



Advances in Optics and Photonics

Non-Hermitian photonic band winding and skin effects: a tutorial

HEMING WANG,  JANET ZHONG, AND SHANHUI FAN* 

Department of Electrical Engineering and Edward L. Ginzton Laboratory, Stanford University, Stanford, California 94305, USA

*shanhui@stanford.edu

Received May 7, 2024; revised August 12, 2024; accepted August 20, 2024;
published 28 September 2024

Non-Hermitian band structures have gained considerable attention due to the novel phenomena not present in their Hermitian counterparts and their connection to various branches of mathematics such as topology and complex analysis. The study of such band structures may also find applications in laser design and in sensing. The spectra and eigenmode characteristics of extended non-Hermitian systems depend strongly on the boundary conditions. With periodic boundary conditions, the spectra can become complex, leading to band winding on the complex frequency plane. With open boundary conditions, the eigenmodes have spatial profiles that are localized at the boundary, an effect known as the non-Hermitian skin effect. Here we provide an overview of the band winding and skin effects in non-Hermitian photonics bands, focusing on one-dimensional cases and photonic applications. We aim to provide a detailed, consistent, and unifying treatment of various phenomena associated with non-Hermitian band structures. © 2024 Optica Publishing Group. All rights, including for text and data mining (TDM), Artificial Intelligence (AI) training, and similar technologies, are reserved.

<https://doi.org/10.1364/AOP.529289>

| | |
|---|-----|
| 1. Introduction | 661 |
| 2. Notation and Concepts | 662 |
| 2.1. Dynamics and Band Structures | 662 |
| 2.2. Boundary Conditions | 664 |
| 2.3. Overview of Single-Band One-Dimensional Models | 665 |
| 3. Some Specific Examples | 666 |
| 3.1. Hatano–Nelson Model | 666 |
| 3.1a. Hermitian Case | 666 |
| 3.1b. Non-Hermitian Case | 669 |
| 3.1c. Gauge Transformations | 672 |
| 3.1d. General Cases | 674 |
| 3.2. Model with Next-Nearest-Neighbor Coupling | 675 |
| 4. Semi-Infinite Boundary Conditions and the Winding Number | 679 |
| 4.1. Iso- $ z $ Contours and Gauge Transformation | 680 |

| | | |
|-------|---|-----|
| 4.2. | Winding Number and the Point-Gap Topology | 681 |
| 4.3. | Non-Hermitian Bulk–Boundary Correspondence for Skin Modes . . | 686 |
| 4.4. | Degenerate Cases | 687 |
| 5. | Open Boundary Conditions and the Generalized Brillouin Zone | 688 |
| 5.1. | Condition for Mode Existence | 689 |
| 5.1a. | Mathematical Argument | 689 |
| 5.1b. | Physical Argument | 690 |
| 5.1c. | Degeneracy Issues | 691 |
| 5.2. | Spectrum Properties and the GBZ | 691 |
| 5.3. | Non-Hermitian Skin Effect | 696 |
| 5.3a. | Hermiticity | 697 |
| 5.3b. | Reciprocity | 698 |
| 5.3c. | Time-Reversal Symmetry | 698 |
| 5.4. | Spectral Dependence on Boundary Conditions | 698 |
| 6. | Multiband Models | 702 |
| 6.1. | Overview of Multiband One-Dimensional Models | 704 |
| 6.2. | Example: the SSH Model | 704 |
| 6.2a. | Hermitian SSH Model | 704 |
| 6.2b. | Non-Hermitian SSH Model | 707 |
| 6.3. | Winding Number, Braiding, and Edge Modes | 708 |
| 6.4. | Semi-Infinite Boundary Conditions | 712 |
| 6.5. | Open Boundary Conditions | 715 |
| 6.5a. | Properties of the Spectra | 716 |
| 6.5b. | Generalized Brillouin Zone | 717 |
| 6.5c. | Exceptions to the General Condition | 717 |
| 6.6. | Open-Boundary Spectra Under Symmetries | 718 |
| 6.6a. | Hermiticity | 718 |
| 6.6b. | Reciprocity | 718 |
| 6.6c. | Sublattice Symmetry | 719 |
| 7. | Calculating the Open-Boundary Spectra | 719 |
| 7.1. | Analytical Approach | 720 |
| 7.2. | Semi-Analytical Approach | 721 |
| 7.3. | Numerical Direct Approach | 722 |
| 7.4. | Numerical Approach Based on Gauge Transformations | 722 |
| 8. | Experimental Implementations and Potential Applications | 723 |
| 8.1. | Experiments | 723 |
| 8.2. | Applications | 723 |
| 9. | Summary and Outlook | 724 |
| | Appendix A. Riemann Surfaces | 726 |
| | Appendix B. Toeplitz Matrices | 729 |
| | Appendix C. Number of Independent Boundary Conditions for Multiband Models | 731 |
| | Funding | 734 |
| | Acknowledgments | 734 |
| | Disclosures | 734 |
| | Data Availability | 734 |
| | References | 734 |

Non-Hermitian photonic band winding and skin effects: a tutorial

HEMING WANG, JANET ZHONG, AND SHANHUI FAN

1. INTRODUCTION

Topological physics [1–3] applies topology, a branch of geometry that focuses on conserved quantities under continuous deformations, to various physical phenomena. A major breakthrough in topological physics is the discovery of topological insulators in condensed matter physics, where the bulk of a solid can be insulating but the topology of electronic band structures can create robust conducting states at the interface. The concept of band topology has since been carried over to photonic bands and studied extensively in photonics and acoustics [4–6].

In both condensed matter physics and photonics, the initial works on band topology have focused on Hermitian Hamiltonians. On the other hand, in recent years there are also emerging interests in the study of band topology for non-Hermitian systems [7–26]. In photonics, gain or loss are rather common in practical systems, and the effects of gain or loss are described by effective non-Hermitian Hamiltonians. The study of non-Hermitian band topology is therefore quite natural in the photonics context.

Band theory for non-Hermitian systems possesses many unique aspects that are not shared by its Hermitian counterparts. In Hermitian systems, the nontrivial band topology arises entirely from the behaviors of the eigenvectors of the Hamiltonian. In contrast, in non-Hermitian systems, nontrivial topology can arise in the behaviors of both the eigenvectors [15,18–21] and the eigenvalues. Two prominent effects of the eigenvalue topology of non-Hermitian band theory are the band winding and the non-Hermitian skin effect. The eigenvalues (optical frequencies) of non-Hermitian bands can take complex values and trace out curves on the complex frequency plane when the wave vector changes. As they are no longer restricted to the real axis, the bands can wind around certain complex frequency points and are characterized by a topological invariant known as the winding number. A nonzero winding number, in turn, is related to the non-Hermitian skin effect, where most of the eigenmodes of an open chain become localized near the boundary [17,27]. These effects have been demonstrated experimentally and have potential applications in novel state transport and improved sensitivity for sensors.

This Tutorial aims to give a pedagogical discussion on non-Hermitian band winding and skin effect in photonic systems. We focus on one-dimensional tight-binding models as the methods for such models have been relatively well-established. Emphasis is placed on both physical intuitions and mathematical rigor. We avoid jargon as much as possible to make the tutorial accessible to readers without backgrounds in non-Hermitian physics or topological models.

There have been several reviews that focus on the non-Hermitian skin effect [28,29] that also summarize the experimental implementation and applications. As a tutorial that focuses on fundamental theory and mathematics, we only provide a brief discussion of the experimental results. The field of general non-Hermitian topology is much richer, and there are prominent effects from band braiding, exceptional points, as well as the interplay with eigenmode topology such as edge mode behavior. We only touch upon these topics when necessary, and we refer interested readers to the following reviews:

[30–34] on non-Hermitian topological photonics, [35] on general non-Hermitian photonics, [36] on exceptional-point geometries, [37–39] on non-Hermitian topological band theory, and [40] on non-Hermitian physics in general.

The outline of this tutorial is as follows. In Section 2 we introduce the basic concepts related to non-Hermitian band structures, including the periodic, semi-infinite, and open boundary conditions for a one-dimensional tight-binding chain. We also set up notation that we use consistently throughout the tutorial. Sections 3–5 focus on single-band models. In Section 3 we calculate the complete spectra of two examples of non-Hermitian models to show the connection between the spectra of different boundary conditions. We also introduce gauge transformations as an important tool in understanding the spectra. In Section 4 we study the spectra of semi-infinite boundary conditions in general. The concept of winding number is introduced by applying gauge transformations to sweep the shifted Brillouin zone (BZ). This leads to a bulk–boundary correspondence for the number of modes at a given frequency for a semi-infinite chain. In Section 5 we study the spectra of open boundary conditions in general. We derive the condition for skin mode existence, known as the generalized Brillouin zone (GBZ), and use it to characterize the non-Hermitian skin effect. Section 6 focuses on multiband models, where we calculate the complete spectra of the Hermitian and non-Hermitian Su–Schrieffer–Heeger (SSH) models as examples and briefly discuss the relations of band winding to other topological phenomena in non-Hermitian models such as band braiding. In Section 7 we discuss and compare some procedures of calculating the open-boundary spectra. In Section 8 we briefly review the experimental implementations and potential applications of the band winding and non-Hermitian skin effect. Finally, in Section 9 we conclude the tutorial by summarizing ongoing research directions. Various mathematical results related to the band winding and non-Hermitian skin effect are collected in the appendices.

2. NOTATION AND CONCEPTS

Throughout this tutorial, we focus on one-dimensional models (Fig. 1), where each unit cell is labeled by an integer n indicating its position. For each cell, a *wave function* ψ_n can be defined, representing the field amplitudes on the cells. This wave function may be the electric field amplitude in photonic crystals or the actual electron wave function in lattice models. In general, there will be *couplings* between the cells that induce transitions of the wave function from one cell to another, forming a chain structure. We assume that the couplings possess *translational invariance*, i.e., they only depend on the position difference of the “from” cell and the “to” cell, not on their absolute positions. We also assume that the model is *tight-binding*, i.e., there are no couplings of cells if their distance is beyond a certain range.

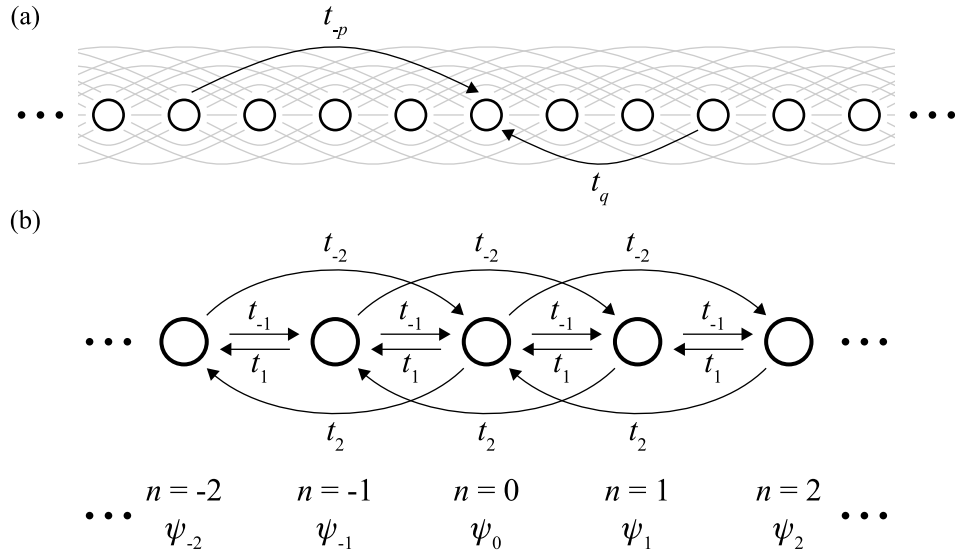
Depending on the nature of the model, ψ_n at any location n may be a scalar (a single amplitude) or a vector (a collection of amplitudes). In the scalar case, the coupling coefficients are also scalars, and the models feature a single band in the wave vector space. One such example is the Hatano–Nelson model [41], which is studied in detail in the following. In the vector case, the coupling coefficients will be matrices with matching dimensions and the model features multiple bands. Examples include the SSH model [42] and its non-Hermitian variations [16,21,27]. We mainly work with the single-band case until Section 5, and briefly discuss the multiband case in Section 6.

2.1. Dynamics and Band Structures

In a single-band model, the dynamics of ψ in the spatial domain can be described as

$$\frac{d\psi_n}{d\tau} = \cdots - it_{-2}\psi_{n-2} - it_{-1}\psi_{n-1} - it_0\psi_n - it_1\psi_{n+1} - it_2\psi_{n+2} + \cdots, \quad (1)$$

Figure 1



Generic one-dimensional model. (a) A chain of cells with translational-invariant tight-binding couplings between them. Here the furthest coupling received by any unit cell comes from four unit cells to the left ($p = 4$) and three unit cells to the right ($q = 3$). (b) A detailed view of the chain with position and wave function labels. Long-range couplings beyond next-nearest neighbors have been omitted for clarity.

where $i^2 = -1$, ψ_n is the wave function on cell n , τ is the time variable, and t_m denotes the coupling coefficient from the $(n + m)$ th cell to the n th cell (t_0 should be interpreted as an on-site potential). For a Hermitian model, we have $t_m = t_{-m}^*$, but t_m can be arbitrary complex numbers in general models. The (effective) Hamiltonian of this system would be

$$H = \sum_{n,m} t_m \psi_n^\dagger \psi_{n+m} \quad (2)$$

and the dynamics can be recovered from H by formally applying the Heisenberg equation $d\psi_n/d\tau = i[H, \psi_n]$.

Alternatively, the dynamics can be put into a matrix form:

$$\frac{d}{d\tau} \begin{bmatrix} \vdots \\ \psi_0 \\ \psi_1 \\ \psi_2 \\ \psi_3 \\ \vdots \end{bmatrix} = -i \begin{bmatrix} \ddots & \vdots & \vdots & \vdots & \vdots & \vdots \\ \cdots & t_0 & t_1 & t_2 & t_3 & \cdots \\ \cdots & t_{-1} & t_0 & t_1 & t_2 & \cdots \\ \cdots & t_{-2} & t_{-1} & t_0 & t_1 & \cdots \\ \cdots & t_{-3} & t_{-2} & t_{-1} & t_0 & \cdots \\ & \vdots & \vdots & \vdots & \vdots & \ddots \end{bmatrix} \begin{bmatrix} \vdots \\ \psi_0 \\ \psi_1 \\ \psi_2 \\ \psi_3 \\ \vdots \end{bmatrix}. \quad (3)$$

This matrix has constant entries for each descending diagonal, known as an *infinite Toeplitz matrix* [43].

The tight-binding assumption indicates that there are only finite terms in the summation of Eq. (1), starting from the t_{-p} term and ending at the t_q term [Fig. 1(a)]:

$$\frac{d\psi_n}{d\tau} = -i \sum_{-p \leq m \leq q} t_m \psi_{n+m}. \quad (4)$$

In general, we assume that there are both couplings from the left and the right ($p \geq 1$ and $q \geq 1$), and p and q represent the actual furthest coupling ranges in the system ($t_{-p} \neq 0$ and $t_q \neq 0$), unless stated otherwise for some special cases.

We are interested in the *modes* (eigenmodes) of the system, where the time evolution of ψ is in the form of $\exp(-i\omega\tau)$ and ω is the angular frequency. In the case where ω is real, this would correspond to monochromatic light in a photonic system. As the system possesses translational invariance in the absence of boundary conditions, each mode is a state with a fixed wave vector and can therefore be written as

$$\psi_n(\tau) = \psi_0(\tau = 0) \times \exp(ikn) \times \exp(-i\omega\tau), \quad (5)$$

where k is the wave vector. Given the coupling coefficients t_n , ω can be solved from Eq. (1) as

$$\omega = \cdots + t_{-2}e^{-2ik} + t_{-1}e^{-ik} + t_0 + t_1e^{ik} + t_2e^{2ik} + \cdots \quad (6)$$

or, within the tight-binding assumption,

$$\omega = \sum_{-p \leq m \leq q} t_m e^{mik}. \quad (7)$$

We introduce the *phase factor* per unit cell as

$$z \equiv e^{ik}. \quad (8)$$

With this notation, ω has the form of a Laurent series in z :

$$\omega = \sum_{-p \leq m \leq q} t_m z^m. \quad (9)$$

We refer to the above equation as the *band structure* of the model. Specifying a single-band model with the coupling coefficients is equivalent to specifying its band structure as a Laurent polynomial.

It will often be convenient to treat k , z , and ω as complex variables. To this end, we use subscripts r and i to denote the real and imaginary part of a complex number, i.e., $\omega = \omega_r + i\omega_i$. In addition, we will scale the physical frequency and coupling constants by a frequency factor such that all quantities in Eq. (9) are dimensionless (z is already dimensionless by definition; k is dimensionless as the positions are dimensionless integers, and can be converted into physical wave vectors by dividing the unit cell length).

2.2. Boundary Conditions

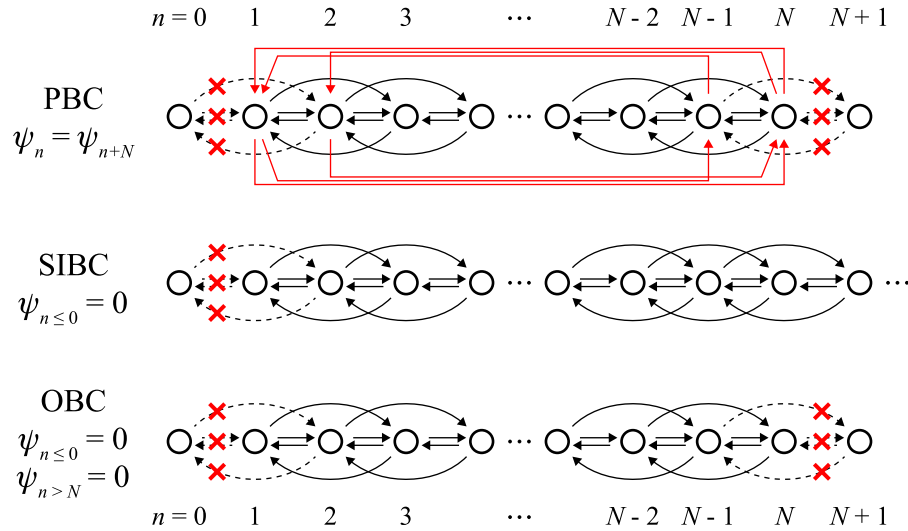
In most physical systems, it is not possible to implement the one-dimensional chain that extends to infinity in both directions, and some boundary conditions will be added to the system. The three boundary conditions most commonly encountered are illustrated in Fig. 2.

The *periodic boundary condition* (PBC) takes a section of the chain of length N and wraps it around into a circle, effectively setting

$$\psi_n = \psi_{n+N}. \quad (10)$$

Due to the periodic constraint, the wave vector k can only take real values ($k_i = 0$, or $|z| = 1$), consistent with the conventional BZ notion.

Figure 2



Three different boundary conditions: periodic, semi-infinite, and open.

The *semi-infinite boundary condition* (SIBC) takes a semi-infinite chain by removing the chain to the left of $n = 1$. This is equivalent to setting

$$\psi_n = 0, \quad n \leq 0 \quad (11)$$

As the chain only extends to the right, the modes may decay to the right, corresponding to k values in the upper complex k plane ($k_i \geq 0$, or $|z| \leq 1$). If studying the semi-infinite chain that extends to the left ($\psi_n = 0$ when $n \geq 0$), then $k_i \leq 0$ or $|z| \geq 1$.

The *open boundary condition* (OBC) takes a section of the chain of length N by removing the chain outside the section. Unlike the case with PBC, in OBC there is no coupling between the two ends of the finite-length chain. The OBC is equivalent to setting

$$\psi_n = 0, \quad n \leq 0 \text{ or } n > N. \quad (12)$$

In the cases of SIBC and OBC, the modes of the system may have $k_i \neq 0$. For non-Hermitian systems, there are in general two types of modes with $k_i \neq 0$. One type is *edge modes*, which are spectrally isolated and not limited to non-Hermitian systems. In fact, these can be deformed continuously into edge modes in Hermitian systems. The other type is the *skin modes*, with continuous frequencies in the spectral domain, and can be deformed continuously into bulk modes for Hermitian models. The skin modes are exclusive to non-Hermitian models and their appearance has been termed the *non-Hermitian skin effect* [27], similar to the skin effect for conductors in electromagnetic wave propagation that also features $k_i \neq 0$. The origin and properties of these modes are the central topic of this tutorial.

2.3. Overview of Single-Band One-Dimensional Models

With the concepts introduced previously, we provide an overview of the spectral characteristics of single-band models in Table 1. A prominent spectral feature of the non-Hermitian models is that the mode frequencies are allowed to be complex, which leads to band winding. Band winding is not possible in Hermitian models because the boundary conditions listed in the table are all Hermitian and a Hermitian operator can only have real eigenvalues. In addition, the SIBC spectra of non-Hermitian models generally consist of regions that occupy a finite area on the complex ω plane, while all other spectra are generally line or curve segments. For the mode profiles, the SIBC and

Table 1. Spectral and Modal Features of Hermitian and Non-Hermitian Single-Band One-Dimensional Models^a

| | Hermitian Models | Non-Hermitian Models | Related Concepts |
|--------------|---|---|--|
| PBC spectra | $\omega \in \mathbb{R}$, line segments | $\omega \in \mathbb{C}$, loops | Band structure [Eq. (9)] |
| PBC modes | $k \in \mathbb{R}$, $ z = 1$ | $k \in \mathbb{R}$, $ z = 1$ | — |
| SIBC spectra | $\omega \in \mathbb{R}$, line segments | $\omega \in \mathbb{C}$, regions | Winding number (Section 4.2), Bulk–boundary correspondence (Section 4.3) |
| SIBC modes | $k \in \mathbb{R}$, $ z = 1$ | $k_i \geq 0$, $ z \leq 1$ (right-extending chains) | Gauge transformations (Sections 3.1c and 4.1) |
| OBC spectra | $\omega \in \mathbb{R}$, line segments | $\omega \in \mathbb{C}$, curve segments | GBZ (Sections 5.1 and 5.2) |
| OBC modes | $k \in \mathbb{R}$, $ z = 1$ | No restrictions | Non-Hermitian skin effect (Section 5.3) |

^aHere \mathbb{R} (\mathbb{C}) is the domain of real (complex) numbers. Related concepts have also been listed.

OBC allow the mode to have complex wave vectors which leads to the non-Hermitian skin effects, but these decaying or growing modes cannot be eigenmodes under the Hermiticity constraints. As such, non-Hermitian skin effects can only be found in non-Hermitian models. Specific examples are demonstrated in Section 3, whereas a general discussion on the SIBC and OBC spectra can be found in Sections 4 and 5, respectively.

3. SOME SPECIFIC EXAMPLES

Before discussing band winding and the non-Hermitian skin effect in their most general forms, we look at two specific examples of one-dimensional tight-binding structures: the Hatano–Nelson model and a model with single-sided next-nearest-neighbor coupling. In both examples, the PBC, SIBC, and OBC spectra are calculated directly, and the results are used to demonstrate some general features of non-Hermitian band structures. We also introduce the concept of gauge transformations in the context of one-dimensional models, which transform the Hamiltonian by relabeling the wave functions and are important for understanding the behavior of the OBC spectrum.

3.1. Hatano–Nelson Model

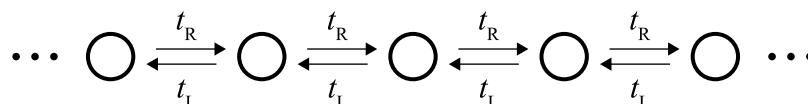
Perhaps the simplest one-dimensional single-band model is the *Hatano–Nelson* model [41] (Fig. 3). The model features no on-site potential and only nearest-neighbor couplings, where the coupling coefficient to the left is $t_L = t_L$ and the coupling coefficient to the right is $t_R = t_R$. Its band structure [Eq. (9)] is given by

$$\omega = t_R z^{-1} + t_L z. \quad (13)$$

3.1a. Hermitian Case

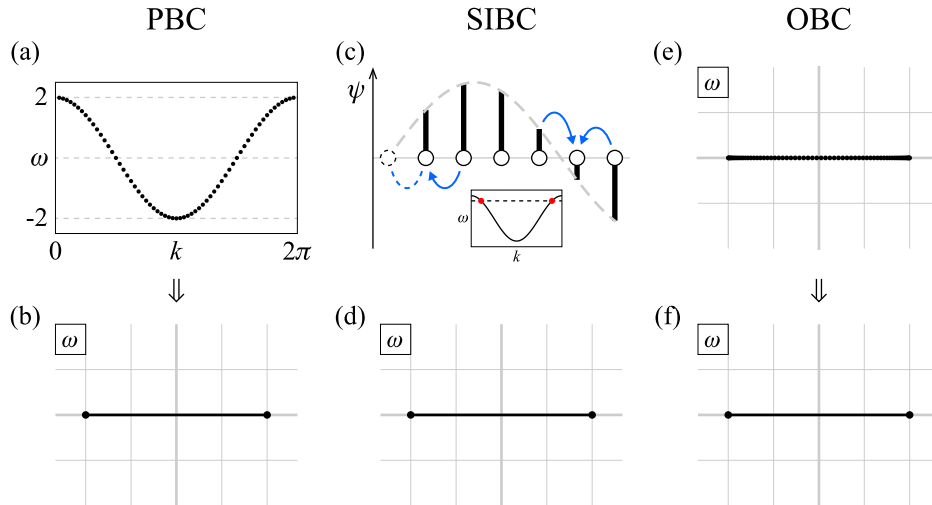
We begin by considering a Hermitian case of the model where $t_L = t_R \equiv t$ and $t > 0$. This reduces the model to the single-band nearest-neighbor-coupling model encountered in solid-state physics. Although the results are well-known, we pedagogically derive them here without using the intuitions related to Hermiticity to compare with the non-Hermitian cases in the following. The band structure for this particular case can

Figure 3



Schematic of the Hatano–Nelson model.

Figure 4



Spectra of a Hermitian case of the Hatano–Nelson model, with $t_L = t_R = 1$. (a) The PBC spectrum for $N = 64$ plotted as real ω versus real k , resembling band diagrams found in solid-state physics. (b) The PBC spectrum for $N \rightarrow \infty$ is plotted in the complex ω plane. The thick gray lines indicate the real and imaginary axes of the ω plane, and the length of each grid corresponds to one unit of ω . (c) A possible SIBC mode profile (black bars) formed by the superposition of PBC modes. A lattice site in the bulk region receives coupling from both sides as indicated by blue arrows [Eq. (16)], whereas the lattice site at the boundary only receives coupling from the right [Eq. (17)]. Inset: The PBC modes used for superposition (represented by red dots) have the same frequency. (d) The SIBC spectrum is plotted in the complex ω plane. (e) The OBC spectrum for $N = 64$ is plotted in the complex ω plane. (f) The OBC spectrum for $N \rightarrow \infty$ is plotted in the complex ω plane.

be reduced to

$$\omega = t(z + z^{-1}) = 2t \cos k, \quad (14)$$

which gives the relation between ω and k on an infinite chain.

For the PBC spectrum, it is still possible to write the field distribution as $\exp(ikn)$, except that we must have

$$\exp(ikN) = 1 \quad (15)$$

to satisfy the periodic constraint Eq. (10). This indicates that k can only take discrete values $0, 2\pi/N, 4\pi/N, \dots$ up to $(N-1)2\pi/N$, but the relation between ω and k stays the same. We conclude that the PBC spectrum is simply the band structure evaluated on equidistant points on the real k axis between 0 and 2π . By taking the $N \rightarrow \infty$ limit, the ω values become dense, approaching the continuous curve determined by $\omega = 2t \cos k$ ($0 \leq k < 2\pi$) [Fig. 4(a)]. This argument also holds for general models, and for this reason, we no longer distinguish between the PBC spectrum and the band structure of a model, unless the finiteness of N plays an important role in the underlying physics. It is also useful to visualize the spectrum on the complex ω plane. This facilitates comparison between Hermitian and non-Hermitian spectra with different boundary conditions, as ω may become complex and k is no longer conserved when boundaries are present. The PBC spectrum in Fig. 4(a) becomes a line segment on the complex ω plane [Fig. 4(b)]. For any frequency point on the line segment, it is possible to find a PBC mode with the corresponding frequency, and for a frequency point not on the line segment there are no such PBC modes.

For the SIBC spectrum, we consider the semi-infinite chain extending to the right, which introduces a boundary condition at the left edge [Fig. 4(c)]. Specifically, while the dynamics in the bulk region at all other lattice sites are given by

$$-i\omega\psi_n = -it(\psi_{n-1} + \psi_{n+1}), \quad n \geq 2, \quad (16)$$

the dynamics of the first cell, located at the boundary of the chain, are different:

$$-i\omega\psi_1 = -it\psi_2. \quad (17)$$

Equation (17) can be obtained by fictitiously extending the lattice segment to include the lattice site 0, and then by setting $\psi_0 = 0$ [compare with Eq. (11)]. This derivation provides an indication that Eq. (17) corresponds to a boundary condition that is perfectly reflecting. In the case for OBC, this derivation can be adopted to derive the boundary condition at the other end of the chain as well.

To solve for Eqs. (16) and (17), we first consider the solution of Eq. (16) in the absence of the boundary condition from Eq. (17). This solution is already obtained in Eq. (14), but k is no longer restricted to be real (i.e., z is no longer restricted to be on the unit circle $|z| = 1$). At a given frequency ω , The two solutions of z of Eq. (14) are given by

$$z_{(1)} = \frac{\omega}{2t} \left(1 - \sqrt{1 - \frac{4t^2}{\omega^2}} \right), \quad z_{(2)} = \frac{\omega}{2t} \left(1 + \sqrt{1 - \frac{4t^2}{\omega^2}} \right). \quad (18)$$

The wave vectors $k_{(1)}$ and $k_{(2)}$ can be found by taking logarithms. The introduction of the boundary condition of Eq. (17) breaks the translation symmetry. As a result, the mode of the system is no longer of the form of $\exp(ikn)$, or z^n . Instead, the mode in general has the form of a linear combination of two exponential components:

$$\psi_n = \alpha_{(1)} z_{(1)}^n + \alpha_{(2)} z_{(2)}^n. \quad (19)$$

This form arises since the mode in general needs to satisfy Eq. (16) away from the boundary. In the following, we refer to the argument used here leading to Eq. (19) as the *superposition argument*. To determine the relations between the coefficients $\alpha_{(1)}$ and $\alpha_{(2)}$, we impose the boundary condition $\psi_0 = 0$:

$$\alpha_{(1)} z_{(1)}^0 + \alpha_{(2)} z_{(2)}^0 = 0, \quad \alpha_{(1)} = -\alpha_{(2)} \quad (20)$$

and the constructed mode can be simply written as

$$\psi_n = \alpha_{(1)} (z_{(1)}^n - z_{(2)}^n). \quad (21)$$

The remaining problem is whether the ψ_n from Eq. (21) represents a physically meaningful mode. As the chain extends infinitely to the right, it would be a reasonable requirement that the wave function does not diverge exponentially (i.e., as $n \rightarrow \infty$, $|\psi_n|e^{-cn} \rightarrow 0$ for all $c > 0$). In the following, we refer to this requirement as the *exponential decay requirement*. For the mode profile given by Eq. (21), this would require $|z_{(1)}| \leq 1$ and $|z_{(2)}| \leq 1$ (equivalently, $\text{Im } k_{(1)} \geq 0$ and $\text{Im } k_{(2)} \geq 0$). Instead of going back to the explicit expressions for $z_{(1)}$ and $z_{(2)}$, we can apply Vieta's formula to Eq. (14) as a quadratic equation in z , which states that the product of all roots is given by the ratio of the constant term and the leading coefficient:

$$z_{(1)} z_{(2)} = 1 \rightarrow |z_{(1)}| |z_{(2)}| = 1. \quad (22)$$

Therefore, the only possibility for physical modes is that $|z_{(1)}| = |z_{(2)}| = 1$, which directly corresponds to the PBC modes where k takes real values. The pair of states

satisfy $z_{(1)} = z_{(2)}^*$ ($k_{(1)} = 2\pi - k_{(2)}$ if we restrict both $k_{(1)}$ and $k_{(2)}$ to be within $[0, 2\pi]$), agreeing with the intuition that two states with opposite wave vectors are being superimposed as if one is reflected from the boundary into the other [Fig. 4(c)]. We conclude that the SIBC spectrum is $-2t \leq \omega \leq 2t$ [Fig. 4(d)], identical to the PBC spectrum.

We note that the two end points $\omega = \pm 2t$ have been included in the spectrum, but the corresponding degeneracy cases $z_{(1)} = z_{(2)} = 1$ and $z_{(1)} = z_{(2)} = -1$ do not support a mode in the form of Eq. (21). For now, we simply state that another mode not in the form of Eq. (21) can be found at the exact frequencies $\omega = \pm 2t$, and postpone a full discussion to Section 4.4.

For the OBC spectrum, we again assume the modes are of the form of Eq. (19) but impose boundary conditions for both edges. From the previous discussion, to satisfy the left boundary condition, the mode profile must be of the form

$$\psi_n = \alpha_{(1)}(z_{(1)}^n - z_{(2)}^n), \quad (23)$$

but unlike the SIBC case, here we do not constrain the magnitude of z . Instead, a new boundary condition $\psi_{N+1} = 0$ is applied [Eq. (12)], which leads to

$$z_{(1)}^{N+1} = z_{(2)}^{N+1}. \quad (24)$$

Using $z_{(1)}z_{(2)} = 1$, this leads to $z_{(1)}^{2N+2} = 1$, and we get

$$|z_{(1)}| = |z_{(2)}| = 1. \quad (25)$$

The exact solutions for $z_{(1)}$ is $\exp[i\pi/(N+1)]$, $\exp[2i\pi/(N+1)]$, \dots , $\exp[Ni\pi/(N+1)]$ [equivalently, $k = \pi/(N+1)$, $2\pi/(N+1)$, \dots , $N\pi/(N+1)$]. There are N solutions total, matching the total number of unit cells, and the set of modes is complete. Since the chain is finite in the OBC case, z (and k) can only take discrete values [Fig. 4(e)], but by taking the $N \rightarrow \infty$ limit, the spectrum becomes dense, approaching the continuous interval $-2t \leq \omega \leq 2t$ [Fig. 4(f)].

3.1b. Non-Hermitian Case

With the Hermitian results in mind, we now consider a non-Hermitian case of the model, where t_L and t_R are both positive numbers but $t_L \neq t_R$. For later convenience, we define the geometric mean coupling $t = \sqrt{t_L t_R}$ and the asymmetry factor $g = \ln(t_L/t_R)/2$. The coupling coefficients can then be expressed as

$$t_L = te^g, \quad t_R = te^{-g}. \quad (26)$$

The PBC spectrum, as well as the band structure, is given by

$$\omega = t_R z^{-1} + t_L z = t(e^g z + e^{-g} z^{-1}). \quad (27)$$

The PBC spectrum will contain complex values when $t_L \neq t_R$. To visualize the PBC spectrum on the complex ω plane, we substitute $z = \exp(ik)$ and write

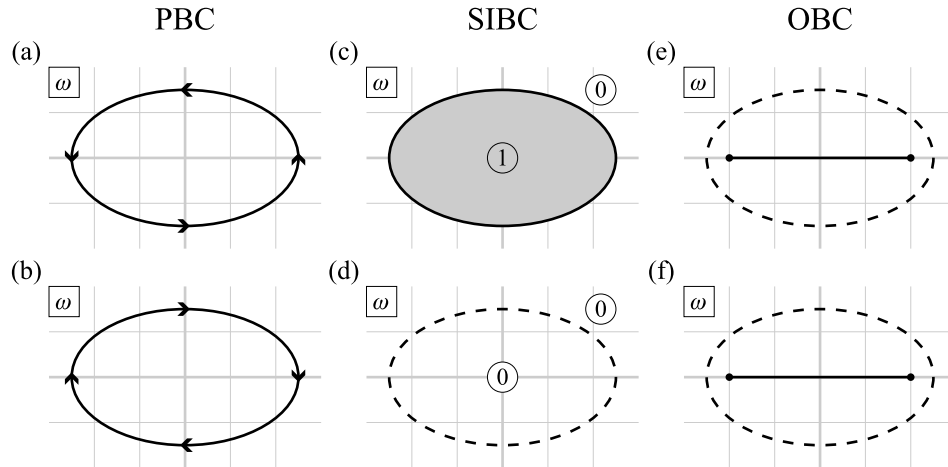
$$\omega = t_R(\cos k - i \sin k) + t_L(\cos k + i \sin k) = (t_L + t_R) \cos k + i(t_L - t_R) \sin k \quad (28)$$

or, in terms of real and imaginary parts,

$$\frac{\omega_r^2}{(t_L + t_R)^2} + \frac{\omega_i^2}{(t_L - t_R)^2} = 1. \quad (29)$$

This is an ellipse in the complex ω plane [Figs. 5(a) and 5(b)]. Its semi-major axis is $t_L + t_R$ on the real axis and its semi-minor axis is $|t_L - t_R|$ on the imaginary axis. The

Figure 5



Spectra of some non-Hermitian cases of the Hatano–Nelson model. (a) The PBC spectra for $t_L = 2$ and $t_R = 1/2$. (b) The PBC spectra for $t_L = 1/2$ and $t_R = 2$. (c) The SIBC spectra for $t_L = 2$ and $t_R = 1/2$. Here the numbers of SIBC modes in the regions are marked with circled numbers. (d) The SIBC spectra for $t_L = 1/2$ and $t_R = 2$. Unlike (c), the PBC spectrum (dashed curve) is not part of the SIBC spectrum. (e) The OBC spectra for $t_L = 2$ and $t_R = 1/2$. The dashed curve indicates the corresponding PBC spectrum. (f) The OBC spectra for $t_L = 1/2$ and $t_R = 2$. The dashed curve indicates the corresponding PBC spectrum. Unlike the previous Hermitian case, distinctions between PBC, SIBC, and OBC spectra can be seen.

foci can be found as

$$\sqrt{(t_L + t_R)^2 - (t_L - t_R)^2} = \sqrt{4t_L t_R} = 2t. \quad (30)$$

When $t_L > t_R$ ($g > 0$), the curve is traversed in the counterclockwise direction when k increases from 0 to 2π , and vice versa. For any frequency point on the curve, there is a PBC mode with the corresponding frequency.

For the SIBC spectrum (where the chain extends to the right), the argument leading to Eq. (19) and Eq. (21) still applies, hence the mode has the same form of spatial profile:

$$\psi_n = \alpha_{(1)}(z_{(1)}^n - z_{(2)}^n), \quad (31)$$

where the solutions to the band structure are found as

$$z_{(1)} = \frac{\omega}{2t_L} \left(1 - \sqrt{1 - \frac{4t^2}{\omega^2}} \right), \quad z_{(2)} = \frac{\omega}{2t_L} \left(1 + \sqrt{1 - \frac{4t^2}{\omega^2}} \right). \quad (32)$$

This time, Vieta's formula indicates that

$$z_{(1)} z_{(2)} = \frac{t_R}{t_L} = e^{-2g}. \quad (33)$$

If $t_L < t_R$ ($g < 0$), then $|z_{(1)}| |z_{(2)}| > 1$ implies that no modes can be found at all. On the other hand, if $t_L > t_R$ ($g > 0$), then it should be possible to satisfy the $|z| \leq 1$ condition for some region in the complex ω plane. Using the explicit expression Eq. (32), the $|z_{(1)}| \leq 1$ and $|z_{(2)}| \leq 1$ condition can be rearranged as

$$\frac{t_R}{t_L} \left| 1 - \sqrt{1 - \frac{4t^2}{\omega^2}} \right| \leq \left| 1 + \sqrt{1 - \frac{4t^2}{\omega^2}} \right| \leq \frac{t_L}{t_R} \left| 1 - \sqrt{1 - \frac{4t^2}{\omega^2}} \right|, \quad (34)$$

which can then be solved as

$$\frac{\omega_r^2}{(t_L + t_R)^2} + \frac{\omega_i^2}{(t_L - t_R)^2} \leq 1. \quad (35)$$

We thus conclude that the SIBC spectrum is exactly the interior of the ellipse representing the PBC spectrum if $t_L > t_R$, where one mode can be found for each complex frequency ω on or inside the ellipse [Fig. 5(c)]. For $t_L < t_R$, no mode exists at any given complex frequency [Fig. 5(d)].

Unlike the Hermitian case where the SIBC spectrum is a line segment, the non-Hermitian SIBC spectrum contains an entire area of ω . In addition, the boundary of the SIBC spectrum is given by the PBC spectrum, although the structures of these two boundary conditions are very different (Fig. 2). This can be explained from an analytic function viewpoint. The band structure of Eq. (27), which is a complex function from z to ω , maps the $|z| \leq 1$ closed disk into some region on the ω plane (possibly with self-overlaps). The image of the boundary of the disk $|z| = 1$ is precisely the PBC spectrum on the ω plane. The interior of the PBC ellipse on the ω plane is covered twice by the closed disk through the band structure mapping, indicating that both preimages of ω are inside the disk and satisfying the exponential decay requirement for the SIBC mode. At these frequencies, therefore, one can obtain a physical SIBC mode through superposition. In contrast, the exterior of the PBC ellipse is covered only once, indicating only one preimage of ω inside the disk $|z| = 1$. There is no SIBC mode at such ω . We demonstrate more connections between PBC and SIBC spectra in Section 4 using this idea.

It would be instructive at this point to study the SIBC mode profile given by Eq. (21) in the non-Hermitian case in more detail. In contrast to the Hermitian case where the components in the superposition are PBC modes [e.g., Fig. 4(c)], the states in the non-Hermitian case may decay into the bulk and lead to a decaying profile for the SIBC mode. As $|z|$ represents the ratio of wave function amplitudes on neighboring cells, the amplitudes of each component scales exponentially as $|z|^n$, and the component with the largest $|z|$ will dominate at large n . Representative SIBC mode profiles for the Hatano–Nelson model with $t_L > t_R$ are shown in Fig. 6. When the frequency point is on the line segment $-2t \leq \omega \leq 2t$, the z solutions satisfy $|z_{(1)}| = |z_{(2)}| = e^{-g}$. Both components have the same amplitude scaling and leads to the asymptotic behavior $|\psi| \sim e^{-ng}$ of the SIBC mode [Fig. 6(a)]. As the frequency point moves closer to the PBC spectrum, one of the z solution approaches $|z| = 1$ whereas the other approaches $|z| = e^{-2g}$. For convenience, we order the z solutions such that $|z_{(1)}| \leq |z_{(2)}|$. As the $z_{(2)}$ component decays slower than the $z_{(1)}$ component, the SIBC mode will be dominated by the $z_{(2)}$ component at large n , leading to $|\psi| \sim |z_{(2)}|^n$ [Fig. 6(b)].

For the OBC spectrum, we start again from the mode profile

$$\psi_n = \alpha_{(1)}(z_{(1)}^n - z_{(2)}^n) \quad (36)$$

with $z_{(1)}$ and $z_{(2)}$ given by Eq. (32). Since the structure is finite, we do not impose the exponential decay requirement of $|z| \leq 1$. Instead, we impose $\psi_{N+1} = 0$, which leads to

$$z_{(1)}^{N+1} = z_{(2)}^{N+1}. \quad (37)$$

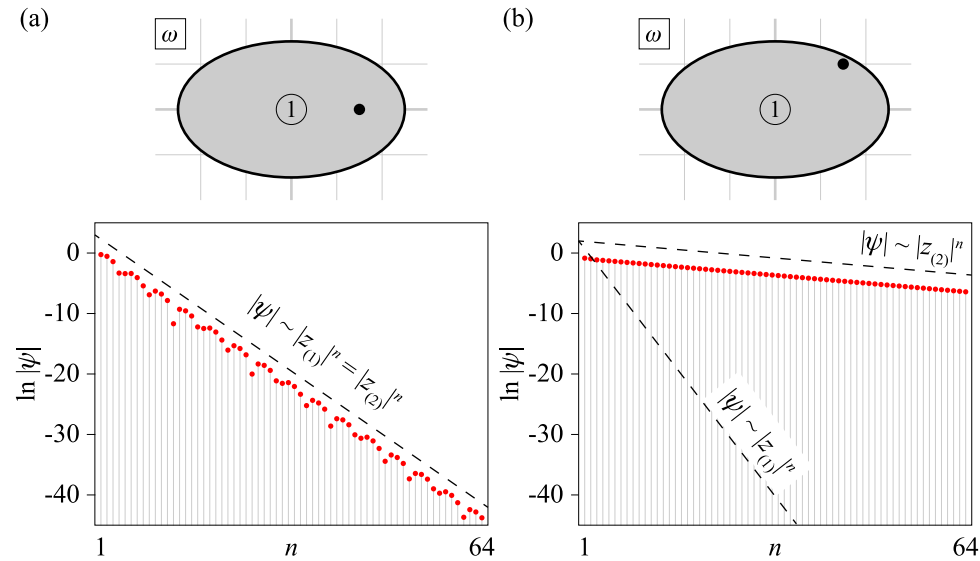
This time $z_{(1)}z_{(2)} = e^{-2g}$, and we get

$$|z_{(1)}| = |z_{(2)}| = e^{-g}. \quad (38)$$

The exact solution for $z_{(1)}$ is $e^{-g}e^{iK}$, where $K = \pi/(N+1), 2\pi/(N+1), \dots, N\pi/(N+1)$. The corresponding ω values are

$$\omega = t(e^g z + e^{-g} z^{-1}) = 2t \cos K. \quad (39)$$

Figure 6



SIBC mode profiles for the non-Hermitian Hatano–Nelson model with $t_L = 2$ and $t_R = 1/2$. (a) Top panel: The SIBC spectrum from Fig. 5(c). The frequency $\omega = 3/2$ has been marked with a black dot. Bottom panel: Normalized SIBC mode profiles at $\omega = 3/2$. The dashed line indicates the scaling of $|\psi|$ with n . (b) Top panel: The SIBC spectrum from Fig. 5(c). The frequency $\omega = 3/2 + i$ has been marked with a black dot. Bottom panel: Normalized SIBC mode profile at $\omega = 3/2 + i$. The two dashed lines indicate the $|z_{(1)}|^n$ and $|z_{(2)}|^n$ scaling. As $|z_{(1)}| \leq |z_{(2)}|$, the SIBC mode is dominated by the $z_{(2)}$ component.

Taking the $N \rightarrow \infty$ limit, we conclude that the OBC spectrum is the line segment connecting the two foci of the PBC ellipse, and does not depend on whether $t_L < t_R$ or $t_L > t_R$ [Figs. 5(e) and 5(f)].

We end this case with a brief discussion of the OBC mode profiles. Substituting the $z_{(1)}$ and $z_{(2)}$ solutions into the mode profile, we obtain

$$\psi_n = 2i\alpha_{(1)}e^{-ng} \sin(nK). \quad (40)$$

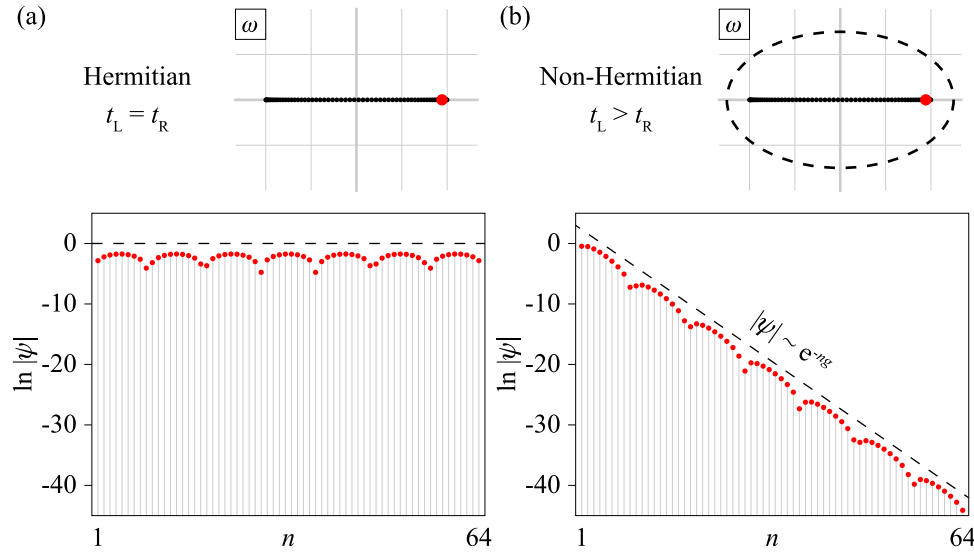
Apart from the oscillation term, the overall mode profile scales as $|\psi_n| \sim e^{-ng}$. If $t_L > t_R$ ($g > 0$), the mode will pile up on the left side of the chain (Fig. 7), agreeing with the intuition that more amplitude is transported to the left than the right. Equation (40) provides the first example of OBC non-Hermitian skin modes, where every mode for the OBC condition is localized on the left edge for $g > 0$ or the right edge for $g < 0$.

In summary, as the couplings become non-Hermitian, the spectra of non-Hermitian models may become complex and the associated modes becomes decaying or growing along the chain (Table 1). The OBC spectra of the model being considered remains real, which is not a general feature of non-Hermitian models but a consequence of *gauge transformations*. This is now discussed in detail.

3.1c. Gauge Transformations

We observe that the OBC spectrum of the non-Hermitian model studied previously [Eq. (39)] is identical to that of a corresponding Hermitian model where both coupling coefficients in the non-Hermitian model are replaced by t . In addition, the corresponding OBC mode profiles differ by only a factor of $\exp(ng)$ at each site. These are not simple coincidences and can be understood by an argument based on gauge transformations.

Figure 7



Comparison of OBC mode profiles for the Hermitian and non-Hermitian Hatano–Nelson models. (a) Top panel: OBC spectrum (dots) for the Hermitian model with $t_L = t_R = 1$ and $N = 64$. The frequency $\omega = 2 \cos(7\pi/65) \approx 1.887$ has been marked with a red dot. Bottom panel: Normalized OBC mode profile at $\omega \approx 1.887$. (b) Top panel: OBC spectrum (dots) and PBC spectrum (dashed curve) for the non-Hermitian model with $t_L = 2$, $t_R = 1/2$ and $N = 64$. The frequency $\omega = 2 \cos(7\pi/65) \approx 1.887$ has been marked with a red dot. Bottom panel: Normalized OBC mode profile at $\omega \approx 1.887$. The dashed line indicates the scaling of $|\psi|$ with n .

Loosely speaking, gauge refers to how the amplitude of wave functions is defined. The ψ_n defined so far has been measured by the same unit, but this is not a requirement for describing the dynamics. An analogy would be comparing the lengths of three objects. Although a convenient method is to determine their lengths in units of meters, the results will not change if the first object is measured using kilometers, the second using meters, and the third using millimeters. Gauge transformation describes the wave functions on each site in different units and changes the Hamiltonian of the system accordingly such that the resulting dynamics remain the same. To maintain the translational invariance of the Hamiltonian, a common choice is to define the new wave function as $\Psi_n = \lambda^n \psi_n$, where λ is a scaling factor.

For the above Hatano–Nelson model, the form of the OBC mode suggests the following gauge transformation:

$$\Psi_n = \psi_n e^{ng}. \quad (41)$$

This can be equivalently described as defining a transformation from the original phase factor z into a new Z :

$$Z = e^g z. \quad (42)$$

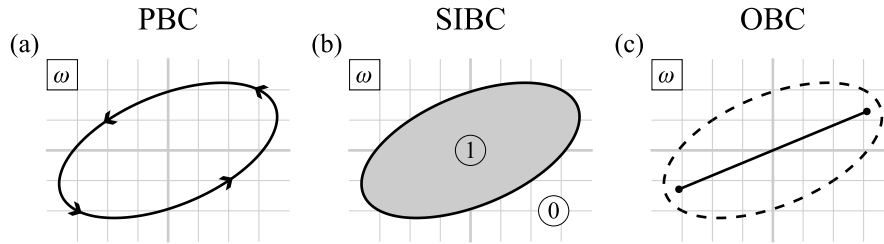
By taking logarithms of the phase factors, the gauge transformation becomes a shift of the wave vector:

$$K = k - ig. \quad (43)$$

As the wave vector shift is along the imaginary axis, this particular gauge transformation is an imaginary gauge transformation. The dynamics in terms of the new wave function Ψ_n can be found by substituting $\psi_n = \Psi_n \exp(-ng)$ into the original dynamics:

$$-i\omega\Psi_n = -i(t_R e^g \Psi_{n-1} + t_L e^{-g} \Psi_{n+1}) = -it(\Psi_{n-1} + \Psi_{n+1}). \quad (44)$$

Figure 8



Spectra of a general case of the Hatano–Nelson model with $t_L = 2 + 2i$ and $t_R = 1$: (a) PBC spectrum; (b) SIBC spectrum; (c) OBC spectrum.

Now, if we interpret this equation as the dynamics of a new system where the actual wave function is Ψ , the new system becomes Hermitian with both nearest-neighbor coupling amplitudes equal to t . Since the form of the OBC boundary conditions for both ψ and Ψ are also equivalent, the OBC spectrum is invariant for such an imaginary gauge transformation. This explains the two models sharing the same OBC spectra and the connection between the OBC mode profiles. We note that the discussion here does not apply to PBC or SIBC spectra as the PBC and the exponential decay requirement are not invariant under an imaginary gauge transformation. Further applications of gauge transformations can be found in Section 4.

3.1d. General Cases

We are now ready to discuss the most general cases, where both t_L and t_R are nonzero *complex* numbers. We again define $t = \sqrt{t_L t_R}$, which is also, in general, a complex number. Correspondingly, we can write $t_L = t e^g e^{-i\phi}$ and $t_R = t e^{-g} e^{i\phi}$, where g and ϕ are real numbers. The band structure is given by

$$\omega = t_R z^{-1} + t_L z = t \left[e^g (e^{-i\phi} z) + e^{-g} (e^{-i\phi} z)^{-1} \right]. \quad (45)$$

This form of the band structure suggests a real gauge transformation, where the wave vector is shifted along the real axis ($K = k - \phi$ and $Z = e^{-i\phi} z$). Although imaginary gauge transformations cannot be applied to PBC and SIBC as $|z|$ will change, real gauge transformations can be performed for PBC, SIBC, and OBC systems while preserving the spectra. For the PBC spectrum, the real gauge transformation effectively relabels each point of the spectrum with a shifted k , and for the SIBC spectrum, the exponential decay requirement is not affected.

As such, after the real gauge transformation, the band structure in terms of the new phase factor $Z = e^{-i\phi} z$ is given by

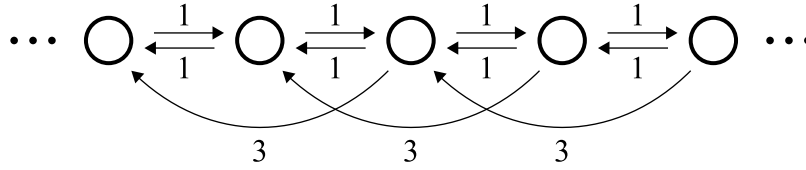
$$\omega = t (e^g Z + e^{-g} Z^{-1}), \quad (46)$$

which resembles the non-Hermitian case described in Section 3.1b but rotated in the complex plane by $\text{Arg}(t)$. All spectral results follow immediately from the previous case.

The PBC spectrum [Fig. 8(a)] is a rotated ellipse, with its semi-major axis $|t_L| + |t_R|$ pointing in the direction given by $\text{Arg}(t)$; the two foci are located at $\pm 2t$. For $|t_L| > |t_R|$, the ellipse is traversed counterclockwise, and vice versa. For $|t_L| = |t_R|$ the ellipse reduces to a line segment connecting $-2t$ and $2t$.

The SIBC spectrum for a right-extending chain [Fig. 8(b)] is either empty ($|t_L| < |t_R|$), the interior of the ellipse ($|t_L| > |t_R|$), or reduced to the line segment connecting $-2t$ and $2t$ ($|t_L| = |t_R|$).

Figure 9



Schematic of a model with next-nearest-neighbor coupling, with the band structure given by $\omega = z^{-1} + z + 3z^2$.

The OBC spectrum [Fig. 8(c)] is always the line segment connecting $-2t$ and $2t$, regardless of the relation between $|t_L|$ and $|t_R|$.

These results for general Hatano–Nelson models (Fig. 8) can be compared with the Hermitian case (Fig. 4), where the spectral features of non-Hermitian models become apparent (see also Table 1): spectra are generally complex, and the SIBC and OBC modes display decaying or growing behavior.

3.2. Model with Next-Nearest-Neighbor Coupling

After the Hatano–Nelson model, we consider a more complicated model by adding a single-sided next-nearest-neighbor coupling term. As analytic calculations with general higher-order models become difficult, we focus on a model with constant coefficients, where the band structure is given by

$$\omega = z^{-1} + z + 3z^2. \quad (47)$$

The schematic of this model is shown in Fig. 9. Similar models with different coupling strengths have been considered in [44].

The PBC spectrum can be straightforwardly drawn on the complex ω plane by substituting $z = e^{ik}$ into the band structure and plotting ω_r and ω_i versus $k \in [0, 2\pi]$. The resulting curve is clover-shaped, traverses counterclockwise, and circles around the origin twice [Fig. 10(a)].

For the SIBC spectrum, we need to separately consider the right-extending and the left-extending chain, as their spectra will be different. We have not focused on the left-extending case for the Hatano–Nelson model, as the spectrum would be equivalent to a right-extending chain with t_L and t_R exchanged (i.e., flipping the entire chain). For the present model, however, both cases need to be considered.

The superposition argument allows us to write the SIBC mode in the form of

$$\psi_n = \alpha_{(1)} z_{(1)}^n + \alpha_{(2)} z_{(2)}^n + \alpha_{(3)} z_{(3)}^n, \quad (48)$$

where $z_{(1)}$, $z_{(2)}$, and $z_{(3)}$ are the three solutions of the band structure with a given ω . To facilitate later discussions related to the exponential decay requirement, we sort the z solutions according to their magnitude in non-decreasing order without loss of generality, requiring that

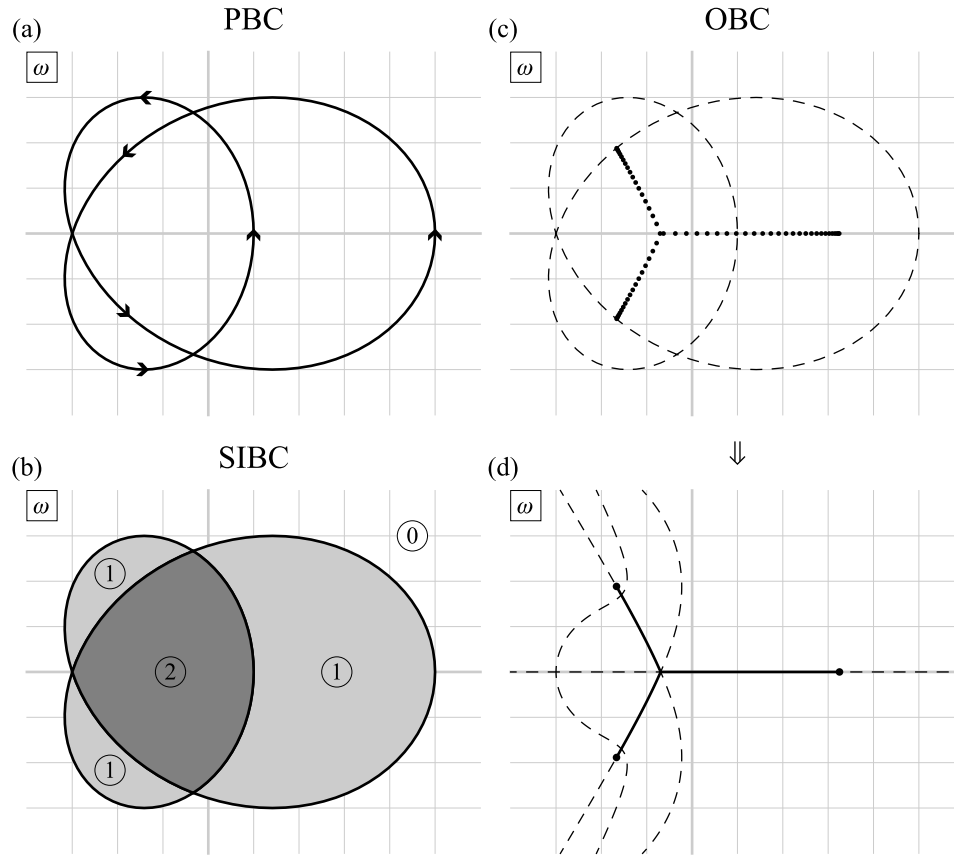
$$|z_{(1)}| \leq |z_{(2)}| \leq |z_{(3)}|. \quad (49)$$

The boundary conditions require some careful consideration as longer-range couplings are now present. We discuss the right-extending chain first and return to the full form of dynamics to find the appropriate boundary conditions:

$$-i\omega\psi_n = -i(\psi_{n-1} + \psi_{n+1} + 3\psi_{n+2}), \quad n \geq 2, \quad (50)$$

$$-i\omega\psi_1 = -i(\psi_0 + \psi_2 + 3\psi_3) = -i(\psi_2 + 3\psi_3). \quad (51)$$

Figure 10



Spectra of the model $\omega = z^{-1} + z + 3z^2$: (a) PBC spectrum; (b) SIBC spectrum; (c) OBC spectrum for $N = 64$ compared with the PBC spectrum (dashed curves); (d) OBC spectrum for $N \rightarrow \infty$, where dashed curves are the analytic curves from Eqs. (57) and (58).

Therefore, the only boundary condition required is $\psi_0 = 0$, as only one coupling from the left is present. This allows us to eliminate one unknown amplitude from the mode:

$$\alpha_{(1)} + \alpha_{(2)} + \alpha_{(3)} = 0 \rightarrow \alpha_{(1)} = -\alpha_{(2)} - \alpha_{(3)}, \quad (52)$$

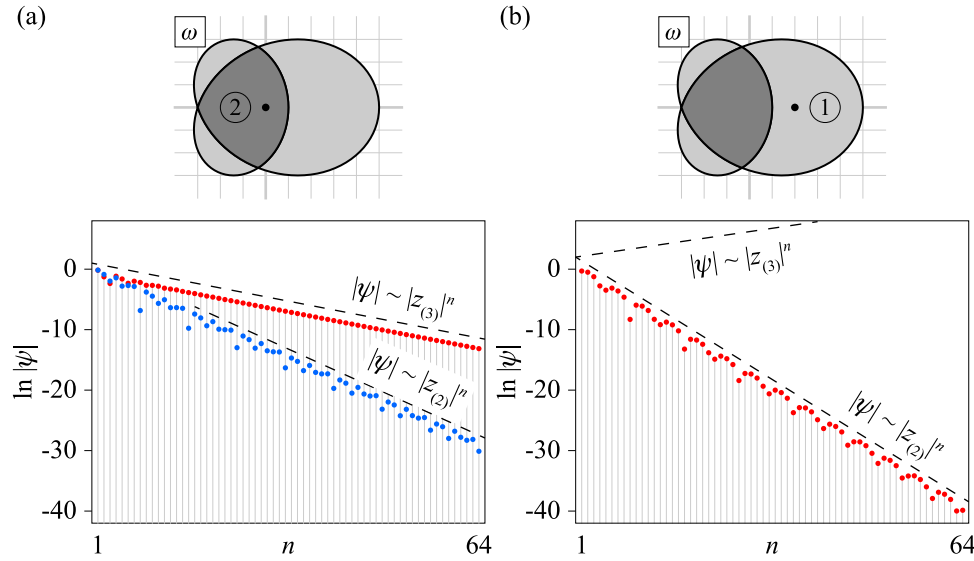
$$\psi_n = (-\alpha_{(2)} - \alpha_{(3)})z_{(1)}^n + \alpha_{(2)}z_{(2)}^n + \alpha_{(3)}z_{(3)}^n. \quad (53)$$

A right-extending chain requires $|z| \leq 1$. At first glance, this would require $|z_{(1)}| \leq 1$, $|z_{(2)}| \leq 1$, and $|z_{(3)}| \leq 1$. However, with certain choices of α , some of the exponential components in Eq. (53) may not appear. Depending on the relative order of $|z_{(1)}|$, $|z_{(2)}|$, $|z_{(3)}|$ and 1, there are three cases to consider.

Case I: $|z_{(1)}| \leq |z_{(2)}| \leq |z_{(3)}| \leq 1$. All components satisfy the exponential decay requirement and may appear in the superposition. As such, $\alpha_{(2)}$ and $\alpha_{(3)}$ can take arbitrary complex values. Analytical calculations are difficult for the roots of a cubic equation, but since the region boundary is given by sections of the PBC curve, we only need to consider each of the five regions separated by the clover shape. Numerical calculation shows that the $|z_{(1)}| \leq |z_{(2)}| \leq |z_{(3)}| \leq 1$ case corresponds to the central region bounded by the inner sections of the PBC curve. The two degrees of freedom from $\alpha_{(2)}$ and $\alpha_{(3)}$ in ψ_n contribute two SIBC modes to the spectrum in these regions in the ω plane.

Case II: $|z_{(1)}| \leq |z_{(2)}| \leq 1 \leq |z_{(3)}|$. Now the $z_{(3)}$ component no longer satisfies the exponential decay requirement and must disappear from the superposition. This requires

Figure 11



SIBC mode profiles for the model $\omega = z^{-1} + z + 3z^2$. (a) Top panel: The SIBC spectrum from Fig. 10(b). The frequency $\omega = 0$ has been marked with a black dot. Bottom panel: Normalized SIBC mode profiles at $\omega = 0$. The dashed line indicates the scaling of $|\psi|$ with n . (b) Top panel: The SIBC spectrum from Fig. 10(b). The frequency $\omega = 2$ has been marked with a black dot. Bottom panel: Normalized SIBC mode profile at $\omega = 2$. The dashed line indicates the scaling of $|\psi|$ with n . Here the $|z_{(3)}|$ scaling does not correspond to a mode as it is exponentially growing from the boundary.

that $\alpha_{(3)} = 0$, and one degree of freedom from $\alpha_{(2)}$ remains in ψ_n . Numerical calculation shows that this case corresponds to the three regions neighboring the central region of the PBC curve. The one degree of freedom in ψ_n contributes one SIBC mode to the spectrum in these regions in the ω plane.

Case III: $|z_{(1)}| \leq 1 \leq |z_{(2)}| \leq |z_{(3)}|$. Both $z_{(2)}$ and $z_{(3)}$ components are not exponentially decaying, requiring $\alpha_{(2)} = \alpha_{(3)} = 0$. Thus, $\psi_n = 0$ identically for all n and there is no SIBC mode. This case corresponds to the unbounded region outside the PBC curve.

It is not possible to have $1 \leq |z_{(1)}| \leq |z_{(2)}| \leq |z_{(3)}|$ as the Vieta's formula applied to the band structure as a polynomial of z results in $z_{(1)}z_{(2)}z_{(3)} = -1/3$.

We conclude that the SIBC spectrum for a right-extending chain is bounded by the outermost sections of the PBC curve. The central region contains two SIBC modes for each ω , where the modes can be chosen such that one mode scales as $|z_{(2)}|^n$ and the other mode scales as $|z_{(3)}|^n$. The three petals each contain one SIBC mode for each ω that scales as $|z_{(2)}|^n$. The entire spectrum is shown in Fig. 10(b), and some SIBC mode profiles can be found in Fig. 11.

For the left-extending chain, we again start from the boundary conditions by looking at the full dynamics near the edge:

$$-i\omega\psi_n = -i(\psi_{n-1} + \psi_{n+1} + 3\psi_{n+2}), \quad n \leq -3, \quad (54)$$

$$-i\omega\psi_{-2} = -i(\psi_{-3} + \psi_{-1} + 3\psi_0) = -i(\psi_{-3} + \psi_{-1}), \quad (55)$$

$$-i\omega\psi_{-1} = -i(\psi_{-2} + \psi_0 + 3\psi_1) = -i(\psi_{-2}). \quad (56)$$

The two couplings from the right requires two boundary conditions: $\psi_0 = 0$ and $\psi_1 = 0$. We do not solve explicitly for the amplitudes and simply observe that ψ_n only

has one degree of freedom for the amplitude and will contain all $z_{(1)}^n$, $z_{(2)}^n$ and $z_{(3)}^n$ components. The left-extending chain, therefore, requires all three z satisfying $|z| \geq 1$, which is impossible since $z_{(1)}z_{(2)}z_{(3)} = -1/3$. We conclude that the SIBC spectrum for a left-extending chain is empty.

For the OBC spectrum, we first present the numerically calculated OBC spectrum for $N = 64$ in Fig. 10(c). The points form a rotated Y shape on the complex ω plane. It is expected that the OBC spectrum for $N \rightarrow \infty$ also has the same Y shape made up of three arcs. Analytical calculation verifies this observation [Fig. 10(d)], where the right portion of the spectrum is a segment of the real ω axis:

$$\omega_i = 0, \quad -\frac{1}{\sqrt[3]{3}} \leq \omega_r \leq \frac{13}{4}, \quad (57)$$

and the two left portions are part of an eighth-order equation that lies within $-5/3 \leq \omega_r \leq -1/\sqrt[3]{3}$ and $|\omega_i| \leq 4\sqrt{2}/3$:

$$\begin{aligned} & 27\omega_i^8 \\ & - 9(12\omega_r^2 - 38\omega_r + 9)\omega_r^6 \\ & - 9(6\omega_r^4 + 174\omega_r^3 - 237\omega_r^2 - 226\omega_r - 60)\omega_i^4 \\ & + 3(108\omega_r^6 + 342\omega_r^5 - 2241\omega_r^4 - 1956\omega_r^3 + 112\omega_r^2 + 1566\omega_r + 325)\omega_i^2 \\ & + (3\omega_r^3 + 1)^2(\omega_r + 3)(27\omega_r + 245) \\ & = 0. \end{aligned} \quad (58)$$

In the following, we outline how these results can be obtained. Starting from the mode profile given by $\psi_n = \alpha_{(1)}z_{(1)}^n + \alpha_{(2)}z_{(2)}^n + \alpha_{(3)}z_{(3)}^n$, we impose three boundary conditions, $\psi_0 = 0$ on the left boundary, and $\psi_{N+1} = 0$ and $\psi_{N+2} = 0$ on the right boundary:

$$\alpha_{(1)} + \alpha_{(2)} + \alpha_{(3)} = 0, \quad (59)$$

$$\alpha_{(1)}z_{(1)}^{N+1} + \alpha_{(2)}z_{(2)}^{N+1} + \alpha_{(3)}z_{(3)}^{N+1} = 0, \quad (60)$$

$$\alpha_{(1)}z_{(1)}^{N+2} + \alpha_{(2)}z_{(2)}^{N+2} + \alpha_{(3)}z_{(3)}^{N+2} = 0. \quad (61)$$

This can be viewed as a set of linear equations on the α and the condition that we get nonzero solutions is the vanishing of its determinant:

$$\begin{vmatrix} 1 & 1 & 1 \\ z_{(1)}^{N+1} & z_{(2)}^{N+1} & z_{(3)}^{N+1} \\ z_{(1)}^{N+2} & z_{(2)}^{N+2} & z_{(3)}^{N+2} \end{vmatrix} = 0. \quad (62)$$

For any finite N , this can be converted into an equation in ω of order N , and the N solutions represent the complex frequencies for the OBC spectrum. To get the spectrum in the $N \rightarrow \infty$ case, we again order the z by $|z_{(1)}| \leq |z_{(2)}| \leq |z_{(3)}|$ and expand the determinant:

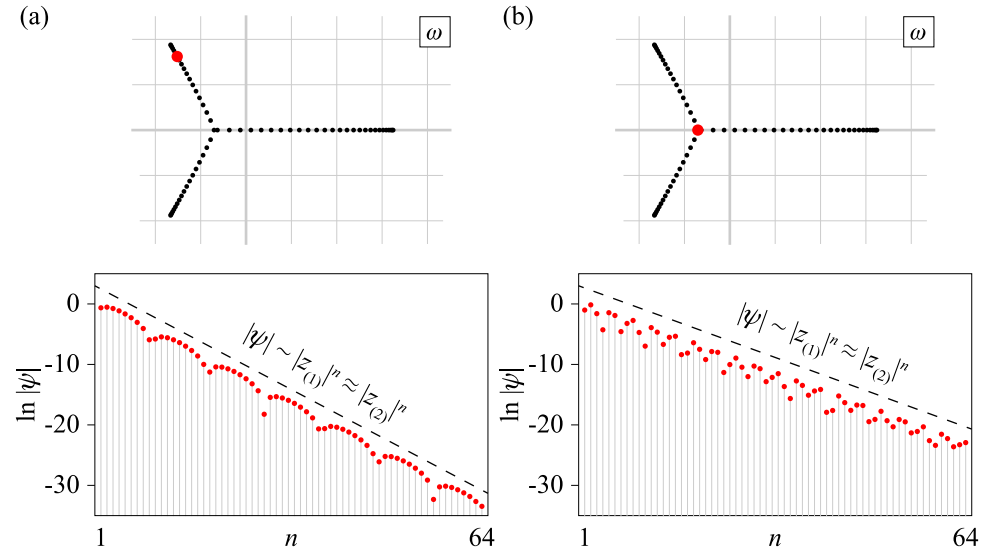
$$z_{(3)}^{N+2}z_{(2)}^{N+1} - z_{(2)}^{N+2}z_{(3)}^{N+1} - z_{(3)}^{N+2}z_{(1)}^{N+1} + z_{(1)}^{N+2}z_{(3)}^{N+1} + z_{(2)}^{N+2}z_{(1)}^{N+1} - z_{(1)}^{N+2}z_{(2)}^{N+1} = 0, \quad (63)$$

where we have sorted the terms according to their magnitudes. Dividing the entire equation by $z_{(3)}^{N+1}z_{(2)}^{N+1}$ results in

$$(z_{(3)} - z_{(2)}) + (z_{(1)} - z_{(3)}) \frac{z_{(1)}^{N+1}}{z_{(2)}^{N+1}} + (z_{(2)} - z_{(1)}) \frac{z_{(1)}^{N+1}}{z_{(3)}^{N+1}} = 0. \quad (64)$$

If $|z_{(1)}| < |z_{(2)}|$, taking the limit results in the $z_{(2)} = z_{(3)}$ condition. This is not possible for the current model, as all the z degeneracies can be enumerated and the modulus

Figure 12



OBC mode profiles for the model $\omega = z^{-1} + z + 3z^2$. (a) Top panel: The OBC spectrum from Fig. 10(c). The frequency $\omega \approx -1.518 + 1.622i$ has been marked with a red dot. Bottom panel: Normalized OBC mode profiles at $\omega \approx -1.518 + 1.622i$. The dashed line indicates the scaling of $|\psi|$ with n . (b) Top panel: The OBC spectrum from Fig. 10(c). The frequency $\omega \approx -0.705$ has been marked with a red dot. Bottom panel: Normalized OBC mode profiles at $\omega \approx -0.705$. The dashed line indicates the scaling of $|\psi|$ with n .

of the degenerate root is always the smallest ($z_{(1)} = z_{(2)}$ instead of $z_{(2)} = z_{(3)}$). As such, for the system to have solutions, the necessary condition would be equal modulus for the two smaller two roots:

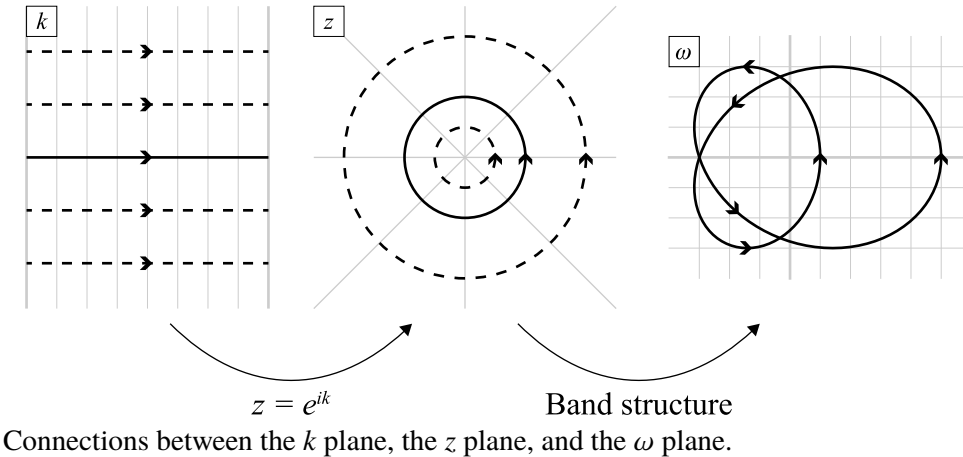
$$|z_{(1)}| = |z_{(2)}|. \quad (65)$$

This condition can then be manipulated algebraically, producing Eq. (58). The relative phase of $z_{(1)}$ and $z_{(2)}$ is not specified, and this phase degree of freedom leads to the $N \rightarrow \infty$ numbers of solutions. The profile of the OBC mode also scales with $|z_{(1)}|^n = |z_{(2)}|^n$ (Fig. 12). A physical interpretation of these observations is given in Section 5. We note that, unlike the Hatano–Nelson model, where the OBC spectrum connects the foci of the ellipse that forms the PBC spectrum, here the OBC spectrum has no apparent connections to the PBC spectrum aside from being enclosed by the PBC spectrum. Although gauge transformations could also be performed on the current model, the transformed Hamiltonian never becomes Hermitian and does not help in calculating the OBC spectrum.

4. SEMI-INFINITE BOUNDARY CONDITIONS AND THE WINDING NUMBER

From the examples given previously, we have seen that the PBC and SIBC spectra of a one-dimensional chain are closely related. The PBC spectrum curve usually divides the complex ω plane into several regions, where different numbers of SIBC modes could be found for a specific ω in each region. This observation can be formulated using the concept of winding number of the PBC spectrum, a topological invariant for the system under the point-gap topology. This, in turn, leads to a bulk–boundary correspondence for non-Hermitian Hamiltonians, which completely specify their SIBC spectrum as the regions with nonzero winding numbers.

Figure 13



Before we explain the new concepts in these statements, it would be useful to take a short detour and look at the complex k , z , and ω planes (Fig. 13), which are frequently used in the following discussions.

The relation between k and z is defined as

$$z = e^{ik}, \quad k = -i \ln z. \quad (66)$$

Here k has a periodicity of 2π and only the strip $0 \leq k_r \leq 2\pi$ needs to be considered. Each horizontal line on the k space with constant k_i maps to a circle on the z plane centered on the origin with radius $\exp(-k_i)$, and each vertical line on the k space with constant k_r maps to a radial line on the z plane with the direction angle given by k_r . The BZ is of particular importance, which shows up on the k plane as the line segment $0 \leq k_r \leq 2\pi$, $k_i = 0$ and on the z plane as $|z| = 1$.

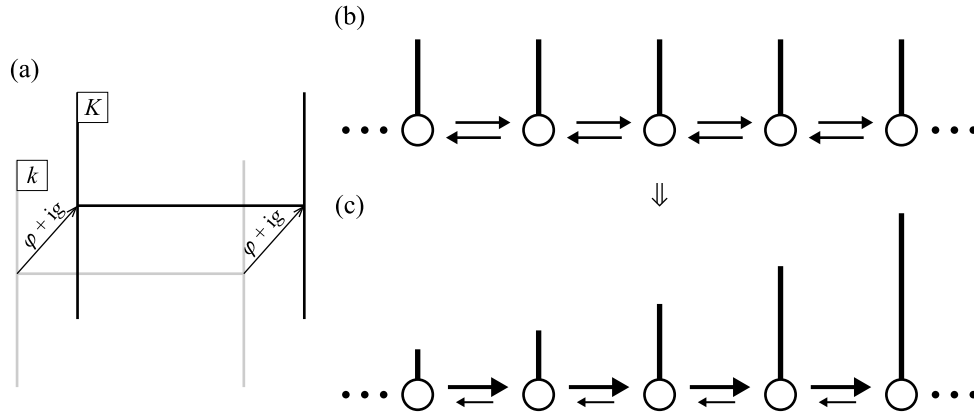
The relation between z and ω is given by the band structure. The mapping from z to ω is single-valued, and the PBC spectra are the result of mapping the BZ ($|z| = 1$) to the ω plane using the band structure function. On the other hand, the mapping from ω to z is multivalued. To be precise, note that each band structure is in the form of a Laurent polynomial as shown in Eq. (9), and can be multiplied by z^p on both sides to give a polynomial equation of z with degree $p + q$. Each ω then corresponds to $p + q$ solutions of z by the fundamental theorem of algebra. The full understanding of such multivalued functions would benefit from the introduction of *branch points*, *branch cuts*, and *Riemann surfaces* [45–48]; the relevance of these concepts to the band structure is collected in Appendix A.

4.1. Iso- $|z|$ Contours and Gauge Transformation

The SIBC for a right-extending chain requires $k_i \geq 0$, and k takes values in the upper strip. The corresponding region in the $|z|$ plane is $|z| \leq 1$, the interior of the unit disk. To understand how the available states are distributed on the ω plane, we consider the constant k_i slices in the k plane, obtained by shifting the BZ by imaginary k values. Each constant k_i line is mapped to an iso- $|z|$ contour on the ω plane by the band structure. As the shifted BZ continuously sweeps upwards across the entire upper strip of k (the unit disk for z), the iso- $|z|$ contour will also sweep across certain regions on the ω plane multiple times, leading to the SIBC spectrum.

As discussed in Section 3.1c, shifting the wave vector can be realized by performing gauge transformations on the model. A general gauge transformation can be

Figure 14



Shifting the BZ is equivalent to gauge transformations. (a) The new K plane is related to the old k plane by a complex shift. (b) In the old model, if the coupling to the left and to the right is the same, the mode will be equally distributed among the cells. (c) In the transformed model, the rightward coupling increases if $g > 0$, and the mode grows exponentially to the right.

represented as

$$\Psi_n = e^{n(g-i\phi)} \psi_n, \quad (67)$$

where ϕ and g are real numbers. The transformation multiplies z by a scaling factor:

$$Z = e^{g-i\phi} z \quad (68)$$

and shifts the wave vector by a constant complex number [Fig. 14(a)]:

$$K = k - (\phi + ig). \quad (69)$$

From here, ϕ and g can be interpreted as the wave vector shift in the real and imaginary directions. If k is on the shifted BZ with $k_i = g$, the shifted wave vector K will be on the BZ with $K_i = 0$.

Substituting the transformed quantities into the band structure, we obtain

$$\omega = \sum_{-p \leq m \leq q} t_m z^m = \sum_{-p \leq m \leq q} (t_m e^{m(i\phi-g)}) Z^m. \quad (70)$$

Therefore, the band structure on the ω plane evaluated on the shifted BZ, which is also the iso- $|z|$ contour with $|z| = \exp(-g)$ and $k_i = g$, can be regarded as the PBC spectrum for the transformed model, where the coupling coefficients have been scaled according to [Figs. 14(b) and 14(c)]

$$T_m = t_m e^{m(i\phi-g)}. \quad (71)$$

By interpreting the shifted and scaled quantities (K , Z , Ψ , and T) as the corresponding quantities for a new model, we can establish a connection between the two models and deduce the properties of one from another. In the following, we use “gauge transformation of a model” to refer to the procedure of deriving a new model from Eq. (71) irrespective of boundary conditions.

4.2. Winding Number and the Point-Gap Topology

A key procedure of calculating the SIBC spectrum is to determine the number of states with $k_i \geq 0$ ($|z| \leq 1$) for a specific ω , as only these states that satisfy the exponential

decay requirement can be used in the linear superposition for the SIBC mode. In other words, of the $p + q$ points on the k plane that maps to the same ω , we need to count the number of points within the upper strip. Here, a state refers to a solution of the band structure at a given ω and z (or k), since each such solution would correspond to a plane wave state that can exist in bulk systems when the boundary conditions are not imposed. As the shifted BZ continuously sweeps toward $k_i \rightarrow \infty$, it will pass through the $k_{(m)}$ points one by one when $k_i = \text{Im}(k_{(m)})$, and the corresponding iso- $|z|$ contour on the ω plane will pass through the ω point. As such, we can convert the problem of counting the number of k to counting the number of times the sweeping contour passes through the ω point.

We demonstrate this process of shifted BZ sweeping with the two example models discussed in Section 3. For the Hatano–Nelson model, the band structure is $\omega = t_R z^{-1} + t_L z$. As an example, we choose $t_L = 2$, $t_R = 1/2$, and select a frequency point $\omega = (3 + i)/2$. The z solutions can be found as $z_{(1)} = (1 - i)/4$ and $z_{(2)} = (1 + i)/2$. Their locations on the k and z plane are shown in Fig. 15(a). The iso- $|z|$ contour for the Hatano–Nelson model is generally an ellipse on the ω plane, and all the ellipses share the same foci. When $|z|$ reaches $|z_{(2)}|$, the contracting ellipse passes through the ω point for the first time [Figs. 15(b) and 15(c)], and the ω point is outside the ellipse immediately after $|z| < |z_{(2)}|$. At $|z| = \sqrt{t_R/t_L}$ the ellipse collapses into a line, and when $|z|$ reaches $|z_{(1)}|$ the ellipse bounces back with an opposite orientation and passes through the ω point for the second time [Figs. 15(d) and 15(e)]. After that, the ellipse keeps expanding and does not pass through the ω point again [Figs. 15(f) and 15(g)].

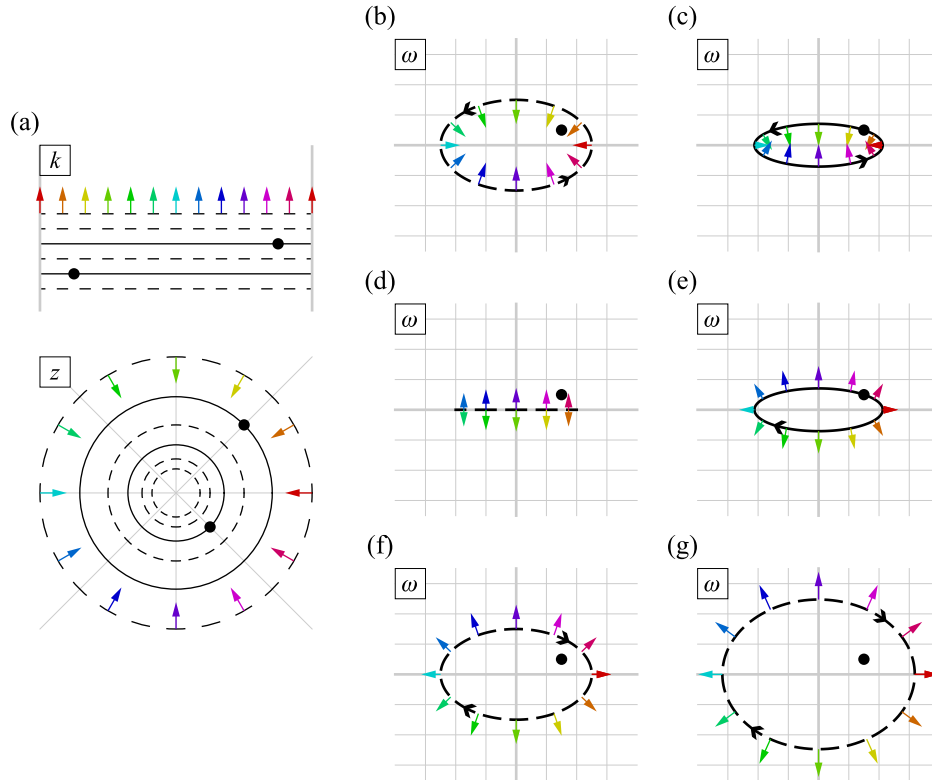
For the band structure given by $\omega = z^{-1} + z + 3z^2$ we have a similar picture (Fig. 16). This time we select the point $\omega = 0$ and the approximate z solutions are $z_{(1)} = 0.245 + 0.587i$, $z_{(2)} = 0.245 - 0.587i$, and $z_{(3)} = -0.824$. In this particular case, we have $|z_{(1)}| = |z_{(2)}|$, where two sections of the contour go through the ω point at the same time in the form of a self-intersection on the contour.

We note that in both cases, the iso- $|z|$ contour always moves toward its left, i.e., its moving direction can be obtained by rotating its traversing direction 90° counterclockwise. This is because the shifted BZ in the z plane also moves to its left during the sweeping process, and the analytic mapping of the band structure preserves orientations. As such, the ω point always passes through a contour segment from its left side to its right side. This motivates us to define a number counting how many times a point is to the left of the entire contour, which would decrease by 1 each time a segment goes through a point to the left.

Now assume that we are standing on the ω point and looking at the contour in the surroundings. Within a narrow view centered on a specific direction, we may observe some contour segments going to the left. If these curves move past the point, the count will decrease by the number of segments, and it would be natural to define the desired number as the total count of the segments [Fig. 17(a)]. If there are both types of curve segments going to the left and to the right, this number should be modified as the count of left-pointing segments minus the count of right-pointing segments, as the ω point appears on the right side of the segment for the latter [Fig. 17(b)]. This definition is independent of the viewing direction, as the loop does not have end points, and the left-pointing and right-pointing segments always appear in pairs when the line of sight becomes tangent to the curve [Fig. 17(c)]. As such, this number effectively describes the number of times the curve circles around the point and is termed the *winding number* w of an oriented loop with respect to the given point.

The winding number can be defined for any point that is not on the loop. It is always an integer, is the same for all points within a continuous region divided by the loop, and

Figure 15



Sweeping of the shifted BZ for the Hatano–Nelson model with $t_L = 2$, $t_R = 1/2$. (a) The z solutions for $\omega = (3 + i)/2$ from the band structure are shown as dots on the k plane (upper panel) and on the z plane (lower panel). The six iso- k_i contours from bottom to top and the six iso- $|z|$ contours from outside to inside correspond to (b)–(g) in that order. Contours intersecting with k and z solutions are solid and other contours are dashed. Colored arrows are placed at equidistant k_r values and point toward larger k_i (smaller $|z|$). (b)–(g) Iso- $|z|$ contours of the band structure on the ω plane. The black dot represents $\omega = (3 + i)/2$. The direction of the contour indicates the direction with increasing k_r [$\text{Arg}(z)$]. Colored arrows correspond to (a) and show the sweeping direction of the contour as k_i increases. Parameters are: (b) $|z| = 1$; (c) $|z| = \sqrt{2}/2$; (d) $|z| = 1/2$; (e) $|z| = \sqrt{2}/4$; (f) $|z| = 1/4$; and (g) $|z| = \sqrt{2}/8$.

decreases by 1 each time a segment of the loop moves past the point from right to left. These properties have already been demonstrated through the above discussions. If the loop is fixed and the point is moving instead, then moving the point past a segment of the loop from left to right also decreases w by 1. To analytically calculate w , consider the angle at ω_0 subtended by a loop segment, given by

$$d\theta = d\text{Arg}(\omega - \omega_0) = \frac{1}{i} \left(\frac{\omega' dz}{\omega - \omega_0} - d \ln |\omega - \omega_0| \right), \quad (72)$$

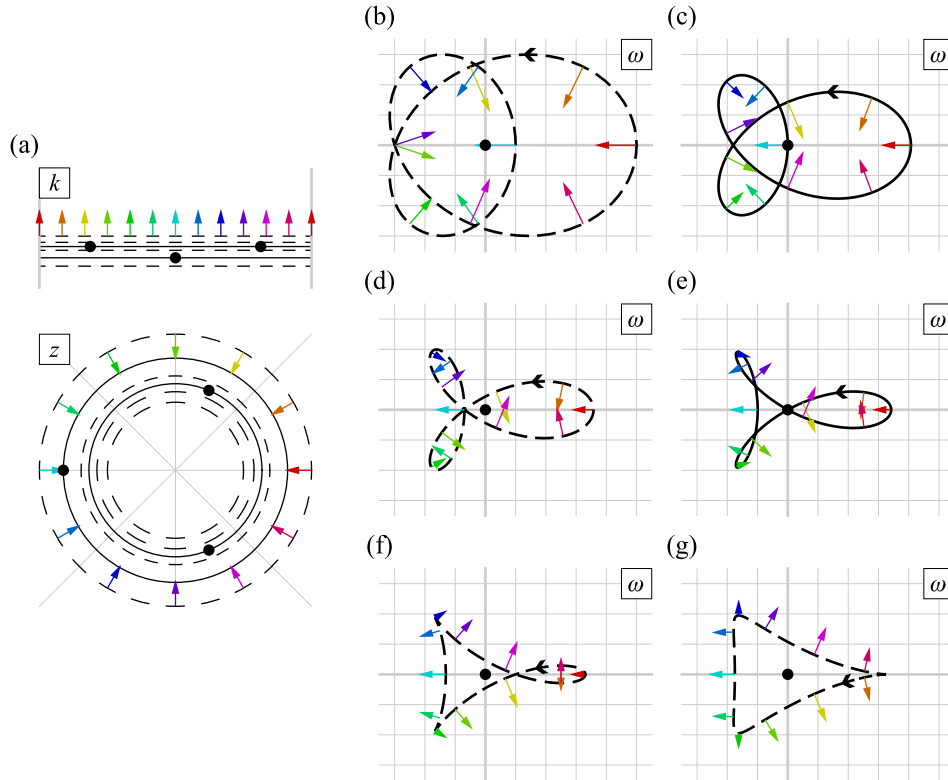
where ω' is the derivative of ω with respect to z . As the point is circled w times, the total angle subtended by the loop should be $2\pi w$. Integration along the loop thus gives

$$2\pi w = \frac{1}{i} \oint_{|z|=1} \frac{\omega'}{\omega - \omega_0} dz \quad (73)$$

or

$$w = \frac{1}{2\pi i} \oint_{|z|=1} \frac{\omega'}{\omega - \omega_0} dz. \quad (74)$$

Figure 16



Sweeping of the shifted BZ for the model $\omega = z^{-1} + z + 3z^2$. (a) The z solutions for $\omega = 0$ from the band structure are shown as dots on the k plane (upper panel) and on the z plane (lower panel). The six iso- k_i contours from bottom to top and the six iso- $|z|$ contours from outside to inside correspond to (b)–(g) in that order. Contours intersecting with k and z solutions are solid and other contours are dashed. Colored arrows are placed at equidistant k_r values and point toward larger k_i (smaller $|z|$). (b)–(g) Iso- $|z|$ contours of the band structure on the ω plane. The black dot represents $\omega = 0$. The direction of the contour indicates the direction with increasing k_r [$\text{Arg}(z)$]. Colored arrows correspond to (a) and show the sweeping direction of the contour as k_i increases. Parameters are: (b) $|z| = 1$; (c) $|z| = 0.824$; (d) $|z| = 0.693$; (e) $|z| = 0.636$; (f) $|z| = 0.577$; and (g) $|z| = 0.5$.

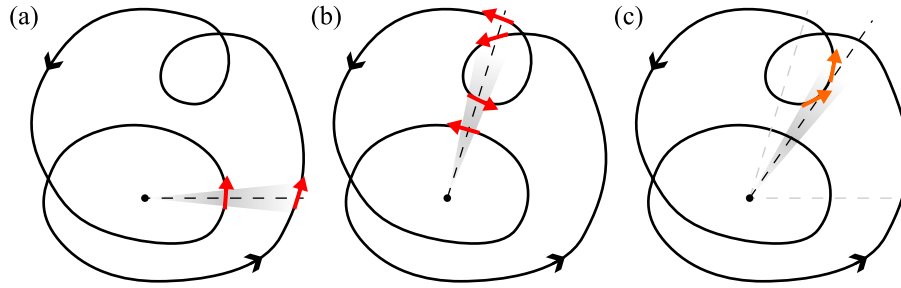
We can now answer the question we posed at the beginning: How many solutions for $z_{(m)}$ are located inside unit disk $|z| \leq 1$ ($k_{(m)}$ solutions in the upper strip) out of a total of $p + q$ solutions? Geometrically, we can sweep the shifted BZ to $k_i \rightarrow +\infty$, and the number becomes the difference between the winding number of the PBC spectrum and the winding number of a scaled model. This scaled model is dominated by the $T_{-p} = t_{-p}e^{pg}$ coupling, which corresponds to the z^{-p} term, and thus has a winding number of $-p$. We conclude that

$$(\text{number of solutions with } |z| \leq 1) = w + p. \quad (75)$$

Alternatively, we interpret Eq. (74) as the *argument principle*, which states that the integral is precisely the number of zeros minus the number of poles for the function $\omega(z) - \omega_0$ (counted with multiplicities):

$$w = \frac{1}{2\pi i} \oint_{|z|=1} \frac{\omega'}{\omega - \omega_0} dz = \#Z[\omega(z) - \omega_0] - \#P[\omega(z) - \omega_0]. \quad (76)$$

Figure 17



Introduction of the winding number. (a) There are two segments pointing to the left when viewed from a certain direction, and the winding number for this point is two. (b) Viewing in another direction, there are three segments pointing to the left and one to the right, and the winding number is again $3 - 1 = 2$. (c) When the viewing direction moves past a tangent direction of the curve, segments pointing in opposite directions appear or disappear in pairs. This ensures that the winding number from (a) and (b) is the same and independent of the viewing direction.

The first term is the quantity we seek (the number of solutions to $\omega(z) = \omega_0$ inside the $|z| = 1$ contour), and the second term is p as the band structure, written as $\omega = \sum_{-p \leq m \leq q} t_m z^m$, has a p th-order pole at the origin (which counts as p poles). Therefore, we arrive at the same conclusion that the number of states for a given ω_0 is given by p plus the winding number of the PBC spectrum with respect to ω_0 .

The importance of the winding number is that it does not change through *continuous deformations*: even if the coupling amplitudes are slightly changed, the number of states satisfying the exponential decay requirement stays the same as long as the PBC spectrum does not pass through the given frequency. The converse is true as well: two models can be continuously morphed into each other while not touching the given frequency if their winding number is the same. It is important to study these continuous deformations as the coupling coefficients may not be exactly as they appear in the model, and may also fluctuate from cell to cell due to disorder (therefore breaking the periodicity assumption).

The requirement that the PBC spectrum does not touch a given frequency ω_0 while deforming leads to the *point-gap topology*. This generalizes the idea of a gap in the Hermitian case, which requires that the bands do not touch a certain real frequency. Although other generalizations such as the line-gap topology are possible, the point-gap topology is the most natural choice for the SIBC spectrum. The winding number, in turn, is a *topological invariant* under the point-gap topology [44,49–52]; it is invariant as long as the change in the model is continuous (passing through the given frequency point would be considered as not continuous under the point-gap topology). Given a fixed ω_0 , a model is *topologically trivial* under the point-gap topology if winding number of the PBC spectrum with respect to ω_0 is zero, and *topologically nontrivial* otherwise. For topologically trivial models, it is possible to tune the coupling parameters and continuously shrink the PBC spectrum to a point, where all unit cells decouple (hence, the triviality). This is not possible for topologically nontrivial models, and the simplest model that can be reduced to is $\omega - \omega_0 = z^w$ with w the winding number, representing unidirectional couplings $|w|$ cell to the right (if $w < 0$) or left (if $w > 0$). We note that the notion of trivial and nontrivial depends on the reference point ω_0 ; the same model can either be topologically nontrivial or trivial, depending on whether the PBC spectrum encloses the reference point ω_0 or not. An alternative definition considers all possible references points, and classifies a model to be trivial if the winding number of the PBC spectrum is zero with respect to every point not on the spectrum, and nontrivial otherwise. With this definition, the PBC spectrum of a

topologically nontrivial model encloses finite areas with nonzero winding numbers, which indicates the existence of the non-Hermitian skin effect (Section 5.3).

4.3. Non-Hermitian Bulk–Boundary Correspondence for Skin Modes

Solving the SIBC modes requires finding all available states and forming linear superpositions out of them while satisfying the boundary conditions. We have solved the former half above and now proceed to the latter half, arriving at a correspondence principle for general non-Hermitian systems.

The general SIBC mode for a right-extending chain can be written as

$$\psi_n = \sum_{m=1}^{p+w} \alpha_{(m)} z_{(m)}^n, \quad (77)$$

where the upper limit of the summation reflects the fact that only the first $p + w$ states satisfy the exponential decay requirement and are available for superposition. The p boundary conditions on the left are $\psi_m = 0$ with m from $-p + 1$ to 0. With the above form for the SIBC mode, the boundary conditions read

$$\alpha_{(1)} z_{(1)}^{-p+1} + \alpha_{(2)} z_{(2)}^{-p+1} + \cdots + \alpha_{(p+w)} z_{(p+w)}^{-p+1} = 0, \quad (78)$$

$$\alpha_{(1)} z_{(1)}^{-p+2} + \alpha_{(2)} z_{(2)}^{-p+2} + \cdots + \alpha_{(p+w)} z_{(p+w)}^{-p+2} = 0, \quad (79)$$

\vdots

$$\alpha_{(1)} z_{(1)}^0 + \alpha_{(2)} z_{(2)}^0 + \cdots + \alpha_{(p+w)} z_{(p+w)}^0 = 0. \quad (80)$$

These can be viewed as a set of linear equations for the amplitudes:

$$V_{\text{single}} (\alpha_{(1)}, \alpha_{(2)}, \dots, \alpha_{(p+w)})^T = 0, \quad (81)$$

$$V_{\text{single}} = \begin{bmatrix} z_{(1)}^{-p+1} & z_{(2)}^{-p+1} & \cdots & z_{(p+w)}^{-p+1} \\ z_{(1)}^{-p+2} & z_{(2)}^{-p+2} & \cdots & z_{(p+w)}^{-p+2} \\ \vdots & \vdots & \ddots & \vdots \\ z_{(1)}^0 & z_{(2)}^0 & \cdots & z_{(p+w)}^0 \end{bmatrix}. \quad (82)$$

The coefficient matrix V_{single} for single-band models is made of $z_{(1)}$ to $z_{(p+w)}$ raised to powers of consecutive integers ($-p + 1$ to 0), and forms a *Vandermonde matrix* [53]. It is guaranteed to be full rank when all $z_{(m)}$ are distinct. As such, the p constraints will remove p degrees of freedom from the superposition, leaving w degrees of freedom that correspond to w independent modes. Therefore, for each frequency that has a winding number of w for the PBC spectrum, exactly w SIBC modes can be found in the system for that frequency. If $w \leq 0$, the system is overdetermined, and no SIBC modes can be found.

A completely analogous procedure can be carried out for a left-extending chain. This time we take the last $q - w$ states for superposition, resulting in

$$\psi_n = \sum_{m=p+w+1}^{p+q} \alpha_{(m)} z_{(m)}^n. \quad (83)$$

The q boundary condition removes q degrees of freedom, leaving $-w$ modes in the system. If $w \geq 0$, the system is overdetermined, and no SIBC modes can be found.

To summarize, we have the full statement of the *bulk–boundary correspondence* for one-dimensional, single-band non-Hermitian systems [49]:

The winding number w of the PBC spectrum with respect to a specific complex frequency point ω_0 corresponds to the number of SIBC modes with frequency ω_0 that can be found in the system. If $w > 0$, then w modes can be found on the left edge of a right-extending chain with frequency ω_0 ; if $w < 0$, then $-w$ modes can be found on the right edge of a left-extending chain with frequency ω_0 ; if $w = 0$, then no modes with frequency ω_0 can be found in either the right-extending or the left-extending chain.

The bulk–boundary correspondence indicates that the SIBC spectrum for a right-extending chain consists of the regions inside the PBC spectrum with positive winding numbers. The modes found in these regions are all skin modes in the sense that these modes are not isolated on the complex ω plane and the mode profile changes continuously with respect to ω_0 changes within the same region.

We note that this non-Hermitian bulk–boundary correspondence features some differences compared with the usual bulk–boundary correspondences for one-dimensional Hermitian systems in condensed matter theory. All bulk–boundary correspondences relate the boundary (SIBC) spectrum (specifically in the discussion here, the number of SIBC modes at a certain frequency) to the bulk (PBC) spectrum. However, the non-Hermitian correspondence based on the point-gap topology does not require any symmetry constraints on H , whereas the Hermitian correspondences require H to possess time-reversal, chiral, particle–hole, or other similar symmetry in one dimension [50,51]. As such, the non-Hermitian correspondence is capable of determining the SIBC spectrum over the entire ω plane by changing the reference point ω_0 , while the Hermitian correspondences only concerns modes at isolated points in frequency. In addition, whereas the non-Hermitian correspondence counts *skin modes* based on the topology of *eigenvalues* alone, the Hermitian correspondences count *edge modes* based on the topology of *eigenvectors*, and can only appear in multiband systems (detailed discussions on multiband systems and edge modes can be found in Section 6).

The bulk–boundary correspondence holds for tight-binding models as well as non-tight-binding models; see Appendix B for details.

4.4. Degenerate Cases

Up to now, we have been carefully avoiding the case when some of the $z_{(m)}$ solutions from the band structure are not distinct. In the presence of such degenerate solutions, the states of the system do not need to be in the form of $\exp(ikn)$ in order to have a single frequency in the dynamics, which breaks a very early assumption we have made [Eq. (5)]. Although such cases are not generic, as SIBC spectra consist of continuous regions and small perturbations within the region will lift the z degeneracy, we nonetheless provide a discussion of such cases for completeness.

The dynamics of the chain are given by

$$-i\omega\psi_n = -i \sum_{-p \leq m \leq q} t_m \psi_{n+m}. \quad (84)$$

To deduce the possible forms a state can take, we view this equation as a *linear recurrence relation* [54], which provides the value of ψ_{n+q} when all the ψ values to its left are known:

$$\psi_{n+q} = \frac{1}{t_q} \left(\omega\psi_n - \sum_{-p \leq m \leq q-1} t_m \psi_{n+m} \right). \quad (85)$$

The theory of linear recurrence relations requires the solutions to the characteristic polynomial, obtained by formally replacing $\psi_{n+m} \rightarrow z^m$:

$$t_q z^q = \omega - \sum_{-p \leq m \leq q-1} t_m z^m, \quad (86)$$

which is identical to the band structure equation. If all solutions $z_{(m)}$ are distinct, then the general solution can be found as

$$\psi_n = \sum_{m=1}^{p+q} \alpha_{(m)} z_{(m)}^n. \quad (87)$$

If some of the $z_{(m)}$ are identical, then each time a duplicate appears, the corresponding state acquires a term with an extra factor of n . For example, if we have $z_{(1)} = z_{(2)} = z_{(3)}$ and $z_{(4)} = z_{(5)}$, the mode profile would be given by

$$\psi_n = \alpha_{(1)} z_{(1)}^n + \alpha_{(2)} n z_{(1)}^n + \alpha_{(3)} n^2 z_{(1)}^n + \alpha_{(4)} z_{(4)}^n + \alpha_{(5)} n z_{(4)}^n. \quad (88)$$

From here, the boundary condition can be imposed as usual by requiring $\psi_m = 0$ with m from $-p + 1$ to 0 . The coefficients for the amplitudes form a *confluent Vandermonde matrix*, which has a full rank similar to the Vandermonde matrix, and the numbers of SIBC modes remain the same.

The exponential decay requirement is more subtle as the states are no longer plane waves. If $|z_{(m)}| < 1$, the state in the form of $n^s z^n$ should still be considered as an exponentially decaying state, since the large n behavior is dominated by the exponential factor. The borderline case is $|z_{(m)}| = 1$, where the z^n state is bounded and the $n^s z^n$ states will diverge as $n \rightarrow \infty$ with $s \geq 1$. It is beneficial to include the z^n state in the SIBC spectrum even if it does not decay (as all Hermitian states belong to this case), but there are different circumstances regarding the $n^s z^n$ case. By only requiring that the state does not diverge exponentially, we have included both the z^n and the $n^s z^n$ states in the SIBC spectrum. This simplifies the SIBC feasible region to be the entire unit disk $|z| \leq 1$ without discussing the degenerate cases separately. This distinction does not affect the bulk–boundary correspondence, as winding numbers are left undefined when the PBC spectrum loop passes through the point, thereby excluding the $|z| = 1$ case altogether.

5. OPEN BOUNDARY CONDITIONS AND THE GENERALIZED BRILLOUIN ZONE

As we have seen from the examples in Section 3.2, the OBC spectra may differ qualitatively from the corresponding PBC spectra and can get complicated very quickly even for simple models. This difference follows from the different behaviors of PBC and OBC spectra under gauge transformations. If an OBC mode $(\psi_1, \psi_2, \dots, \psi_N)$ can be found in a system with band structure $\omega = \sum_{-p \leq m \leq q} t_m z^m$, then we can perform gauge transformation on both the mode and the coupling coefficients, resulting in a scaled mode $(\lambda^{-1} \psi_1, \lambda^{-2} \psi_2, \dots, \lambda^{-N} \psi_N)$ and a scaled system $\omega = \sum_{-p \leq m \leq q} (t_m \lambda^{-m}) (\lambda z)^m$, where λ is the scaling parameter. It can be easily verified that the scaled mode satisfies the dynamics in the scaled system with the same frequency ω . As such, an entire family of models related by gauge transformations shares the same OBC spectrum [27,52,55]. If any feature of a particular PBC spectrum carries over to the OBC spectrum, the same feature must be found in all other transformed models, which would exclude many specific properties such as the detailed shape and the enclosed regions.

In the following, we show that the condition of two $|z|$ being equal, as found in Section 3 [Eqs. (25), (38), and (65)], is the condition that generalizes to arbitrary systems in the $N \rightarrow \infty$ limit [44,56,57]. This condition is invariant with respect to gauge transformations and is therefore consistent with the previous discussion. We also introduce related concepts such as the GBZ [27,56] and show that the discrepancy between OBC and PBC spectra is an example of the extreme sensitivity of the spectrum on the boundary conditions.

5.1. Condition for Mode Existence

For a band structure given by $\omega = \sum_{-p \leq m \leq q} t_m z^m$, where p (q) is the furthest range of coupling from the left (right), the OBC mode can be expressed as

$$\psi_n = \sum_{m=1}^{p+q} \alpha_{(m)} z_{(m)}^n, \quad (89)$$

where $\alpha_{(m)}$ is the undetermined coefficients for the superposition and $z_{(m)}$ are the $p + q$ solutions from the band structure for a specific ω and sorted in nondecreasing amplitude. We again consider generic ω first, where all $z_{(m)}$ are distinct.

As demonstrated in Section 3.2, there will be p boundary conditions at the left side of the chain, from $\psi_{-p+1} = 0$ to $\psi_0 = 0$; similarly, there will be q boundary conditions at the right, from $\psi_{N+1} = 0$ to $\psi_{N+q} = 0$. Together these constraints form a set of linear equations on the coefficients:

$$\begin{bmatrix} z_{(1)}^{-p+1} & z_{(2)}^{-p+1} & \cdots & z_{(p+q)}^{-p+1} \\ \vdots & \vdots & \vdots & \vdots \\ z_{(1)}^0 & z_{(2)}^0 & \cdots & z_{(p+q)}^0 \\ z_{(1)}^{N+1} & z_{(2)}^{N+1} & \cdots & z_{(p+q)}^{N+1} \\ \vdots & \vdots & \vdots & \vdots \\ z_{(1)}^{N+q} & z_{(2)}^{N+q} & \cdots & z_{(p+q)}^{N+q} \end{bmatrix} \begin{bmatrix} \alpha_{(1)} \\ \alpha_{(2)} \\ \vdots \\ \alpha_{(p+q)} \end{bmatrix} = 0. \quad (90)$$

As the number of amplitudes equals the number of equations, the system has nonzero solutions only when the determinant vanishes, which becomes a requirement on the values of z and, in turn, ω . We note that this determinant is *not* a Vandermonde determinant, as the exponents are not consecutive integers, making it possible to vanish for specific values of $z_{(m)}$.

5.1a. Mathematical Argument

We first provide a purely mathematical argument on when OBC modes can be found when $N \rightarrow \infty$ by directly expanding the determinant. We observe that the modulus of each term will scale differently when N is large; for example, the term from the main diagonal scales as $|z_{(p+1)} z_{(p+2)} \cdots z_{(p+q)}|^N$, whereas the term from the anti-diagonal scales as $|z_{(1)} z_{(2)} \cdots z_{(q)}|^N$. As we are adding together many terms with different scaling, we expect that the result is dominated by its asymptotically largest terms. As each term contain q monomials in the form of z^N where each z is different, the largest term would be to assign the largest $|z|$ to the monomials, resulting in $|z_{(p+1)} z_{(p+2)} \cdots z_{(p+q)}|^N$. The second largest term would be to replace $z_{(p+1)}$ with $z_{(p)}$; replacing any other z would lead to a smaller term. Using a minor expansion and grouping these two terms together, we arrive at

$$\begin{aligned} & \left| \begin{array}{cccc} z_{(1)}^{-p+1} & \cdots & z_{(p-1)}^{-p+1} & z_{(p)}^{-p+1} \\ \vdots & \vdots & \vdots & \vdots \\ z_{(1)}^0 & \cdots & z_{(p-1)}^0 & z_{(p)}^0 \end{array} \right| \left| \begin{array}{cccc} z_{(p+1)}^1 & z_{(p+2)}^1 & \cdots & z_{(p+q)}^1 \\ \vdots & \vdots & \vdots & \vdots \\ z_{(p+1)}^q & z_{(p+2)}^q & \cdots & z_{(p+q)}^q \end{array} \right| [z_{(p+1)} z_{(p+2)} \cdots z_{(p+q)}]^N \\ & - \left| \begin{array}{cccc} z_{(1)}^{-p+1} & \cdots & z_{(p-1)}^{-p+1} & z_{(p+1)}^{-p+1} \\ \vdots & \vdots & \vdots & \vdots \\ z_{(1)}^0 & \cdots & z_{(p-1)}^0 & z_{(p+1)}^0 \end{array} \right| \left| \begin{array}{cccc} z_{(p)}^1 & z_{(p+2)}^1 & \cdots & z_{(p+q)}^1 \\ \vdots & \vdots & \vdots & \vdots \\ z_{(p)}^q & z_{(p+2)}^q & \cdots & z_{(p+q)}^q \end{array} \right| [z_{(p)} z_{(p+2)} \cdots z_{(p+q)}]^N \\ & + \text{exponentially smaller terms} = 0. \end{aligned} \quad (91)$$

Here, the coefficients out front are all Vandermonde determinants, which cannot vanish if all z are distinct, and these two terms are the actual two largest terms in the entire

determinant. By moving the first term to the other side of the equation and taking logarithms, we conclude that

$$\ln \left| \frac{z_{(p+1)}}{z_{(p)}} \right| = \frac{1}{N} \ln \left| \prod_{m=1}^{p-1} \frac{z_{(p+1)} - z_{(m)}}{z_{(p)} - z_{(m)}} \prod_{m=p+2}^{p+q} \frac{z_{(p)} - z_{(m)}}{z_{(p+1)} - z_{(m)}} + \text{exponentially smaller terms} \right| \rightarrow 0. \quad (92)$$

Therefore, a necessary condition for the OBC mode to exist in the $N \rightarrow \infty$ limit is that

$$|z_{(p)}| = |z_{(p+1)}|. \quad (93)$$

Although only p appears explicitly in Eq. (93), the condition is symmetric in p and q , as the p th and $(p + 1)$ th solution of z sorted in nondecreasing amplitude becomes the $(q + 1)$ th and q th solution sorted in nonincreasing amplitude. This is also consistent with the fact that the OBC spectrum remains the same if the entire chain is flipped horizontally, which replaces z with z^{-1} in the Hamiltonian, interchanges p and q , and reverses the ranking of z solutions.

Although Eq. (93) is also sufficient for the OBC spectrum (i.e., every ω point with $|z_{(p)}| = |z_{(p+1)}|$ is included in the OBC spectrum), the complete proof of the sufficiency part is outside the scope of this tutorial (see Appendix B for a brief discussion).

5.1b. Physical Argument

It is important to note that the condition $|z_{(p)}| = |z_{(p+1)}|$ concerns specifically the p th and the $(p + 1)$ th solution of z sorted in nondecreasing amplitude, rather than two arbitrary solutions. In the following, we provide a more physical argument for this by separately matching the mode to the boundary conditions on the left and right edges, borrowing ideas from the SIBC analysis given previously.

For the mode profile given by $\psi_n = \sum_{m=1}^{p+q} \alpha_{(m)} z_{(m)}^n$, the p boundary condition on the left edge will impose p constraints. This allows us to solve $\alpha_{(1)}$ to $\alpha_{(p)}$ in terms of $\alpha_{(p+1)}$ to $\alpha_{(p+q)}$. The coefficient matrix involved is a Vandermonde matrix, which has full rank when all $z_{(m)}$ are distinct. Therefore, we can choose the remaining q amplitudes, $\alpha_{(p+1)}$ to $\alpha_{(p+q)}$, as the amplitudes for the q independent states satisfying the left boundary conditions. Each state has different asymptotic behavior in the bulk, with $|\psi_n| \sim |z_{(p+1)}|^n$ for the state for $\alpha_{(p+1)}$, $|\psi_n| \sim |z_{(p+2)}|^n$ for the state for $\alpha_{(p+2)}$, and so on. The combination of these states, however, will always decay slower than the fastest-decaying one, i.e.,

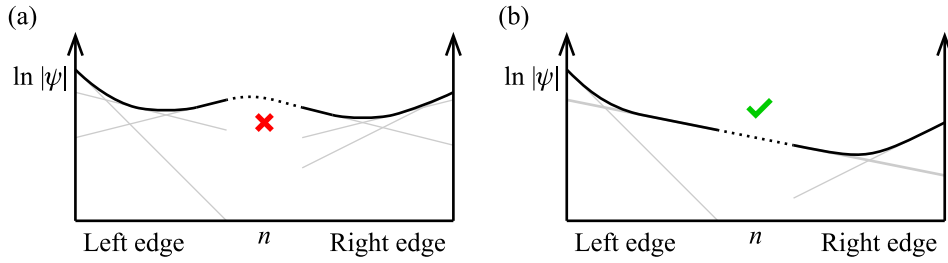
$$\lim_{n \rightarrow \infty} \frac{1}{n} \ln |\psi_n| \geq \ln |z_{(p+1)}|. \quad (94)$$

For the right edge, with a completely analogous argument, we can take $\alpha_{(1)}$ to $\alpha_{(p)}$ as the independent amplitudes, and the combination of states satisfying the right boundary condition will decay slower (to the left) than the fastest-decaying one:

$$\lim_{n \rightarrow \infty} \frac{1}{n} \ln |\psi_{-n}| \geq -\ln |z_{(p)}|. \quad (95)$$

If an OBC mode satisfies both boundary conditions, then somewhere in the middle of the chain, the mode will decay no faster than $\ln |z_{(p+1)}|$ but no slower than $\ln |z_{(p)}|$ [Fig. 18(a)]. Given that $|z_{(p+1)}| \geq |z_{(p)}|$, the only possibility is that $|z_{(p)}| = |z_{(p+1)}|$, which is also the scaling behavior of the actual OBC mode in the middle of the chain [Fig. 18(b)]. This again demonstrates that the two z in the condition are specifically the p th and the $(p + 1)$ th ones, as the ordering relates to the number of boundary conditions that need to be matched on each side.

Figure 18



OBC spectrum condition explained as a constraint of the mode growth rate. The schematic assumes $p = q = 2$. Gray lines are the asymptotics given by each $z_{(m)}$ and the black curve shows the superimposed mode profile satisfying boundary conditions at each edge separately. (a) If $|z_{(2)}| < |z_{(3)}|$, the mode behavior does not agree in the middle of the chain, and cannot be matched to form a mode that satisfies boundary conditions at both edges. (b) If $|z_{(2)}| = |z_{(3)}|$, it is possible to match the mode in the middle of the chain, resulting in a valid OBC mode.

5.1c. Degeneracy Issues

It is tempting to simply set $z_{(m_1)} = z_{(m_2)}$ with two arbitrary solutions, which makes the determinant in Eq. (90) vanish, and claim that these z degeneracy points are all in the OBC spectrum. However, as discussed in Section 4.4, the inclusion of identical $z_{(m)}$ will change the state profile to $n^s z^n$, and the determinant will change accordingly. Again we take the example of $z_{(1)} = z_{(2)} = z_{(3)}$ and $z_{(4)} = z_{(5)}$, with the mode profile given by

$$\psi_n = \alpha_{(1)} z_{(1)}^n + \alpha_{(2)} n z_{(1)}^n + \alpha_{(3)} n^2 z_{(1)}^n + \alpha_{(4)} z_{(4)}^n + \alpha_{(5)} n z_{(4)}^n. \quad (96)$$

Suppose that the model has $p = 4$ and $q = 1$. We impose four boundary conditions on the left and one on the right, which leads to

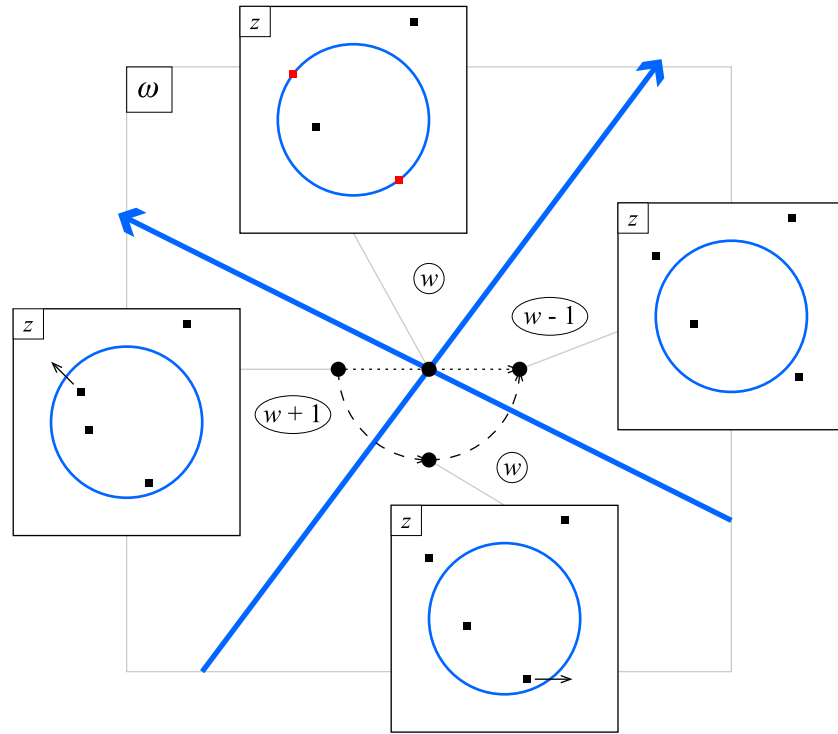
$$\begin{vmatrix} z_{(1)}^{-3} & -3z_{(1)}^{-3} & 9z_{(1)}^{-3} & z_{(4)}^{-3} & -3z_{(4)}^{-3} \\ z_{(1)}^{-2} & -2z_{(1)}^{-2} & 4z_{(1)}^{-2} & z_{(4)}^{-2} & -2z_{(4)}^{-2} \\ z_{(1)}^{-1} & -z_{(1)}^{-1} & z_{(1)}^{-1} & z_{(4)}^{-1} & -z_{(4)}^{-1} \\ 1 & 0 & 0 & 1 & 0 \\ z_{(1)}^{N+1} & (N+1)z_{(1)}^{N+1} & (N+1)^2 z_{(1)}^{N+1} & z_{(4)}^{N+1} & (N+1)z_{(4)}^{N+1} \end{vmatrix} = 0. \quad (97)$$

This determinant is generally nonvanishing and therefore imposes additional constraints on the z and ω values in addition to the z degeneracy criterion. As the zero determinant above and the z degeneracy are algebraically independent constraints, they cannot be both satisfied in general and the degeneracy points are not on the OBC spectrum. The only exception is when the ω at the degeneracy point also satisfies $|z_{(p)}| = |z_{(p+1)}|$. As $z_{(p)} = z_{(p+1)}$ implies $|z_{(p)}| = |z_{(p+1)}|$, the ω points where $z_{(p)} = z_{(p+1)}$ will be on the OBC spectrum for $N \rightarrow \infty$.

5.2. Spectrum Properties and the GBZ

The form of $|z_{(p)}| = |z_{(p+1)}|$ suggests that it can be connected to the iso- $|z|$ contours discussed in Section 4. In fact, if the $|z| = z_0$ contour on the ω plane has self-intersections, then at each self-intersection point there are at least two z solutions with the same $|z|$ for the same ω . However, not all such intersections are on the OBC spectrum, as the z_0 may not correspond to $|z_{(p)}|$ and $|z_{(p+1)}|$, but to solutions with other rankings. Figure 10 provides a concrete example: none of the three self-intersection points of the PBC curve are on the OBC spectrum, as they correspond to $|z_{(2)}| = |z_{(3)}|$ rather than $|z_{(1)}| = |z_{(2)}|$.

Figure 19

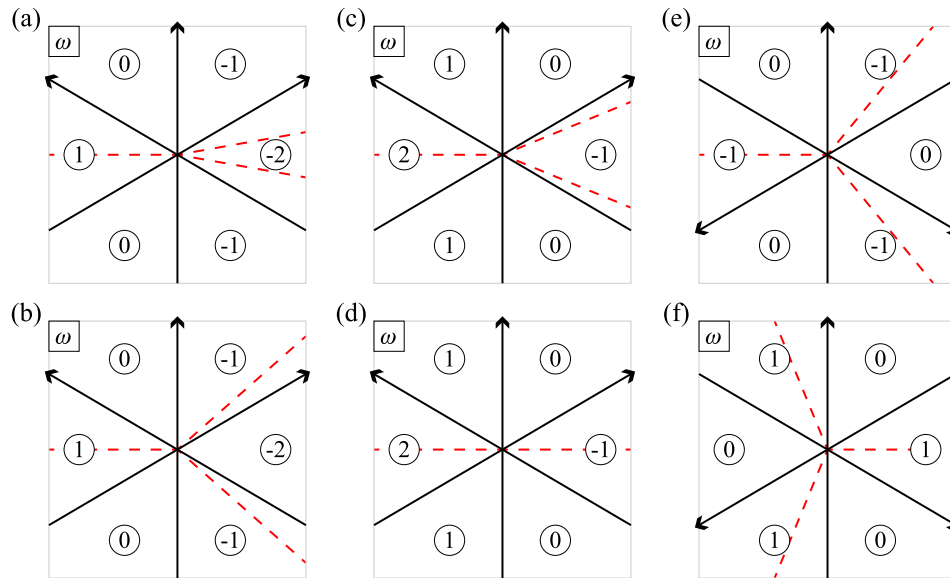


Schematic of an iso- $|z|$ contour self-intersection (blue arrows) in the ω plane. The ω plane is divided into regions with different winding numbers, represented by circled numbers $w + 1$, w , and $w - 1$. Insets show the relative locations of the z solutions (squares) for each ω point and the $|z| = z_0$ contour (blue circles), assuming $p = q = 2$. When the ω point in the $w + 1$ region moves to the $w - 1$ region along the dashed curve, $z_{(3)}$ and $z_{(2)}$ solutions cross the $|z| = z_0$ circle in succession. When the path is deformed to pass through the intersection point (dotted line), $z_{(3)}$ and $z_{(2)}$ solutions cross the $|z| = z_0$ circle at the same time.

To determine what kind of self-intersection points are actually on the OBC spectrum, we need to know the ranking number of a point on the $|z| = z_0$ contour compared with all other z solutions, i.e., how many other z solutions have a magnitude below z_0 . From the SIBC discussion (Section 4.2), this is directly related to the winding number: the number of solutions with a magnitude below $|z| = z_0$ at a certain ω point is given by p plus the winding number of the $|z| = z_0$ contour for that point.

We consider the simplest self-intersection, where only two parts of the iso- $|z|$ contour intersect (see Fig. 19). If more than two segments of the contour meet at the same point, we can perturb the z_0 value slightly to separate them and return to the original configuration with a continuity argument. We take the loop orientation as the direction of increasing $\text{Arg}(z)$ so the winding number with respect to points not on the contour can be defined. We now assume that the winding number for the region to the left of both segments is $w + 1$. As crossing the curve from left to right reduces the winding number by 1, the two regions between both segments have a winding number of w , and the region to the right of both segments has a winding number of $w - 1$. For ω points in the left region, the winding numbers indicate that there are $w + 1 + p$ solutions for z with a magnitude below $|z| = z_0$. When ω crosses one segment of the curve, the $(w + 1 + p)$ th solution $z_{(w+1+p)}$ crosses over the $|z| = z_0$ circle, and when ω crosses another segment of the curve, the $(w + p)$ th solution $z_{(w+p)}$ also crosses over the $|z| = z_0$ circle. If this ω path is deformed so that it passes through the intersection, the $z_{(w+1+p)}$

Figure 20



Schematics of self-intersection points with three iso- $|z|$ contour segments (black) and some possible shapes of the local OBC spectra (red). Winding numbers for each region divided by the contour are represented by circled numbers. The extending directions of the OBC spectra are not exhaustive and depend on the model parameters. (a),(b) Three segments going in the same direction, with winding numbers from -2 to 1 . (c),(d) Three segments going in the same direction, with winding numbers from -1 to 2 . (e) Three segments going in alternating directions, with winding numbers from -1 to 0 . (f) Three segments going in alternating directions, with winding numbers from 0 to 1 .

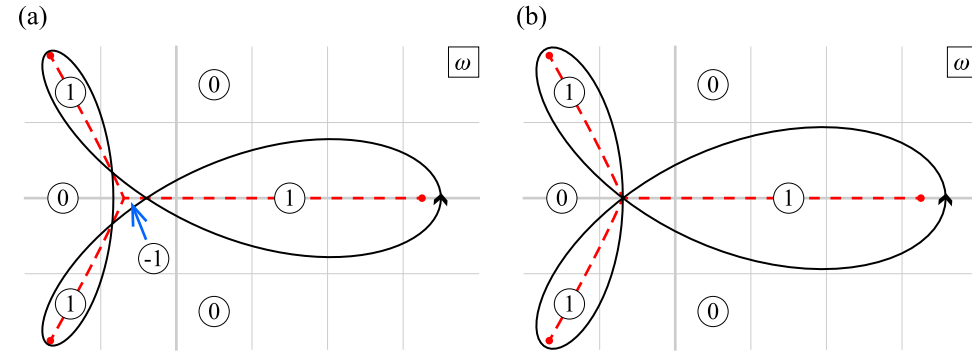
and $z_{(w+p)}$ crosses $|z| = z_0$ at the same time, indicating that $|z_{(w+1+p)}| = |z_{(w+p)}| = z_0$. For the OBC spectrum, we require that $|z_{(p)}| = |z_{(p+1)}|$, and comparison gives

$$w = 0. \quad (98)$$

In other words, for the self-intersection point to be in the OBC spectrum, it should be that sandwiched between regions with winding numbers 1 and -1 [58]. A slightly modified version of the same statement generalizes to self-intersection points with multiple segments: the self-intersection point is contained in the OBC if and only if the winding number of a region plus the number of segments having this region on their right side is positive, and the winding number of a region minus the number of segments having this region on their left side is negative (the sum and difference represent the maximum and minimum attainable winding numbers in the vicinity of the self-intersection point when perturbation is applied). All configurations of self-intersection points with three segments that are on the OBC spectra can be found in Fig. 20. Figure 21 demonstrates the relation of the OBC spectrum and contour self-intersections for the example model used in Section 3.2. In Fig. 21(a), the iso- $|z|$ contour at $|z| = 2/3$ is selected and all the self-intersection points are on the OBC spectrum. In Fig. 21(b), the contour value leads to a self-intersection point with three contour segments, which becomes the meeting point of the three arcs in the OBC spectrum [see also Figs. 16(d) and 20(f)].

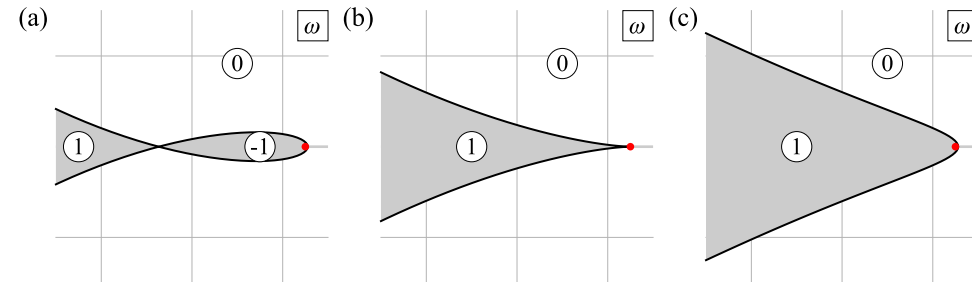
As the OBC spectrum is given by $|z_{(p)}| = |z_{(p+1)}|$, it can be viewed as the collection of all $|z_{(p)}| = |z_{(p+1)}| = z_0$ points where z_0 varies. Therefore, the OBC spectrum can also be constructed by drawing every iso- $|z|$ contour, identifying the correct

Figure 21



OBC spectrum and the iso- $|z|$ contours for the model $\omega = z^{-1} + z + 3z^2$. Winding numbers of different regions are represented by circled numbers. Contour levels are (a) $|z| = 2/3 \approx 0.667$ and (b) $|z| = 3^{-1/3} \approx 0.693$.

Figure 22



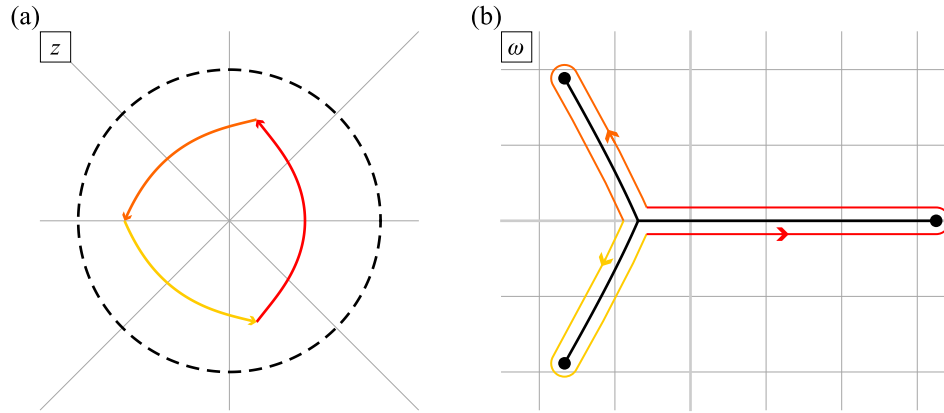
OBC spectrum and three iso- $|z|$ contours for the model $\omega = z^{-1} + z + 3z^2$. Contour levels are (a) $|z| = 9/20$; (b) $|z| = 1/2$ (critical value); (c) $|z| = 11/20$. All plots are zoomed in around the branch point $\omega = 13/4$ (shown as the red point) to show the details of the curves. Winding numbers of different regions are also marked.

self-intersections, and collecting them together. This gives another explanation of why the OBC spectrum does not look like the corresponding PBC spectrum, as only some of the self-intersection points of the PBC spectrum could be on the OBC spectrum. A corollary of this interpretation is that the points on the OBC spectrum are exactly the ω points where the winding number for the $|z| = z_0$ contour jumps from negative integers to positive integers as z_0 increases; they never have a winding number of 0, which can also be verified in Fig. 21.

The self-intersection points trace out continuous arcs as z_0 varies in the $|z| = z_0$ contour. When the contour closes on itself, the self-intersection point no longer exists beyond a certain z_0 (Fig. 22), forming a termination point of the arcs. At the critical value, the iso- $|z|$ contour curves form cusps, where $[\partial\omega/\partial\text{Arg}(z)]|_{|z|} = 0$. As ω is analytic in z , this is equivalent to $\partial_z\omega = 0$, indicating that the termination points are always branch points that additionally satisfy $z_{(p)} = z_{(p+1)}$ (see Appendix A for the relation between branch points and z degeneracy). This provides a means to enumerate all possible termination points for the OBC spectrum and an estimation of its extent on the ω plane.

We take the model $\omega = z^{-1} + z + 3z^2$ as an example; the full OBC spectrum is shown in Fig. 10. After rewriting the band structure as a polynomial in z (i.e., $3z^3 + z^2 - \omega z + 1 =$

Figure 23



GBZ for the model $\omega = z^{-1} + z + 3z^2$. (a) The GBZ in the z plane. The dashed circle is the BZ $|z| = 1$. (b) As the z point moves along the GBZ, the corresponding ω moves along the OBC spectrum. Each colored section in (a) corresponds to an arc of the OBC spectrum and the entire OBC spectrum is covered. Note that the trajectory has been offset from the OBC spectrum for clarity; the actual point travels on the spectrum back and forth.

0), the branch points can be found by setting the *discriminant* to zero (Appendix A):

$$12\omega^3 + \omega^2 - 54\omega - 247 = 0, \quad (99)$$

$$\omega = \frac{13}{4}, \quad \omega = \frac{-5 + 4\sqrt{2}i}{3}, \quad \omega = \frac{-5 - 4\sqrt{2}i}{3}. \quad (100)$$

All three points satisfy $z_{(1)} = z_{(2)}$, and the OBC spectrum indeed terminates on these points.

The graph of the OBC spectrum, where arcs connect certain branch points together, resembles the branch cuts drawn for multivalued functions. It turns out that the OBC spectrum defines a branch cut of the multivalued map from ω to z , where the single-valued branches are determined by $|z|$ [59,60] (see Appendix A). In addition, although the OBC spectrum may possess interesting features in terms of its graph topology [61,62], it is always a single connected component for single-band models.

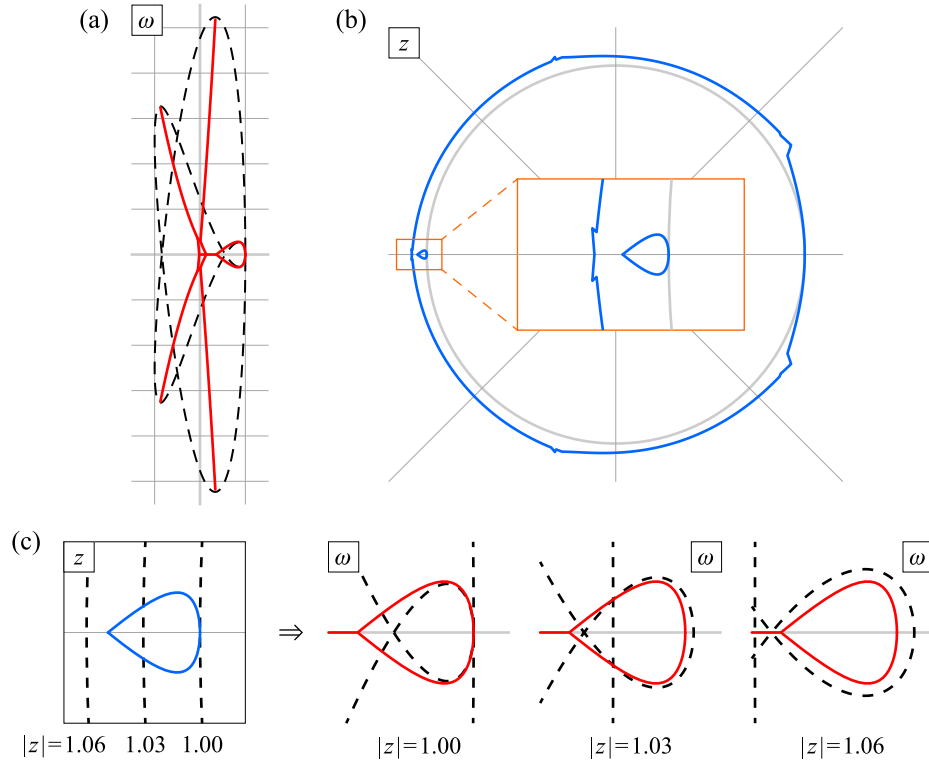
We now turn our attention to the z plane, where we can draw the $z_{(p)}$ and $z_{(p+1)}$ values that correspond to ω values on the OBC spectrum. The collection of these z values is known as the GBZ [27,56], termed as such because this reduces to the BZ of $|z| = 1$ for Hermitian models. For one-dimensional, single-band models, the GBZ is usually a simple loop similar to the BZ (Fig. 23).

It has been conjectured in [44] that all GBZ for single-band models are connected. However, here we provide an example of a single-band GBZ with two connected components by explicitly constructing a model. We consider a PBC spectrum given by

$$\omega = \cos 2k + i \left(\frac{5}{2} \sin 3k - 3 \sin 2k \right) = -\frac{5}{4}z^{-3} + 2z^{-2} - z^2 + \frac{5}{4}z^3. \quad (101)$$

The PBC and OBC spectra are shown in Fig. 24(a), where the OBC spectrum features a teardrop-shaped section near $\omega = 1$, and the GBZ becomes disconnected [Fig. 24(b)]. This can be understood with the iso- $|z|$ contour self-intersection construction of the OBC spectrum [Fig. 24(c)]. The PBC spectrum features a small loop near $\text{Arg}(z) = 0$

Figure 24



GBZ for single-band models can be disconnected. (a) The PBC (black dashed) and OBC (red solid) spectrum of the model $\omega = -5z^{-3}/4 + 2z^{-2} - z^2 + 5z^3/4$. (b) The GBZ (blue) corresponding to (a). The inset shows an enlarged view of the disconnected part. (c) Iso- $|z|$ contour self-intersection construction of the OBC spectrum. As the $\text{Arg}(z) = \pi$ segment sweeps through the loop, the z solution belonging to the segment becomes disconnected from the rest.

to the left of $\omega = 1$ while being tangent to another vertical segment near $\text{Arg}(z) = \pi$ of the PBC curve. When the $\text{Arg}(z) = \pi$ segment sweeps through the loop to the left, the intersections become part of the OBC spectrum, and the corresponding z points are added to the GBZ. However, after the segment sweeps past the loop, the OBC spectrum continues along the self-intersection of the loop as the winding number changes. The section near $\text{Arg}(z) = \pi$ no longer creates OBC modes, and the GBZ section becomes disconnected from the rest.

As $\ln |z_{(p)}|$ represents the overall decay factor of the mode profile as argued in Section 5.1b, any GBZ points that are not on the BZ indicate the presence of the non-Hermitian skin effect, as discussed in Section 5.3. In addition, the GBZ also carries theoretical significance; for example, the Green function of an OBC chain [63–67] can be expressed as a contour integral along the GBZ [68,69].

5.3. Non-Hermitian Skin Effect

For the SIBC spectrum of a right-extending chain, the exponential decay requirement restricts $|z| \leq 1$, and we expect to find the modes with $|z| < 1$ in the regions enclosed by the PBC spectrum curve with positive winding numbers. For the OBC modes, however, there are no *a priori* requirements for exponential decay, and instead the $|z_{(p)}| = |z_{(p+1)}|$ condition provides a natural interpretation of the overall decay factor of the mode. If $|z_{(p)}| < 1$ ($|z_{(p)}| > 1$), then the mode will be localized at the left (right) edge in the $N \rightarrow \infty$ limit. By the continuity of the OBC spectrum, the modes with

a frequency close enough to a $|z_{(p)}| \neq 1$ mode will also feature $|z_{(p)}| \neq 1$, leading to a finite section of the OBC spectrum with boundary-localizing modes. Such an appearance of a macroscopic number of modes localized on one of the boundaries in the limit of $N \rightarrow \infty$ is known as the *non-Hermitian skin effect* and the corresponding modes are *skin modes*.

On the z plane, the non-Hermitian skin effect will occur if the GBZ is different from the $|z| = 1$ circle. The portions of GBZ inside $|z| = 1$ correspond to the modes piling up on the left edge, and the portions of GBZ outside $|z| = 1$ correspond to the modes piling up on the right edge. On the ω plane, the OBC spectrum consists of arcs without internal areas. If the PBC spectrum encloses finite areas with nonzero winding numbers, then the OBC spectrum is guaranteed to be different from the PBC spectrum, and skin modes will be present [44,52]. The modes localizing on the left boundary have $|z_{(p)}| = |z_{(p+1)}| < 1$, and their frequencies are located in the regions where the PBC spectrum has a positive winding number (as there are more than p solutions of z satisfying $|z| < 1$). Similarly, the modes localizing on the right boundary will be located in the negative winding number regions. As such, it is possible to have both left-localizing and right-localizing modes in the same system if the PBC spectrum features both positive and negative winding numbers [70] (e.g., Fig. 21 (a)).

We note that the non-Hermitian skin effect is not invariant under the gauge transformation, as it depends on the location of $|z| = 1$ to separate the left and right skin modes. It is straightforward to gauge transform a model without skin effects such that all modes in the new model pile up on the left edge, and similarly some specific models where the GBZ is given by $|z| = z_0$ (such as the Hatano–Nelson model with positive real coefficients, as discussed in Section 3.1b) can be gauge transformed to eliminate the skin effect.

Another note is that the profile of any OBC mode does not only depend on the value of $|z_{(p)}|$ but also on the $|z|$ values from other states in the superposition. The existence of $z_{(1)}$ to $z_{(p-1)}$ states may create additional exponential components at the left end of the chain, and the mode amplitude may appear to be concentrated on the left end for a short chain even if $|z_{(p)}| > 1$. As such, the piling direction of the mode is indicated by $|z_{(p)}|$ only for sufficiently long chains.

In the following, we discuss how certain symmetries of the model constrain the non-Hermitian skin effect.

5.3a. Hermiticity

Since the “non-Hermitian skin effect” contains the adjective “non-Hermitian,” we expect that the effect does not show up for Hermitian models, i.e., the GBZ of all Hermitian models should coincide with the BZ. Here Hermiticity requires the “to” and “from” coupling coefficients to be complex conjugates of each other:

$$t_m = t_{-m}^*. \quad (102)$$

In this case, $p = q$, and the PBC spectrum can be written as

$$\omega = t_0 + 2 \operatorname{Re} \left[\sum_{m=1}^q t_m z^m \right], \quad (103)$$

where we have used $z^{-1} = z^*$ on the BZ. As such, ω is always real, and the PBC spectrum is a line on the real axis. All other points not on the line segment have a winding number of 0.

For the OBC spectrum, we observe that the points not on the PBC spectrum could not be in the OBC spectrum as they have a winding number of 0 (as discussed in Section

5.2), and as such the OBC spectrum is entirely contained in the PBC spectrum. On the other hand, for real ω values, the $2p$ solutions of z possess a Hermitian symmetry: $(z^{-1})^*$ is a solution to the band structure if z is. As such, the magnitude of solutions come in pairs after being ordered, i.e., $|z_{(2p)}| = |z_{(1)}|^{-1}$, $|z_{(2p-1)}| = |z_{(2)}|^{-1}$, and so on. A ω point on the PBC indicates that at least one $|z_{(m)}|$ is 1; by the pairing argument, $|z_{(p)}|$ and $|z_{(p+1)}|$ must be 1. Therefore, every point in the PBC spectrum is in the OBC spectrum, and the GBZ coincides with $|z| = 1$ where no skin modes could be found. The notion of the “non-Hermitian skin effect” has thus been justified since this effect only occurs in non-Hermitian models.

5.3b. Reciprocity

Reciprocity is a fundamental symmetry of the Maxwell equations that governs the dynamics of electromagnetism [71]. In the context of band structures, it would require the “to” and “from” coupling coefficients to be equal to each other:

$$t_m = t_{-m}. \quad (104)$$

In this case, $p = q$, and the PBC spectrum can be written as

$$\omega = t_0 + \sum_{m=1}^q t_m (z^m + z^{-m}) = t_0 + 2 \sum_{m=1}^q t_m \cos k. \quad (105)$$

The spectrum may be complex but satisfies $\omega(k) = \omega(2\pi - k)$. As such, the PBC spectrum curve backtracks itself after $k = \pi$ and every point not on the curve has a winding number of 0. The reciprocity symmetry indicates that z^{-1} is a solution to the band structure if z is, with no restrictions on ω . Following the argument of the Hermitian case, the OBC spectrum coincides with the PBC spectrum and no skin modes will be found. We conclude that a model must break both Hermiticity and reciprocity for skin modes to manifest.

5.3c. Time-Reversal Symmetry

Time-reversal symmetry is another fundamental symmetry for electromagnetics that is separate from reciprocity. A natural way to define time-reversal symmetry in tight-binding models is to require that the coupling coefficients are real:

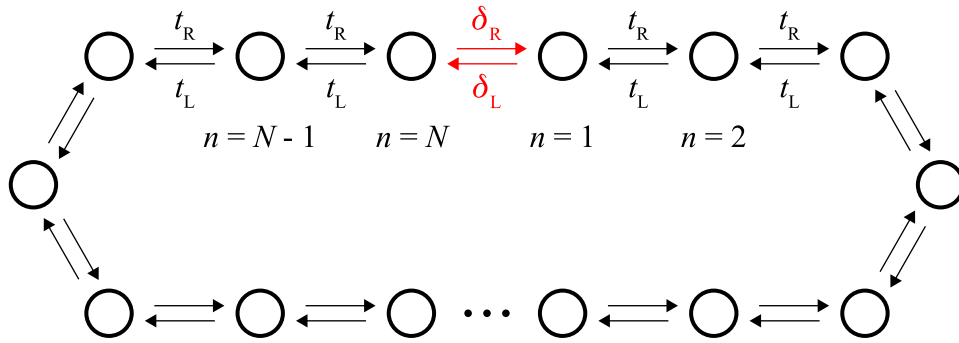
$$t_m = t_m^*. \quad (106)$$

Unfortunately, this symmetry alone does not imply any special properties of the OBC spectra other than conjugation symmetry, as demonstrated by the model $\omega = z^{-1} + z + 3z^2$ in Section 3.2. The different behavior of time-reversal symmetry compared with other symmetries can be understood using gauge transformations. An imaginary gauge transformation would break Hermiticity and reciprocity, but not time-reversal symmetry. If a specific model with time-reversal symmetry lacks the non-Hermitian skin effect, gauge transformation would make the new model acquire the non-Hermitian skin effect while preserving the time-reversal symmetry. It is possible to combine time-reversal symmetry with other symmetries to create composites. For example, reciprocity conditions are equivalent to Hermiticity under the assumption of time-reversal symmetry, and the discussions with Hermiticity and reciprocity would apply.

5.4. Spectral Dependence on Boundary Conditions

A unique aspect of the non-Hermitian system is the drastic difference between the OBC and the PBC spectra, even though the only structural difference between a PBC

Figure 25



Schematic of the generalized boundary conditions for the Hatano–Nelson model. Couplings are periodic except at the boundary between cell N and cell 1 , where δ_R replaces t_R and δ_L replaces t_L .

chain and an OBC chain with the same number of cells is the removal of hopping terms at the boundaries (Fig. 2). This is very different from Hermitian systems, where such a structural difference does not induce drastic spectral changes. In non-Hermitian systems, the extreme sensitivity to boundary conditions [72–74] is responsible for the drastic difference between the OBC and PBC spectra, and the sensitivity can be traced to the decay rate ($\ln |z|$) from the non-Hermitian skin effect. With the Hatano–Nelson model as an example, we demonstrate how the PBC spectrum morphs into the OBC spectrum as we vary the boundary conditions [57,73,75].

Consider a Hatano–Nelson chain with N cells and coupling coefficients t_L and t_R . We assume that $t_L > t_R > 0$ as we have shown in Section 3.1d that the most general cases can be reduced to this case via rotating the ω plane, rotating the z plane (i.e., shifting k by real numbers via real gauge transformations), and flipping the entire chain. However, instead of working with a fully periodic chain, we replace the coupling from cell N to cell 1 by δ_R and the coupling from cell 1 to cell N by δ_L (Fig. 25). This generalizes the boundary condition we have been using and includes both PBC and OBC as special cases: the PBC corresponds to $\delta_R = t_R$ and $\delta_L = t_L$, and the OBC corresponds to $\delta_R = \delta_L = 0$. The goal is to understand how the spectrum evolves when δ_R and δ_L are continuously tuned to zero, a procedure sometimes known as the PBC–OBC spectral flow [57].

We begin with an analytical description of the model [73] by constructing the boundary conditions explicitly. The dynamics of the first cell now reads

$$-i\omega\psi_1 = -it_L\psi_2 - i\delta_R\psi_N. \quad (107)$$

A general mode in the bulk can be expressed as $\psi_n = \alpha_{(1)}z_{(1)}^n + \alpha_{(2)}z_{(2)}^n$, where $z_{(1)}$ and $z_{(2)}$ are solutions to $\omega = t_R z^{-1} + t_L z$. To eliminate ω from Eq. (107) and arrange the boundary condition in a form comparable to the OBC, we fictitiously extend the lattice segment past the boundary to include the lattice site 0 , where ψ_0 is obtained from the bulk mode expression. We can then compare Eq. (107) with the dynamics of the first cell as if it is in the bulk,

$$-i\omega\psi_1 = -it_L\psi_2 - it_R\psi_0 \quad (108)$$

and write the boundary condition as

$$\delta_R\psi_N = t_R\psi_0, \quad (109)$$

where both state amplitudes are to be substituted by $\psi_n = \alpha_{(1)}z_{(1)}^n + \alpha_{(2)}z_{(2)}^n$. The boundary condition can be interpreted as “the incoming rate of amplitude change across the

boundary equals the corresponding rate in the bulk.” In terms of the z solutions, the condition reduces to

$$(\delta_R z_{(1)}^N - t_R)\alpha_{(1)} + (\delta_R z_{(2)}^N - t_R)\alpha_{(2)} = 0. \quad (110)$$

Similarly, for the last cell in the chain, the boundary condition reads

$$\delta_L \psi_1 = t_L \psi_{N+1} \quad (111)$$

and substituting in the general mode expression gives

$$(\delta_L z_{(1)} - t_L z_{(1)}^{N+1})\alpha_{(1)} + (\delta_L z_{(2)} - t_L z_{(2)}^{N+1})\alpha_{(2)} = 0. \quad (112)$$

These two conditions are linear equations in $\alpha_{(1)}$ and $\alpha_{(2)}$, and to get nonzero solutions, the coefficient determinant must vanish:

$$\begin{vmatrix} \delta_R z_{(1)}^N - t_R & \delta_R z_{(2)}^N - t_R \\ \delta_L z_{(1)} - t_L z_{(1)}^{N+1} & \delta_L z_{(2)} - t_L z_{(2)}^{N+1} \end{vmatrix} = 0. \quad (113)$$

To simplify this determinant, we can gauge transform the model such that the submatrix in the Hamiltonian that describes the bulk of the chain is Hermitian. We introduce the geometric mean coupling $t = \sqrt{t_L t_R}$ and the asymmetry factor $g = \ln(t_L/t_R)/2$. We scale the phase factor and define $Z = e^g z$ such that $\omega = t(Z + Z^{-1}) = 2t \cos K$ with $Z = \exp(iK)$. Expanding the determinant leads to

$$Z_{(1)}^{-1}(e^{-Ng} \delta_R Z_{(1)}^N - t_R)(e^{Ng} \delta_L - t_L Z_{(1)}^{-N}) - Z_{(1)}(e^{-Ng} \delta_R Z_{(1)}^{-N} - t_R)(e^{Ng} \delta_L - t_L Z_{(1)}^N) = 0, \quad (114)$$

where we have used that $Z_{(1)} Z_{(2)} = 1$. In terms of the complex K , the equation can also be rearranged as

$$\frac{\sin(N+1)K}{\sin K} - \frac{\delta_L \delta_R}{t_L t_R} \frac{\sin(N-1)K}{\sin K} - \left(e^{Ng} \frac{\delta_L}{t_L} + e^{-Ng} \frac{\delta_R}{t_R} \right) = 0 \quad (115)$$

and the distributions of solutions can be obtained by graphical methods.

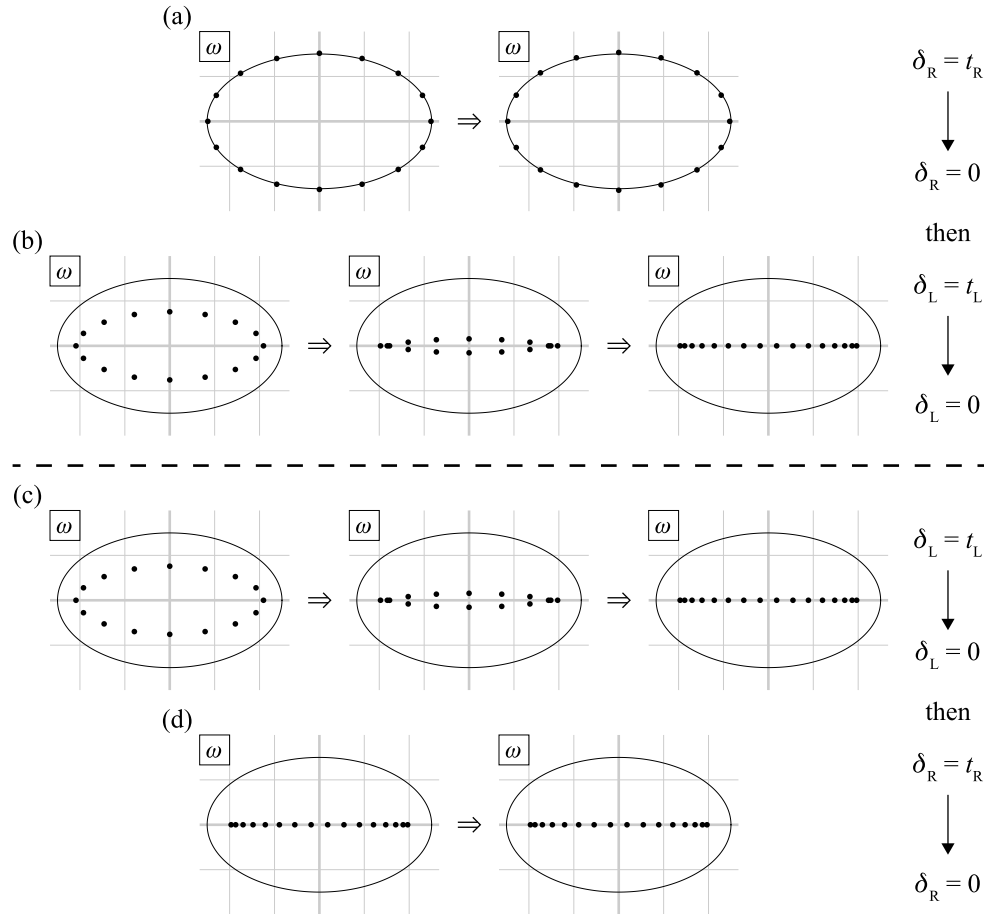
To evolve from PBC to OBC, we continuously decrease δ_R from t_R to 0 and then decrease δ_L from t_L to 0. Numerical evidence suggests that the spectrum did not change much during the $\delta_R \rightarrow 0$ step [Fig. 26(a)] but suddenly collapsed onto the real axis in the $\delta_L \rightarrow 0$ step [Fig. 26(b)]. This can be understood by considering the properties of the two states at ω .

For the PBC structure, we have $z_{(2)} = 1$ and $z_{(1)} = e^{-2g}$. The $z_{(1)}$ state does not satisfy PBC but may be present when the $z_{(2)}$ state is reflected at the boundary. After the $\delta_R \rightarrow 0$ step, the composition of $z_{(1)}$ state in ψ_1 is comparable to the $z_{(2)}$ state as the left boundary condition becomes $\psi_0 = 0$, but the composition of $z_{(1)}$ state in ψ_N is negligible as it has been attenuated by e^{-2Ng} . As such, we only need to tune $z_{(2)}$ slightly to match the other boundary condition. By substituting $\delta_L = t_L$, $\delta_R = 0$, and using $z_{(1)} = e^{-2g}/z_{(2)}$ in Eq. (113), we arrive at

$$z_{(2)}^2 - z_{(2)}^{N+2} \approx e^{-2g} \rightarrow z_{(2)} \approx \hat{z} \left[1 + \frac{1}{N} \ln(1 - e^{-2g} \hat{z}^{-2}) \right], \quad (116)$$

where $\hat{z} = \exp(2i\pi/N), \exp(4i\pi/N), \dots, \exp(2Ni\pi/N)$ are the PBC solutions. Both the $z_{(2)}$ and the corresponding ω are shifted on the $O(1/N)$ order. Therefore, the spectrum does not change significantly during the $t_R \rightarrow 0$ step. Another intuitive way to arrive at the same qualitative result is by observing that ψ tends to be transported to the left

Figure 26



Eigenvalue flows when continuously evolving from PBC to OBC in the Hatano–Nelson model. In all panels $N = 16$, $t_L = 2$, and $t_R = 1/2$. The black ellipsoid marks the corresponding PBC spectrum for comparison. In (a), δ_R decreases from t_R to 0 whereas $\delta_L = t_L$ remains unchanged. Parameters are $\delta_R = 1/4$ (left panel) and 0 (right panel). In (b), $\delta_R = 0$ remains unchanged whereas δ_L decreases from t_L to 0. Parameters are $\delta_L = 2^{-7}$ (left panel), 2^{-14} (middle panel), and 0 (right panel). In (c), δ_L decreases from t_L to 0 whereas $\delta_R = t_R$ remains unchanged. Parameters are $\delta_L = 2^{-7}$ (left panel), 2^{-14} (middle panel), and 0 (right panel). In (d), $\delta_L = 0$ remains unchanged whereas δ_R decreases from t_R to 0. Parameters are $\delta_R = 1/4$ (left panel) and 0 (right panel).

as $t_L > t_R$. By keeping $\delta_L = t_L$, the transport continues across the boundary, and the mode profile remains similar to the PBC case.

The following $\delta_L \rightarrow 0$ step behaves very differently. As the left boundary condition has also been modified, the composition of $z_{(1)}$ and $z_{(2)}$ states in ψ_N needs to be adjusted. However, since they are at exponentially different scales, the decaying rate of both states, determined by $|z_{(1)}|$ and $|z_{(2)}|$, will shift toward each other to decrease the scale difference and match the boundary condition. This can be described by gauge-transforming the model with $\delta_R = 0$, resulting in new coupling amplitudes $\Delta_L = T_L = t_L(\delta_L/t_L)^{1/N}$ and $T_R = t_R(\delta_L/t_L)^{-1/N}$. This eliminates the scaling difference between δ_L and t_L , and T_L and T_R approach each other. Since the system behaves similarly to the corresponding PBC spectrum when $\Delta_L = T_L$ and $T_L > T_R$ is maintained, $|z_{(1)}|$ and $|z_{(2)}|$ continue to approach each other and this is accompanied by the shrinking of the spectrum. This process continues until $\delta_L \sim e^{-N\delta} t_L$, after which point $|z_{(1)}|$ and $|z_{(2)}|$ are nearly equal and the OBC behavior becomes dominant.

If the order of parameter changes is reversed when approaching OBC from PBC, the spectral behavior will also be reversed [Figs. 26(c) and 26(d)]: the spectrum collapses onto the real line when δ_L is decreased to 0 first, followed by minimal spectrum changes when δ_R decreases to 0. This shows that the change of couplings with a direction opposite to the state decay has the greatest effect on the spectral flow.

Finally, to explicitly show the extreme spectral sensitivity on boundary conditions for OBC, we apply perturbation analysis on the OBC spectra and see how adding couplings changes the spectrum. It is more convenient to use the Toeplitz matrix form of the Hamiltonian,

$$H = \begin{bmatrix} 0 & t_L & & & & & \delta_R \\ t_R & 0 & t_L & & & & \\ & t_R & \ddots & \ddots & & & \\ & & \ddots & \ddots & t_L & & \\ & & & t_R & 0 & t_L & \\ \delta_L & & & & t_R & 0 & \end{bmatrix}. \quad (117)$$

The first-order perturbation of a nondegenerate eigenvalue can be written as

$$\delta\omega = \frac{\psi_{\text{left}}^T \delta H \psi_{\text{right}}}{\psi_{\text{left}}^T \psi_{\text{right}}}, \quad (118)$$

where ψ_{left} and ψ_{right} are the left and right eigenmodes for H , with $\psi_{\text{left}} H = \omega \psi_{\text{left}}$ and $H \psi_{\text{right}} = \omega \psi_{\text{right}}$. When $\delta_R = \delta_L = 0$ (OBC), the eigenvectors can be expressed as $\psi_{\text{right},n} = e^{-ng} \sin(nK)$ and $\psi_{\text{left},n} = e^{ng} \sin(nK)$ with $K = \pi/(N+1), 2\pi/(N+1), \dots, N\pi/(N+1)$. With $\delta_R = 0$ and a small nonzero δ_L with $|\delta_L| \ll e^{-Ng}$, the perturbation calculation reads

$$\delta\omega = \frac{2 \sin K \sin NK}{N+1} e^{(N-1)g} \delta_L \quad (119)$$

and the e^{Ng} factor demonstrates the extreme sensitivity. In the literature, such behavior as described in Eq. (119) has sometimes been referred to as the “exponential sensitivity on boundary conditions” [74]. However, we note that the exponential dependence refers to the size of the system rather than the perturbation.

6. MULTIBAND MODELS

In the previous sections, we have been considering single-band models. There are situations where a multiband model is more appropriate for describing the system in question, e.g., when the unit cell contains internal degrees of freedom. In these cases, each ψ_n in Eq. (1) becomes a vector and the Hamiltonian in the wave vector space is a matrix where each entry is a Laurent polynomial in z . This leads to two spectral features that are absent in the single-band models: the possible permutations of bands after going around the BZ, which are fully described by the braiding of eigenfrequencies [19,76–80], and the existence of edge modes that are distinct from skin modes. Both of these effects could not be fully represented by band winding alone, and are thus outside the scope of this tutorial. We briefly discuss their connections to the band winding and refer interested readers to some reviews on these related topics [36–38]. Instead, here we focus only on band winding and non-Hermitian skin effects in multiband models.

In the following, we mainly consider two-band systems; generalizations to more bands will be straightforward. Each ψ_n will be a two-component vector in the form of $(\psi_{A,n}, \psi_{B,n})^T$, with subscripts A and B labeling the components. For lattice models,

each unit cell is represented by two lattice sites, with the components of ψ_n assigned to each site. The dynamics of these components can be described by

$$\begin{aligned} \frac{d\psi_{A,n}}{d\tau} = & \cdots - it_{AA,-1}\psi_{A,n-1} - it_{AB,-1}\psi_{B,n-1} \\ & - it_{AA,0}\psi_{A,n} - it_{AB,0}\psi_{B,n} \\ & - it_{AA,+1}\psi_{A,n+1} - it_{AB,+1}\psi_{B,n+1} + \cdots, \end{aligned} \quad (120)$$

$$\begin{aligned} \frac{d\psi_{B,n}}{d\tau} = & \cdots - it_{BA,-1}\psi_{A,n-1} - it_{BB,-1}\psi_{B,n-1} \\ & - it_{BA,0}\psi_{A,n} - it_{BB,0}\psi_{B,n} \\ & - it_{BA,+1}\psi_{A,n+1} - it_{BB,+1}\psi_{B,n+1} + \cdots, \end{aligned} \quad (121)$$

where $t_{XY,m}$ denote the coupling coefficient from component X in the $(n+m)$ th cell to component Y in the n th cell. Written more compactly,

$$\frac{d}{d\tau} \begin{bmatrix} \psi_{A,n} \\ \psi_{B,n} \end{bmatrix} = -i \sum_m \begin{bmatrix} t_{AA,m} & t_{AB,m} \\ t_{BA,m} & t_{BB,m} \end{bmatrix} \begin{bmatrix} \psi_{A,n+m} \\ \psi_{B,n+m} \end{bmatrix}. \quad (122)$$

In analogy to the single-band case, we can write down the matrix form of the Hamiltonian for all components of all cells:

$$\frac{d}{d\tau} \begin{bmatrix} \vdots \\ \psi_{A,0} \\ \psi_{B,0} \\ \psi_{A,1} \\ \psi_{B,1} \\ \vdots \end{bmatrix} = -i \begin{bmatrix} \ddots & \vdots & \vdots & \vdots & \vdots & \vdots \\ \cdots & t_{AA,0} & t_{AB,0} & t_{AA,1} & t_{AB,1} & \cdots \\ \cdots & t_{BA,0} & t_{BB,0} & t_{BA,1} & t_{BB,1} & \cdots \\ \cdots & t_{AA,-1} & t_{AB,-1} & t_{AA,0} & t_{AB,0} & \cdots \\ \cdots & t_{BA,-1} & t_{BB,-1} & t_{BA,0} & t_{BB,0} & \cdots \\ \vdots & \vdots & \vdots & \vdots & \vdots & \ddots \end{bmatrix} \begin{bmatrix} \vdots \\ \psi_{A,0} \\ \psi_{B,0} \\ \psi_{A,1} \\ \psi_{B,1} \\ \vdots \end{bmatrix}. \quad (123)$$

This matrix has constant block entries for each descending diagonal, known as an *infinite block Toeplitz matrix*.

Using $\psi_n(\tau) = (\psi_{A,0}, \psi_{B,0})^T(\tau=0) \times \exp(ikn) \times \exp(-i\omega\tau)$ and assuming tight-binding models, we obtain the following:

$$\omega \begin{bmatrix} \psi_{A,n} \\ \psi_{B,n} \end{bmatrix} = \sum_{-p \leq m \leq q} \begin{bmatrix} t_{AA,m}z^m & t_{AB,m}z^m \\ t_{BA,m}z^m & t_{BB,m}z^m \end{bmatrix} \begin{bmatrix} \psi_{A,n} \\ \psi_{B,n} \end{bmatrix}. \quad (124)$$

The matrix appearing on the right-hand side of the previous equation is the (wave-vector-space) Hamiltonian:

$$H(z) = \sum_{-p \leq m \leq q} \begin{bmatrix} t_{AA,m}z^m & t_{AB,m}z^m \\ t_{BA,m}z^m & t_{BB,m}z^m \end{bmatrix}. \quad (125)$$

Each entry of $H(z)$ is a Laurent polynomial in z , and ω is the eigenvalue of $H(z)$ with $(\psi_{A,n}, \psi_{B,n})^T$ as its eigenvectors. As such, ω can be solved from the characteristic equation for $H(z)$:

$$\det[H(z) - \omega\mathbb{I}] = 0, \quad (126)$$

where \mathbb{I} is the identity matrix with dimensions matching $H(z)$. The above equation can be expanded as a polynomial in ω and defines the *band structure* for multiband systems.

Table 2. Spectral and Modal Features of Hermitian and Non-Hermitian Multiband One-Dimensional Models^a

| | Hermitian Models | Non-Hermitian Models | Related Concepts |
|-----------------|---|--|---|
| PBC spectra | $\omega \in \mathbb{R}$, line segments | $\omega \in \mathbb{C}$, multiple loops | Braiding (Section 6.3) |
| PBC modes | $k \in \mathbb{R}$, $ z = 1$ | $k \in \mathbb{R}$, $ z = 1$ | — |
| SIBC spectra | $\omega \in \mathbb{R}$, line segments (bulk modes) and isolated points (edge modes) | $\omega \in \mathbb{C}$, regions (bulk modes) and isolated points (edge modes) | Winding number (Section 6.3) |
| SIBC bulk modes | $k \in \mathbb{R}$, $ z = 1$ | $k_i \geq 0$, $ z \leq 1$ (right-extending chains) | — |
| SIBC edge modes | $k_i \geq 0$, $ z \leq 1$ (right-extending chains) | $k_i \geq 0$, $ z \leq 1$ (right-extending chains) | Band-structure-preserving transformations (Section 6.3) |
| OBC spectra | $\omega \in \mathbb{R}$, line segments (bulk modes) and isolated points (edge modes) | $\omega \in \mathbb{C}$, curve segments (bulk modes) and isolated points (edge modes) | — |
| OBC bulk modes | $k \in \mathbb{R}$, $ z = 1$ | No restrictions | — |
| OBC edge modes | No restrictions | No restrictions | — |

^aRelated concepts specific to the multiband case have also been listed.

6.1. Overview of Multiband One-Dimensional Models

An overview of the spectral characteristics of multiband models is provided in Table 2. Most of the spectral features of multiband models follow from their single-band counterparts, except that the PBC and OBC spectra may contain multiple connected components. Bulk mode profiles are also similar to the single-band case, where wave vectors are real for Hermitian models but can become complex for non-Hermitian models with nonperiodic boundary conditions. However, edge modes are unique to multiband models and may appear at the terminated boundaries in SIBC and OBC. These modes show up as isolated points on the complex ω plane and can have complex wave vectors even in the Hermitian case. As the behaviors of edge modes are similar in both Hermitian and non-Hermitian models, using complex wave vectors provides a unified treatment for both cases. Specific examples are demonstrated in Section 6.2 and some of the differences between multiband and single-band models are explored in Section 6.3. After that, a general discussion on the SIBC and OBC spectra can be found in Sections 6.4 and 6.5, respectively.

6.2. Example: the SSH Model

6.2a. Hermitian SSH Model

The SSH model [42] [Fig. 27(a)] is among the simplest one-dimensional multiband models that include edge modes in the SIBC and OBC spectrum, and its non-Hermitian extensions have been studied extensively in the context of establishing a non-Hermitian bulk–boundary correspondence for edge modes [12,14,16,17,81]. The model features alternating coupling strengths t_1 and t_2 in a one-dimensional chain. After grouping a neighboring pair of lattice sites into a single unit cell, one of the couplings becomes an intracell coupling between the two lattice sites while the other becomes an intercell coupling between neighboring unit cells [Fig. 27(b)].

The Hamiltonian $H(z)$ of the SSH model is given by

$$H(z) = \begin{bmatrix} 0 & t_1 + t_2 z^{-1} \\ t_1 + t_2 z & 0 \end{bmatrix}, \quad (127)$$

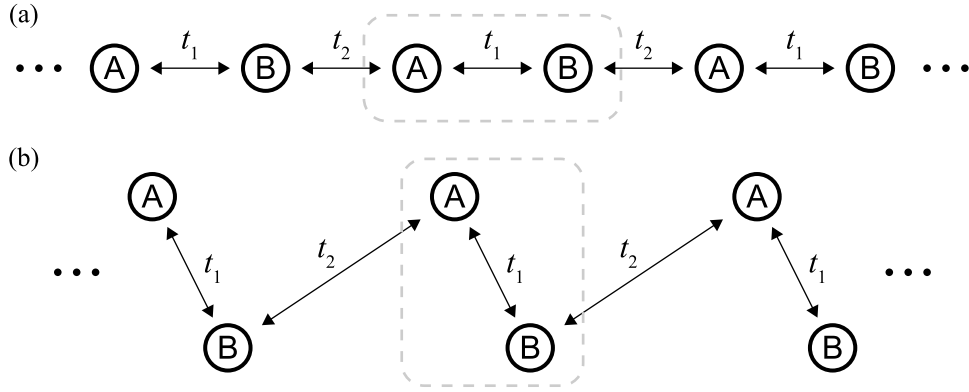
where t_1 and t_2 are both positive.

The PBC spectrum can be solved from the characteristic equation:

$$\omega^2 - (t_1 + t_2 z^{-1})(t_1 + t_2 z) = 0, \quad (128)$$

$$\omega = \pm \sqrt{t_1^2 + t_2^2 + 2t_1 t_2 \cos k}. \quad (129)$$

Figure 27



Schematic of the SSH model. (a) Representation of the model emphasizing the alternating couplings in a one-dimensional chain. (b) Representation of the model emphasizing the intracell and intercell couplings with two lattice sites per unit cell. Letters A and B indicate the corresponding component for each site.

The band structure has a gap at $k = \pi$ with $\omega = \pm|t_1 - t_2|$, and no modes can be found in the interval from $-|t_1 - t_2|$ to $|t_1 - t_2|$ [Figs. 28(a) and 28(b)]. The gap closes when $t_1 = t_2$.

For the SIBC spectra, the mode is in general of the form

$$\psi_n = \alpha_{(1)} \begin{bmatrix} t_1 + t_2 z_{(1)}^{-1} \\ \omega \end{bmatrix} z_{(1)}^n + \alpha_{(2)} \begin{bmatrix} t_1 + t_2 z_{(2)}^{-1} \\ \omega \end{bmatrix} z_{(2)}^n, \quad (130)$$

where the general form of eigenvectors for $H(z)$ have been substituted directly. We note that the two states are not the two eigenvectors for a single $H(z)$, but one eigenvector from $H(z_{(1)})$ and one eigenvector from $H(z_{(2)})$ which share the same ω . The left boundary removes the coupling between $\psi_{A,1}$ and $\psi_{B,0}$ (Fig. 27), which imposes the condition $\psi_{B,0} = 0$. This leads to

$$\omega(\alpha_{(1)} + \alpha_{(2)}) = 0 \quad (131)$$

and we need to discuss two cases based on Eq. (131).

If $\omega \neq 0$, then $\alpha_{(1)} = -\alpha_{(2)}$, and the existence of both components requires that $|z_{(1)}| \leq 1$ and $|z_{(2)}| \leq 1$. Together with Vieta's formula applied to the band structure ($z_{(1)}z_{(2)} = 1$), we get $|z_{(1)}| = |z_{(2)}| = 1$, i.e., the modes are superpositions of the corresponding PBC modes.

For the other case $\omega = 0$, the z can be solved directly from Eq. (128) as $-t_1/t_2$ and $-t_2/t_1$. The form of eigenvectors appearing in Eq. (130) cannot be used to determine the eigenvector at $z = -t_2/t_1$ as substituting this into $(t_1 + t_2 z^{-1}, \omega)^T$ produces $(0, 0)^T$. Instead, we can write down the Hamiltonian at these two z points as

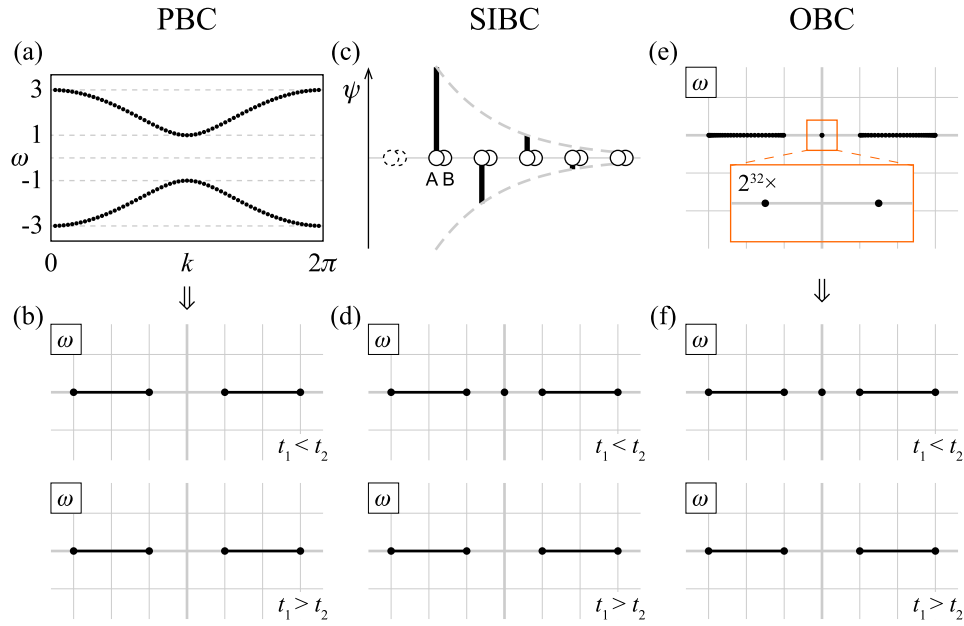
$$H\left(z = -\frac{t_1}{t_2}\right) = \begin{bmatrix} 0 & (t_1^2 - t_2^2)/t_1 \\ 0 & 0 \end{bmatrix}, \quad H\left(z = -\frac{t_2}{t_1}\right) = \begin{bmatrix} 0 & 0 \\ (t_1^2 - t_2^2)/t_1 & 0 \end{bmatrix}. \quad (132)$$

Their eigenvectors at $\omega = 0$ can be found as $(1, 0)^T$ and $(0, 1)^T$, respectively. The superposition of these states becomes

$$\psi_n = \alpha_{(1)} \begin{bmatrix} 1 \\ 0 \end{bmatrix} \left(-\frac{t_1}{t_2}\right)^n + \alpha_{(2)} \begin{bmatrix} 0 \\ 1 \end{bmatrix} \left(-\frac{t_2}{t_1}\right)^n. \quad (133)$$

Imposing the $\psi_{B,0} = 0$ leads to $\alpha_{(2)} = 0$, eliminating one of the components, and the exponential decay requirement becomes $t_2 \geq t_1$. Therefore, one extra mode can be

Figure 28



Spectra of the Hermitian SSH model. (a) The PBC spectrum for $N = 64$ plotted as real ω versus real k , resembling band diagrams found in solid-state physics. Here $t_1 = 1$, $t_2 = 2$. (b) The PBC spectrum for $N \rightarrow \infty$ is plotted in the complex ω plane, with $t_1 = 1$, $t_2 = 2$ (top panel) and $t_1 = 2$, $t_2 = 1$ (bottom panel). (c) Mode profile of an edge mode. Note that the amplitudes are 0 on one of the components. Here $t_1 = 1$, $t_2 = 2$. (d) The SIBC spectrum is plotted in the complex ω plane, with $t_1 = 1$, $t_2 = 2$ (top panel) and $t_1 = 2$, $t_2 = 1$ (bottom panel). (e) The OBC spectrum for $N = 32$ (with a total of 64 sites) is plotted in the complex ω plane. Note the central splitting caused by edge mode couplings that is exponentially small. Here $t_1 = 1$, $t_2 = 2$. (f) The OBC spectrum for $N \rightarrow \infty$ is plotted in the complex ω plane, with $t_1 = 1$, $t_2 = 2$ (top panel) and $t_1 = 2$, $t_2 = 1$ (bottom panel).

found at $\omega = 0$ if $t_2 \geq t_1$, and for $t_2 > t_1$ this mode is special in the sense that the mode frequency is not part of the PBC spectra and the mode profile is not from the superposition of PBC modes with $\omega = 0$ [Figs. 28(c) and 28(d)]. Rather, this mode arises due to the existence of boundary conditions and is an *edge mode* of the system. No such modes can be found if $t_2 < t_1$.

The OBC spectra can be solved similarly to the SIBC spectra. The general mode has the same form as in the SIBC case, and it can be verified that $\omega = 0$ is not an exact solution to the OBC spectrum for any finite N . There are no exponential decay requirements, and we impose two boundary conditions, $\psi_{B,0} = 0$ and $\psi_{A,N+1} = 0$:

$$\alpha_{(1)} + \alpha_{(2)} = 0, \quad (134)$$

$$\alpha_{(1)}(t_1 + t_2 z_{(1)}^{-1})z_{(1)}^{N+1} + \alpha_{(2)}(t_1 + t_2 z_{(2)}^{-1})z_{(2)}^{N+1} = 0. \quad (135)$$

Eliminating $\alpha_{(1)}$ and $\alpha_{(2)}$ from the equation and using $z_{(1)}z_{(2)} = 1$ leads to

$$z_{(1)}^{N+1} - z_{(1)}^{-(N+1)} = -\frac{t_2}{t_1} \left(z_{(1)}^N - z_{(1)}^{-N} \right). \quad (136)$$

The equation has $2N + 2$ solutions, but two solutions $z_{(1)} = \pm 1$ lead to modes with identically zero amplitudes everywhere and should be excluded. The number of physical solutions agrees with the total number of sites and the modes are complete. To see

the distribution of these solutions, we substitute $z_{(1)} = e^{ik}$ and write the equation as

$$\sin(N+1)k = -\frac{t_2}{t_1} \sin Nk. \quad (137)$$

Graphical methods shows that there are $2N$ real solutions of k between 0 and 2π (excluding $k = 0$ and $k = \pi$) if $t_2/t_1 \leq (N+1)/N$, and only $2N-2$ real solutions if $t_2/t_1 > (N+1)/N$. In the latter case, there are two complex k solutions in the strip $0 \leq k < 2\pi$ corresponding to the two edge modes. Their corresponding ω is not exactly 0 as these two eigenmodes can be viewed as symmetric and antisymmetric superpositions of the two edge modes, which are localized on one edge for the SIBC but couple together through the bulk for the OBC. This coupling of edge modes induces a frequency splitting on the order of $(t_1/t_2)^N$ (Fig. 28(e)), and can be derived using transfer matrix methods [82]. After taking the $N \rightarrow \infty$ limit, the continuous part of the OBC spectrum approaches the PBC spectrum, and the frequencies of edge modes (if they exist) approach 0 (Fig. 28(f)).

In summary, we observe that in the Hermitian case, the PBC, SIBC, and OBC spectra are all similar. This observation is true for both single-band (see Section 3.1a) and multiband Hermitian models. For multiband Hermitian models, there may be additional edge modes that appear exclusively in the SIBC and OBC spectra with no counterpart in the PBC spectrum. Such edge modes do not occur in single-band Hermitian models.

6.2b. Non-Hermitian SSH Model

There are several non-Hermitian extensions of the SSH models where existing couplings are replaced with non-Hermitian ones or new non-Hermitian couplings are introduced. One example is to replace the intracell coupling with different coupling amplitudes going in each direction [20,27,50,83]. The Hamiltonian is given by

$$H(z) = \begin{bmatrix} 0 & t_1 e^g + t_2 z^{-1} \\ t_1 e^{-g} + t_2 z & 0 \end{bmatrix}, \quad (138)$$

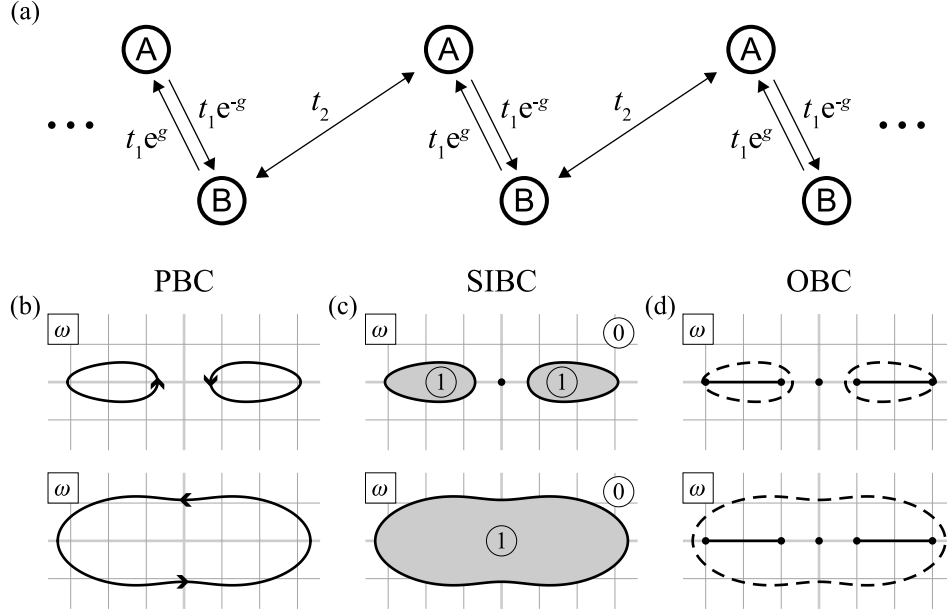
where t_1 and t_2 are positive and the asymmetry factor g is taken to be real [Fig. 29(a)]. This particular model is chosen as it can be gauge transformed into the Hermitian SSH model [27], which allows direct comparison of their OBC spectra.

The PBC spectrum can take complex values and is no longer restricted to the real ω axis compared to the Hermitian SSH model. The spectrum may consist of either two disjoint loops or one single loop, depending on whether $|g| < |\ln(t_2/t_1)|$ or not [Fig. 29(b)]. The $|g| > |\ln(t_2/t_1)|$ case provides an example where the PBC spectrum consists of fewer connected components than the number of bands; after going from $k = 0$ to $k = 2\pi$, some bands do not return to their starting frequencies but continue to another band. This feature corresponds to band braiding as discussed in [19,77]. It is unique to non-Hermitian models, as ω must be real in Hermitian models, and the bandgaps would segment the real axis and prevent the bands from switching places.

The SIBC spectrum has two possible contributions: the areas bounded by the PBC spectrum with positive winding numbers as well as the edge modes located at $\omega = 0$ [Fig. 29(c)]. We note that in the cases where the PBC spectrum consists of a single component and encloses $\omega = 0$, the edge mode argument does not provide an extra mode as it has already been accounted for when $|z_{(1)}| \leq 1$ and $|z_{(2)}| \leq 1$ simultaneously.

For the OBC spectrum, we explicitly construct the gauge transformations such that the non-Hermitian model is transformed into the Hermitian SSH model. We first scale

Figure 29



Non-Hermitian extension of the SSH model. (a) Schematic of the model. (b) The PBC spectrum, with $t_1 = 1$, $t_2 = 2$, and $g = 1/2$ (top panel) or $g = 1$ (bottom panel). (c) The corresponding SIBC spectrum from (b). Note that there is no additional edge modes in the bottom panel. (d) The corresponding OBC spectrum from (b).

the second component of the wave function by e^g by defining $\Psi = (\psi_A, e^g \psi_B)^T$. The effective Hamiltonian for Ψ can be found as

$$\begin{bmatrix} 1 & 0 \\ 0 & e^g \end{bmatrix} \begin{bmatrix} 0 & t_1 e^g + t_2 z^{-1} \\ t_1 e^{-g} + t_2 z & 0 \end{bmatrix} \begin{bmatrix} 1 & 0 \\ 0 & e^{-g} \end{bmatrix} = \begin{bmatrix} 0 & t_1 + t_2 e^{-g} z^{-1} \\ t_1 + t_2 e^g z & 0 \end{bmatrix}, \quad (139)$$

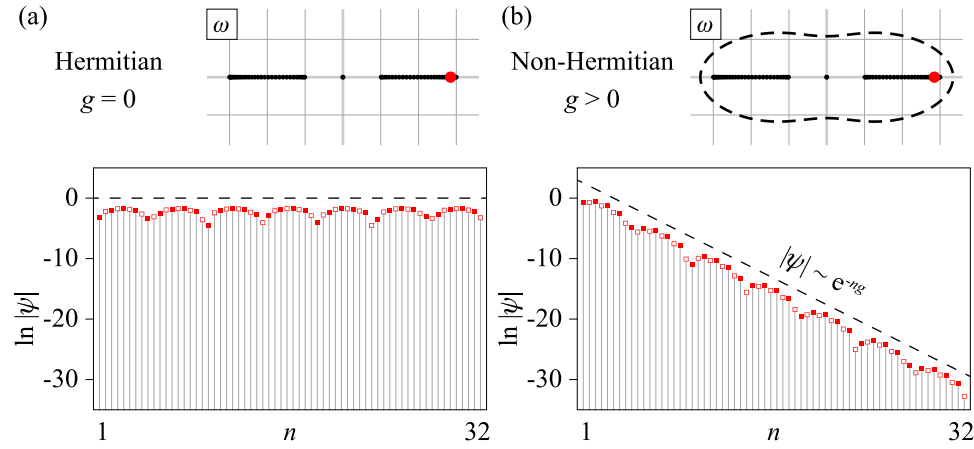
which then reduces to the Hermitian SSH model by another gauge transformation $Z = e^g z$. These transformations do not change the boundary conditions, and the model shares the same OBC spectrum with its Hermitian version, including the existence and location of the edge modes [Fig. 29(d)]. The gauge transformation $Z = e^g z$ implies the presence of the non-Hermitian skin effect, where the OBC mode profile scales with e^{-ng} . A comparison of the mode profile with the corresponding Hermitian case can be found in Fig. 30.

6.3. Winding Number, Braiding, and Edge Modes

Building upon the specific example discussed previously, we now consider general cases. The general analysis of SIBC spectra for multiband systems follows a similar argument to the single-band case: the modes are linear combinations of states with different z at the same ω while also satisfying $|z| \leq 1$ (on a right-extending chain), and the total number of such states are related to the winding number defined on the PBC bands. However, the multiband nature of the model introduces some subtleties in the derivation, which relates to band braiding and edge mode behaviors.

We now describe the details using a general two-band system where the Hamiltonian is in the form of Eq. (125). Expanding the characteristic equation results in a $(P + Q)$ th order equation in z where $-P$ and Q are the lowest and highest exponent of z appearing in the characteristic equation, respectively. Thus, there are $P + Q$ solutions of z for a specific ω . As the exponents for z in each matrix element are between $-p$ and q , P is at most $2p$ and Q is at most $2q$ (rp and rq for r bands). The reason that P and Q

Figure 30



Comparison of OBC mode profiles for the Hermitian and non-Hermitian SSH models. Here $t_1 = 1$, $t_2 = 2$. (a) Top panel: OBC spectrum (dots) for the Hermitian model ($g = 0$) with $N = 32$. The frequency $\omega \approx 2.848$ has been marked with a red dot. Bottom panel: Normalized OBC mode profile for A sites (solid squares) and B sites (empty squares) at $\omega \approx 2.848$. (b) Top panel: OBC spectrum (dots) and PBC spectrum (dashed curve) for the non-Hermitian model with $g = 1$ and $N = 32$. The frequency $\omega \approx 2.848$ has been marked with a red dot. Bottom panel: Normalized OBC mode profile for A sites (solid squares) and B sites (empty squares) at $\omega \approx 2.848$. The dashed line indicates the scaling of $|\psi|$ with n .

may be smaller than their upper bounds is that the z^{-2p} and z^{2q} terms may be missing with specific coupling coefficients. A concrete example would be the SSH models above (Section 6.2), where only two z solutions can be found ($P = Q = 1$) despite $2p = 2q = 2$.

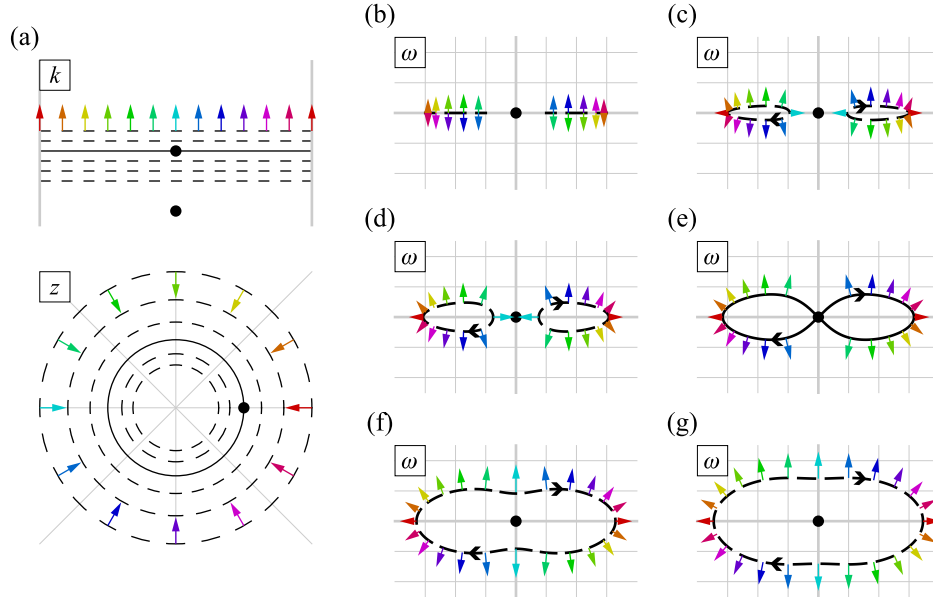
To count how many states satisfy the exponential decay requirement ($|z| \leq 1$) and are available for linear superposition, we sweep the shifted BZ to $k_i \rightarrow \infty$ and count the number of times the iso- $|z|$ contour goes through ω . For multiband models, the PBC spectrum may have multiple components (for the Hermitian SSH model there are two, agreeing with the conventional band definition), and these components may merge or split during the sweeping process (Fig. 31). Each component may pass through a given point ω individually, providing a new solution with $|z| \leq 1$, and it does not matter which component is the one passing through ω . Therefore, it makes sense to define the winding number w for the entire PBC spectra as the sum of the winding numbers of each component, i.e.,

$$w = \sum_m \frac{1}{2\pi i} \oint_{|z|=1} \frac{\omega'_m}{\omega_m - \omega_0} dz, \quad (140)$$

where ω_m is the m th component from the band structure that varies continuously from $k_r = 0$ to $k_r = 2\pi$. This definition also takes the band-merging scenario into account; in Figs. 31(f) and 31(g), ω_1 continues to ω_2 at the end of the BZ [i.e., $\omega_1(k_r \rightarrow 2\pi) = \omega_2(k_r \rightarrow 0)$] and vice versa, and their contributions are added together to form the winding number of the entire loop.

Although the geometrical interpretation of winding number w requires drawing the bands on the ω plane and joining them to form larger loops if necessary, the integral definition of w does not require knowledge of individual ω_m . We first review the following property for the addition of winding numbers: if $f_1(z)$ and $f_2(z)$ are two

Figure 31



Sweeping of the shifted BZ for the Hermitian SSH model with $t_1 = 1$, $t_2 = 2$. (a) The z solutions for $\omega = 0$ from the band structure are shown as dots on the k plane (upper panel) and on the z plane (lower panel; the solution outside $|z| = 1$ has been omitted). The six iso- k_i contours from bottom to top and the six iso- $|z|$ contours from outside to inside correspond to (b)–(g) in that order. Contours intersecting with k and z solutions are solid and other contours are dashed. Colored arrows are placed at equidistant k_r values and point toward larger k_i (smaller $|z|$). (b)–(g) Iso- $|z|$ contours of the band structure on the ω plane. The black dot represents $\omega = 0$. The direction of the contour indicates the direction with increasing k_r [$\text{Arg}(z)$]. Colored arrows correspond to (a) and show the sweeping direction of the contour as k_i increases. Parameters are: (b) $|z| = 1$; (c) $|z| = 0.794$; (d) $|z| = 0.630$; (e) $|z| = 0.5$; (f) $|z| = 0.397$; and (g) $|z| = 0.315$.

continuous complex functions that are nonzero everywhere on $|z| = 1$, $w[f_1(z)]$ and $w[f_2(z)]$ are the winding numbers of $f_1(|z| = 1)$ and $f_2(|z| = 1)$ with respect to 0, then

$$w[f_1(z)] + w[f_2(z)] = w[f_1(z)f_2(z)], \quad (141)$$

where the quantity on the right is the winding number for the product $f_1(z) \times f_2(z)$ as a function of z . This could be most easily understood by considering the subtended angle for each loop segment, where the argument of the product function is a sum of the individual arguments. For band structures, where each $\omega_m - \omega_0$ is an eigenvalue of $H(z) - \omega_0 \mathbb{I}$, the product of all band frequencies is simply $\det[H(z) - \omega_0 \mathbb{I}]$. As such, the winding number can also be calculated as, for any finite number of bands,

$$w = \frac{1}{2\pi i} \oint_{|z|=1} \frac{\det[H(z) - \omega_0 \mathbb{I}]'}{\det[H(z) - \omega_0 \mathbb{I}]} dz = \frac{1}{2\pi i} \oint_{|z|=1} dz \frac{d}{dz} \ln \det[H(z) - \omega_0 \mathbb{I}] \quad (142)$$

and no solutions for the individual bands are needed.

Following the same argument from the single-band case (Section 4.2), the number of $|z| \leq 1$ solutions is the difference between w and the winding number of a scaled model. As $\det[H(z) - \omega_0 \mathbb{I}]$ equals the value of characteristic polynomial with $\omega = \omega_0$, the scaled model is dominated by the z^{-P} term, which is, by definition, the term with

the lowest order for z . We conclude that

$$(\text{number of solutions with } |z| \leq 1) = w + P, \quad (143)$$

where P replaces p from the single-band case.

We note that a significant amount of information is lost in the process of reducing the PBC band structure to a single winding number for each ω . In particular, the winding behavior does not contain all information about the band braiding. Two models with the same shape of PBC spectrum may lead to the same winding number everywhere on the ω plane, but they may be drastically different in the sense that one model cannot be continuously changed to the other without inducing some form of degeneracy. Consider a two-band system where two Hatano–Nelson chains are placed next to each other:

$$H_1(z) = \begin{bmatrix} z & 0 \\ 0 & c + z \end{bmatrix}, \quad (144)$$

where one of the chains has a real on-site potential c . When $c = 1$, the PBC spectrum consists of two intersecting circles centered on $\omega = 0$ and $\omega = 1$, and has a winding number of 2 with respect to a reference point within the intersection region [Fig. 32(a)]. For this system, increasing c shifts the right circle to the right and eventually removes the intersection region. This process does not require the creation of any degeneracy, i.e., $H_1(z)$ remains nondegenerate for all $c > 1$. We contrast this behavior with another model, where the coupling phase for the first chain is flipped:

$$H_2(z) = \begin{bmatrix} -z & 0 \\ 0 & c + z \end{bmatrix}. \quad (145)$$

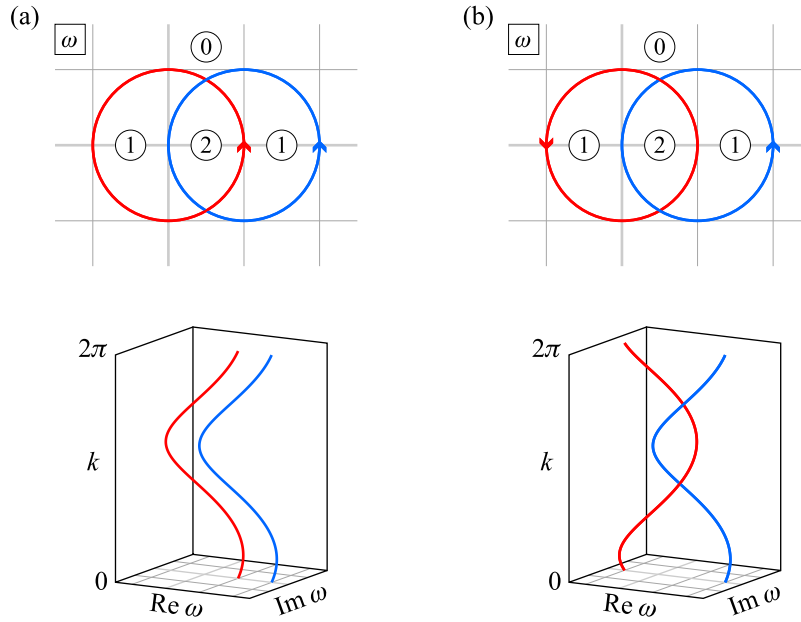
At any given c , the PBC spectra of $H_1(z)$ and $H_2(z)$ have the same shape. However, one can no longer remove the $w = 2$ region without inducing a degeneracy. As an example, one can again remove the $w = 2$ region by increasing the value of c from $c = 1$. However, the Hamiltonian $H_2(z)$ has a degeneracy point on the BZ at $z = -1$ when $c = 2$. The essential difference is that the two frequency strands for the Hamiltonian H_2 are *braided*, circling around each other as k increases from 0 to 2π . In contrast, no braiding occurs for H_1 , and the winding number calculation alone does not differentiate between H_1 and H_2 . Further discussions of band braiding are outside the scope of the tutorial, but they have been applied to the homotopy classification of non-Hermitian bands [76,78,79] and demonstrated experimentally [84–91].

The winding number property of a Hamiltonian is also unrelated to the edge mode properties. The band winding behavior is only determined by $\det[H(z) - \omega_0 \mathbb{I}]$; for the same winding behavior, there are still degrees of freedom to choose the matrix elements of $H(z)$. The Hermitian SSH model provides such an example, and its Hamiltonian is copied here for convenience:

$$H(z) = \begin{bmatrix} 0 & t_1 + t_2 z^{-1} \\ t_1 + t_2 z & 0 \end{bmatrix}. \quad (146)$$

We have shown in Section 6.2a that edge modes can be found when $t_2 > t_1$ and there are no edge modes when $t_2 < t_1$. However, the characteristic polynomial, $\omega^2 - (t_1 z + t_2)(t_1 + t_2 z)/z = 0$, is symmetric in t_1 and t_2 . Exchanging t_1 and t_2 in $H(z)$ preserves the characteristic polynomial and the PBC spectrum but adds or removes the edge modes. This can also be interpreted as a change of basis applied to the Hamiltonian. We define

Figure 32



Braiding in multiband models, which are not captured by the winding number. (a) Top panel: PBC spectrum of the model $[z, 0; 0, 1 + z]$ on the ω plane. Winding numbers have been marked. Bottom panel: A three-dimensional view of the same spectrum, where the two bands are not braided. (b) Top panel: PBC spectrum of the model $[-z, 0; 0, 1 + z]$ on the ω plane. Winding numbers have been marked. Bottom panel: A three-dimensional view of the same spectrum, where the two bands are braided.

a shift matrix:

$$U(z) = \begin{bmatrix} 0 & 1 \\ z & 0 \end{bmatrix}. \quad (147)$$

Performing a similarity transformation of H using U results in

$$U^{-1}HU = \begin{bmatrix} 0 & t_1 z^{-1} + t_2 \\ t_1 z + t_2 & 0 \end{bmatrix}, \quad (148)$$

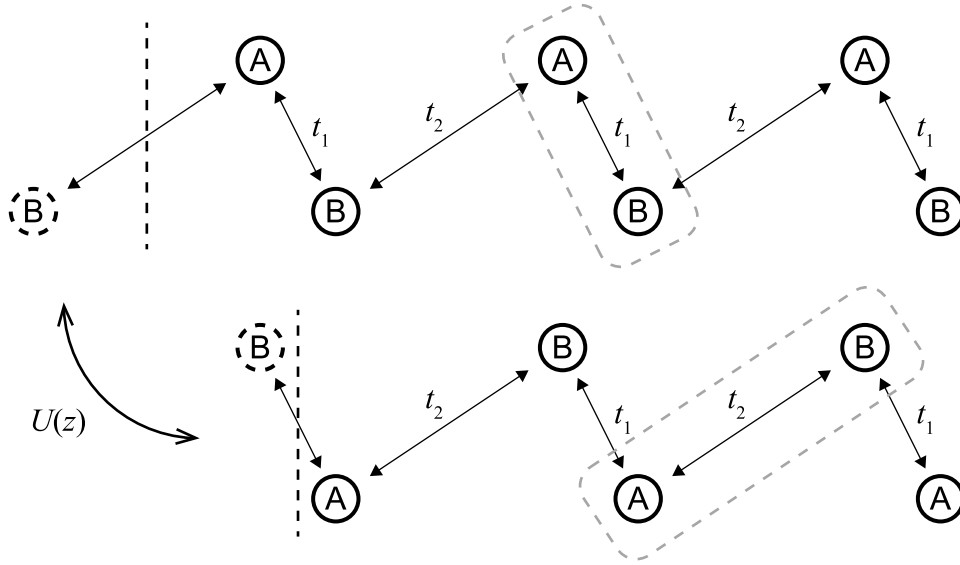
therefore exchanging the role of t_1 and t_2 . The action of U on the wave function replaces $\psi_{A,n}$ with $\psi_{B,n}$ and $\psi_{B,n}$ with $\psi_{A,n+1}$, effectively shifting the unit cell one lattice site to the right (hence, the name “shift matrix”; Fig. 33). For PBC spectra, this reinterpretation of unit cells does not change the physical structure of the chain, preserving the spectra and the winding numbers. The presence or absence of edge modes, on the other hand, depends on where the chain is terminated. In general, we can consider a matrix U with Laurent polynomial entries that also has a determinant in the form of z^s . This ensures that U^{-1} has Laurent polynomial entries. Consequently, $U^{-1}HU$ and H will both be tight-binding and share the same PBC spectrum and winding numbers, but the edge mode behaviors could be different. We discuss the conditions for the existence of edge modes in detail in the following.

6.4. Semi-Infinite Boundary Conditions

After establishing that there are $P + w$ states available for linear combinations, a general two-band SIBC mode can be expressed as

$$\psi_n = \sum_{m=1}^{P+w} \alpha_{(m)} \begin{bmatrix} a_{(m)} \\ b_{(m)} \end{bmatrix} z_{(m)}^n, \quad (149)$$

Figure 33



Unit cell relabeling in multiband models changes the presence of edge modes, which are not captured by the winding number. Dashed lines show the position of the boundary if SIBC is imposed in each case.

where $(a_{(m)}, b_{(m)})^T$ is the eigenvector of $H(z_{(m)})$ for the eigenvalue ω with arbitrary normalization.

The next step is to impose the boundary conditions. At first glance, we would require each component in ψ_m to be 0 with m from $-p + 1$ to 0, resulting in $2p$ equations, but this is not necessarily the case. Consider again the SSH model, where only one bond is disconnected at the boundary, and $\psi_{B,0} = 0$ is sufficient to maintain the boundary condition. This suggests that specific coupling coefficients can reduce the number of equations needed, similar to how P , the lowest order of z in the characteristic equation, can be less than $2p$.

The number and forms of boundary conditions are not entirely obvious from the coupling coefficients alone. As an example, we can perform gauge transformations on the non-Hermitian SSH model discussed above to arrive at a new Hamiltonian:

$$\frac{1}{2} \begin{bmatrix} 1 & -i \\ -i & 1 \end{bmatrix} \begin{bmatrix} 0 & t_1 e^g + t_2 z^{-1} \\ t_1 e^{-g} + t_2 z & 0 \end{bmatrix} \begin{bmatrix} 1 & i \\ i & 1 \end{bmatrix} \quad (150)$$

$$= \begin{bmatrix} it_1 \sinh g - it_2(z - z^{-1})/2 & t_1 \cosh g + t_2(z + z^{-1})/2 \\ t_1 \cosh g + t_2(z + z^{-1})/2 & -it_1 \sinh g + it_2(z - z^{-1})/2 \end{bmatrix}. \quad (151)$$

This model has been considered in [14]. As this gauge transformation does not depend on z , the boundary and the exponential decay requirement are unchanged. The transformed model shares the same SIBC spectrum as the non-Hermitian SSH model. To obtain the necessary boundary conditions, we explicitly write down the dynamics for both components of ψ_1 :

$$\begin{aligned} i \frac{d\psi_{A,1}}{d\tau} = & -\frac{it_2}{2} \psi_{A,2} + \frac{t_2}{2} \psi_{B,2} \\ & + it_1 \sinh g \psi_{A,1} + t_1 \cosh g \psi_{B,1} \\ & + \left(\frac{it_2}{2} \psi_{A,0} + \frac{t_2}{2} \psi_{B,0} \right), \end{aligned} \quad (152)$$

$$i \frac{d\psi_{B,1}}{d\tau} = \frac{t_2}{2} \psi_{A,2} + \frac{it_2}{2} \psi_{B,2} + t_1 \cosh g \psi_{A,1} - it_1 \sinh g \psi_{B,1} + \left(\frac{t_2}{2} \psi_{A,0} - \frac{it_2}{2} \psi_{B,0} \right), \quad (153)$$

where the terms in parentheses should be included if the cell is in the bulk, but excluded for a semi-infinite chain terminated at $n = 0$. To describe a semi-infinite chain, these terms should vanish to maintain the boundary condition:

$$\frac{it_2}{2} \psi_{A,0} + \frac{t_2}{2} \psi_{B,0} = 0, \quad (154)$$

$$\frac{t_2}{2} \psi_{A,0} - \frac{it_2}{2} \psi_{B,0} = 0. \quad (155)$$

Each of the four terms corresponds to a coupling removed at the boundary. Both equations are equivalent to

$$i\psi_{A,0} + \psi_{B,0} = 0, \quad (156)$$

which is exactly the transformed version of the boundary condition from the non-Hermitian SSH model. As such, the condition completely specifies the boundary, and it is unnecessary to impose $\psi_{A,0} = 0$ and $\psi_{B,0} = 0$ separately.

For a more general discussion, we consider a semi-infinite chain extending to the right. The dynamics of ψ_n with $n \geq p + 1$ are not affected by the SIBC. The dynamics of ψ_p contains contributions from ψ_0 , and these contributions should be set to 0 to maintain the boundary conditions:

$$t_{AA,-p} \psi_{A,0} + t_{AB,-p} \psi_{B,0} = 0, \quad (157)$$

$$t_{BA,-p} \psi_{A,0} + t_{BB,-p} \psi_{B,0} = 0. \quad (158)$$

The dynamics of ψ_{p-1} contains contributions from both ψ_{-1} and ψ_0 , which leads to

$$t_{AA,-p} \psi_{A,-1} + t_{AB,-p} \psi_{B,-1} + t_{AA,-p+1} \psi_{A,0} + t_{AB,-p+1} \psi_{B,0} = 0, \quad (159)$$

$$t_{BA,-p} \psi_{A,-1} + t_{BB,-p} \psi_{B,-1} + t_{BA,-p+1} \psi_{A,0} + t_{BB,-p+1} \psi_{B,0} = 0, \quad (160)$$

and so on. By considering the dynamics of ψ_m with m from 1 to p , we arrive at the following matrix form of boundary conditions:

$$T_{\text{left}} (\psi_{A,-p+1}, \psi_{B,-p+1}, \psi_{A,-p+2}, \psi_{B,-p+2}, \dots, \psi_{A,0}, \psi_{B,0})^T = 0, \quad (161)$$

where

$$T_{\text{left}} = \begin{bmatrix} t_{AA,-p} & t_{AB,-p} & t_{AA,-p+1} & t_{AB,-p+1} & \cdots & t_{AA,-1} & t_{AB,-1} \\ t_{BA,-p} & t_{BB,-p} & t_{BA,-p+1} & t_{BB,-p+1} & \cdots & t_{BA,-1} & t_{BB,-1} \\ 0 & 0 & t_{AA,-p} & t_{AB,-p} & \cdots & t_{AA,-2} & t_{AB,-2} \\ 0 & 0 & t_{BA,-p} & t_{BB,-p} & \cdots & t_{BA,-2} & t_{BB,-2} \\ \vdots & \vdots & \vdots & \vdots & \ddots & \vdots & \vdots \\ 0 & 0 & 0 & 0 & \cdots & t_{AA,-p} & t_{AB,-p} \\ 0 & 0 & 0 & 0 & \cdots & t_{BA,-p} & t_{BB,-p} \end{bmatrix}, \quad (162)$$

and the number of independent boundary conditions can be found as the rank of the coefficient matrix T_{left} , which has $t_{XY,m}$ with m from $-p$ to -1 as its block entries for each descending diagonal. In general, the rank of T_{left} equals P , the lowest order of z in the characteristic equation, and we only require P boundary conditions for the left

side of the chain (a more rigorous version of this statement as well as a general proof can be found in Appendix C).

With this in mind, we can substitute the ψ_m with m from $-p + 1$ to 0 using the superposition of individual z components. This results in a matrix equation for the component coefficients:

$$T_{\text{left}} V_{\text{multi}} (\alpha_{(1)}, \alpha_{(2)}, \dots, \alpha_{(P+w)})^T = 0, \quad (163)$$

where

$$V_{\text{multi}} = \begin{bmatrix} a_{(1)} z_{(1)}^{-p+1} & a_{(2)} z_{(2)}^{-p+1} & \cdots & a_{(P+w)} z_{(P+w)}^{-p+1} \\ b_{(1)} z_{(1)}^{-p+1} & b_{(2)} z_{(2)}^{-p+1} & \cdots & b_{(P+w)} z_{(P+w)}^{-p+1} \\ a_{(1)} z_{(1)}^{-p+2} & a_{(2)} z_{(2)}^{-p+2} & \cdots & a_{(P+w)} z_{(P+w)}^{-p+2} \\ b_{(1)} z_{(1)}^{-p+2} & b_{(2)} z_{(2)}^{-p+2} & \cdots & b_{(P+w)} z_{(P+w)}^{-p+2} \\ \vdots & \vdots & \vdots & \vdots \\ a_{(1)} z_{(1)}^0 & a_{(2)} z_{(2)}^0 & \cdots & a_{(P+w)} z_{(P+w)}^0 \\ b_{(1)} z_{(1)}^0 & b_{(2)} z_{(2)}^0 & \cdots & b_{(P+w)} z_{(P+w)}^0 \end{bmatrix}. \quad (164)$$

Unlike Eq. (82) for the single-band case, there are state components a and b appearing in V_{multi} and these depend on z implicitly. As such, V_{multi} is no longer a Vandermonde matrix, and there is no guarantee that V_{multi} is full rank. If V_{multi} is full rank, then $T_{\text{left}} V_{\text{multi}}$ has rank P . The P constraints remove P degrees of freedom from the system, resulting in w skin modes left. At specific ω values, the z solutions and the corresponding a and b components may reduce the rank of V_{multi} and $T_{\text{left}} V_{\text{multi}}$. Each additional deficit rank of $T_{\text{left}} V_{\text{multi}}$ leads to an extra mode for that specific ω , which is then identified as an edge mode in the system. To summarize, we have a weakened version of the bulk–boundary correspondence:

The winding number w of the PBC spectrum with respect to a specific frequency point ω_0 , calculated as a contour integral of the logarithmic derivative of the determinant, corresponds to the lower limit of SIBC modes found in the system. If $w \geq 0$, then at least w modes can be found on the left edge of a right-extending chain; if $w \leq 0$, then at least $-w$ modes can be found on the right edge of a left-extending chain. The “at least” phrase includes the contributions of additional edge modes, which is a consequence of the deficit rank for the coefficient matrix formed by the z and state amplitudes and cannot be directly inferred from the winding number information alone.

6.5. Open Boundary Conditions

The analysis of OBC spectra largely follows the SIBC procedure. After imposing OBCs on both ends, we obtain a set of equations similar to Eq. (90). However, the coefficients in the expanded determinant [Eq. (91)] are no longer Vandermonde determinants but submatrices of $T_{\text{left}} V_{\text{multi}}$ [as defined in Eqs. (162) and (164)] that contain state amplitudes. In general cases when the coefficients for the largest term $[z_{(P+1)} z_{(P+2)} \cdots z_{(P+Q)}]^N$ do not vanish, the same argument from the single-band OBC discussion in Section 5.1 leads to the condition of

$$|z_{(P)}| = |z_{(P+1)}| \quad (165)$$

where P replaces p in the single-band case. However, exceptions to this condition may occur when there are structural or symmetry constraints on the model [92], which are discussed in Section 6.5c. In addition to the continuous parts in the OBC spectrum, there may also be discrete points corresponding to left and right edge modes from the SIBC spectrum. The non-Hermitian skin effect discussion does not usually include the edge modes as their existence is not directly related to non-Hermiticity or the winding

number. Although edge modes decay into the bulk in the Hermitian cases, they can become delocalized and extend into the bulk if all the participating states have $|z| = 1$ [93,94], or even becomes localized on the opposite boundary [95].

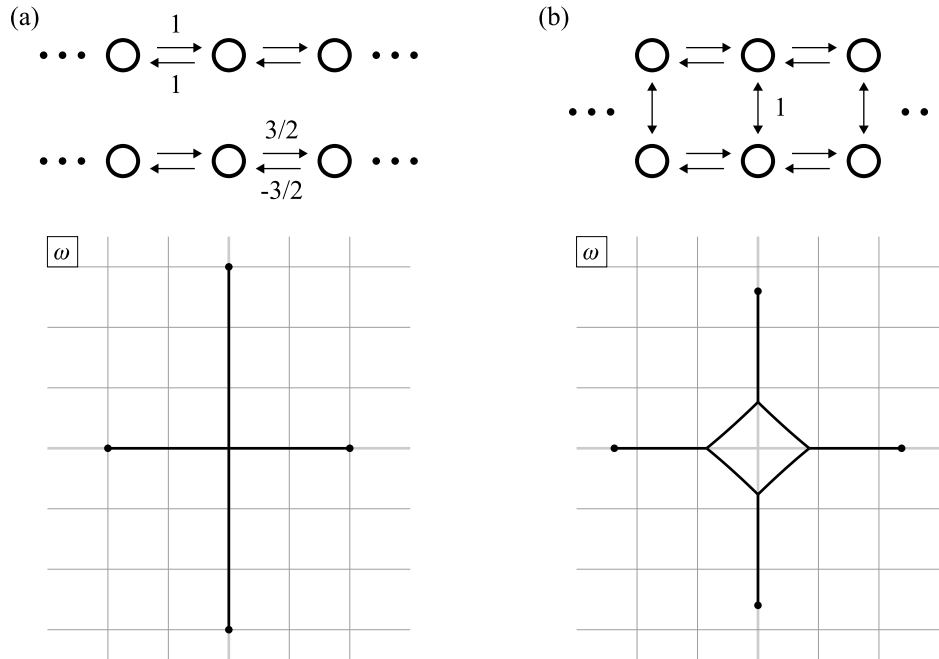
In the following, we assume that the tight-binding models are general enough (i.e., the OBC spectra are given by $|z_{(P)}| = |z_{(P+1)}|$) and focus on the continuous parts of the spectrum (i.e., edge modes will not be discussed).

6.5a. Properties of the Spectra

Most of the spectral properties for the single-band case can be carried over to the multiband case. For example, the self-intersection construction of the OBC spectra (Section 5.2) remains the same by replacing p with P . A major difference is that, whereas the single-band OBC spectra is always connected on the ω plane, a multiband OBC spectra may consist of multiple connected components (apart from the possible isolated edge modes). In general, the OBC spectra of a r -band model consists of at most r connected components, where the average number of modes per unit cell for each component is always a positive integer (see Appendix B). This is similar to the Hermitian r -band models that have r distinct bands, except that in the non-Hermitian case different bands may be merged together to form larger connected components.

For two-band models, the SSH models discussed in Section 6.2 provide examples of two-component OBC spectra, which attains the maximum possible number of components. On the other hand, it is not difficult to construct two-band models with a single-component OBC spectra; an example based on coupled Hatano–Nelson chains is provided in Fig. 34.

Figure 34



Construction of two-band models with single-component OBC spectra. (a) Top panel: Schematic of two Hatano–Nelson chains with $\omega = z^{-1} + z$ and $\omega = 3(z^{-1} - z)/2$. Bottom panel: OBC spectra of the two chains. (b) Top panel: Schematic of the two-band model $[z^{-1} + z, 1; 1, 3(z^{-1} - z)/2]$, where the two chains in (a) are coupled together. Bottom panel: OBC spectra of the model.

A related concept for the PBC spectrum is the “line gap,” which is a simple curve (i.e., a continuous curve without self-intersections) on the complex ω plane extending to $\omega = \infty$ that separates the complex PBC bands. This concept, together with the associated line-gap topology (continuous deformation of the model without any part of the spectrum touching the simple curve), can be applied to the topological classification of non-Hermitian models [50]. For two-band models, the existence of a line gap indicates that the PBC spectrum consists of two separate loops on each side of the gap. As such, a two-band model with a line gap necessarily has two OBC components, with one component in the regions with nonzero winding numbers for each loop of the PBC spectrum. We note that the existence of line gaps is not invariant under gauge transformations (e.g., Figure 31), and the existence of any line gap among the gauge transformed models leads to a two-component OBC spectrum. On the other hand, a two-component OBC spectrum does not imply the existence of a line gap of the PBC spectrum or among its gauge transformations, as the PBC spectrum loops may extend beyond their enclosed OBC components and fill in the space between them.

6.5b. Generalized Brillouin Zone

The GBZ for multiband models is the collection of $z_{(P)}$ and $z_{(P+1)}$ satisfying $|z_{(P)}| = |z_{(P+1)}|$ and can be constructed similarly to the single-band case. However, the shapes of the GBZ becomes more complex due to the presence of extra bands. For simplicity, we restrict ourselves to two-band models. For a two-component OBC spectrum, there are generally two GBZ loops, one for each component, and are sometimes labeled as GBZ+ and GBZ− [45]. For a single-component OBC spectrum, it is possible to have one or two GBZ loops. For Hermitian models the GBZ reduces to two copies of the BZ, but in general non-Hermitian models they may be separate or intersecting with each other. The intersection of GBZ loops may be confusing given that their corresponding spectra are separated, but this is simply an artifact of projecting from the Riemann surface onto the z plane and discarding the ω information associated with it. In Hermitian two-band models, a single wave vector in the BZ leads to two states, each with a different composition within the unit cell. The pair of (z, ω) together identifies a unique plane-wave state in the model, and two states may share the same ω (as in superposition arguments) or the same z (as in multiple bands for the same wave vector). The GBZ intersection point is an example of the latter and does not necessarily indicate any spectral features at that point. The discussions regarding discontinuous GBZs in Section 5.2 also applies here: the GBZ can become discontinuous for both two-component and one-component OBC spectra, leading to more connected components of GBZ than the number of bands.

6.5c. Exceptions to the General Condition

The $|z_{(P)}| = |z_{(P+1)}|$ condition requires that the coefficient of the asymptotic largest term in the determinant expansion [Eq. (91)] does not vanish in the multiband case. We illustrate how exceptions can occur with the following “two-band” model, where two Hatano–Nelson chains with opposite orientations are placed next to each other:

$$H = \begin{bmatrix} z^{-1}/2 + 2z & 0 \\ 0 & 2z^{-1} + z/2 \end{bmatrix}. \quad (166)$$

As the two chains do not couple, the PBC spectrum consists of two overlapping ellipses with opposite traversing directions. Similarly, the OBC spectrum is the union of two spectra from the individual chain, i.e., the line segment $-2 \leq \omega \leq 2$. However, a naïve application of $|z_{(2)}| = |z_{(3)}|$ leads to the PBC spectrum rather than the OBC spectrum. The failure of the $|z_{(P)}| = |z_{(P+1)}|$ condition is due to the ability to match boundary conditions within each component, and the decay rates of states across all

components may become out of order. From a mathematical point of view, we can analyze the state behaviors for ω values inside the PBC ellipse. Here the solutions are ordered in such a way that the $z_{(1)}$ and $z_{(2)}$ solutions comes from the first chain with $(a_{(1)}, b_{(1)})^T = (a_{(2)}, b_{(2)})^T = (1, 0)^T$ and the $z_{(3)}$ and $z_{(4)}$ solutions correspond to $(a_{(3)}, b_{(3)})^T = (a_{(4)}, b_{(4)})^T = (0, 1)^T$. Imposing the boundary conditions lead to

$$\begin{bmatrix} z_{(1)}^0 & z_{(2)}^0 & 0 & 0 \\ 0 & 0 & z_{(3)}^0 & z_{(4)}^0 \\ z_{(1)}^{N+1} & z_{(2)}^{N+1} & 0 & 0 \\ 0 & 0 & z_{(3)}^{N+1} & z_{(4)}^{N+1} \end{bmatrix} \begin{bmatrix} \alpha_{(1)} \\ \alpha_{(2)} \\ \alpha_{(3)} \\ \alpha_{(4)} \end{bmatrix} = 0. \quad (167)$$

We note that the $z_{(3)}^N z_{(4)}^N$ term is missing from the determinant expansion due to the linear-dependent $(a_{(3)}, b_{(3)})^T$ and $(a_{(4)}, b_{(4)})^T$, invalidating the argument for single-band models in Section 5.1a. Adding inter-chain couplings to the system, such as

$$H = \begin{bmatrix} z^{-1}/2 + 2z & \epsilon \\ \epsilon & 2z^{-1} + z/2 \end{bmatrix}, \quad (168)$$

with $\epsilon \neq 0$ as the coupling parameter, converts it into a genuine two-band model and restores the $|z_{(2)}| = |z_{(3)}|$ condition. This example demonstrates the fact that the OBC spectrum in the $N \rightarrow \infty$ limit can be discontinuous with respect to parameter changes (termed as “critical skin effects”) [96–98], and the order of $\epsilon \rightarrow 0$ and $N \rightarrow \infty$ limits cannot be interchanged [99]. For finite systems, this manifests as the extreme sensitivity of the finite-sized spectrum on ϵ that couples the states with different $|z|$, similar to the role of generalized boundary conditions in Section 5.4, and can lead to various finite-size effects [100,101].

6.6. Open-Boundary Spectra Under Symmetries

In the following, we consider how different symmetries constrain the behavior of the OBC spectra in multiband models [102,103].

6.6a. Hermiticity

Similar to the single-band case, Hermiticity requires all “to” and “from” coupling coefficients to be conjugates of each other:

$$t_{XY,m} = t_{YX,-m} \quad (169)$$

where X and Y are component labels. In terms of the matrix Hamiltonian we have

$$H(z) = H^\dagger[(z^{-1})^*] \quad (170)$$

When calculating the PBC spectrum, each H on the BZ $|z| = 1$ is a Hermitian matrix as $z = (z^{-1})^*$. The entire PBC spectrum is real, with winding number 0 on the ω plane with respect to every point outside the PBC spectrum. Following the argument from the single-band case (Section 5.3a), the GBZ coincides with $|z| = 1$ indicating no skin modes could be found [104]. We note again that the discussion does not apply to edge modes as they are not directly related to the winding numbers.

6.6b. Reciprocity

Reciprocity is a rather subtle symmetry when there are internal degrees of freedom for each unit cell. As discussed in [37], the condition of reciprocity may not be respected

by unitary transformations. Here we focus on the individual sites and require that all “to” and “from” coupling coefficients be equal:

$$t_{XY,m} = t_{YX,-m} \quad (171)$$

and, in terms of the matrix Hamiltonian,

$$H(z) = H^T(z^{-1}). \quad (172)$$

For the PBC spectrum, $H(e^{ik})$ and $H(e^{-ik})$ share the same eigenvalues, and the PBC curves backtrack themselves after $k = \pi$. Following the argument from the single-band case (Section 5.3b), no skin modes could be found if there are reciprocity constraints. A photonic crystal example is demonstrated in [105].

6.6c. Sublattice Symmetry

The existence of multiple sites within a single unit cell allows the discussion of symmetries involving individual components that are not present in single-band models. A representative example is the sublattice symmetry for two-band models, which is the existence of a unitary Hermitian operator Γ without z dependence that anti-commutes with $H(z)$:

$$\Gamma H(z) \Gamma^{-1} = \Gamma H(z) \Gamma^\dagger = -H(z). \quad (173)$$

In practice, Γ is usually taken to be σ_3 , the third Pauli matrix, for convenience. This does not affect the generality of results as we can always perform unitary transformations on both Γ and $H(z)$. An immediate consequence is that $H(z)$ can only have off-diagonal elements:

$$H(z) = \begin{bmatrix} 0 & H_{AB}(z) \\ H_{BA}(z) & 0 \end{bmatrix}. \quad (174)$$

In terms of couplings, the two-band sublattice symmetry forbids any coupling between sites with the same component labels. The SSH model and its non-Hermitian extension discussed previously are examples of models with sublattice symmetry. The spectrum of a sublattice-symmetric model will be central symmetric on the ω plane with respect to $\omega = 0$ since the eigenmode ψ at energy ω can be mapped to its partner $\Gamma\psi$ at energy $-\omega$. This applies to all PBC, SIBC, and OBC spectra. We note that one-component OBC spectra under this symmetry does not necessarily pass through $\omega = 0$; the components may be joined together at other locations on the ω complex plane.

Although the edge mode properties have been related to the winding numbers of the individual matrix elements $H_{AB}(z)$ and $H_{BA}(z)$ [57], sublattice symmetry alone does not imply the presence or absence of the non-Hermitian skin effect, as this symmetry cannot be broken by imaginary gauge transformations. However, since the band structure is in the form of $\omega^2 = H_{AB}(z)H_{BA}(z)$, many spectral properties can be derived from the single-band model corresponding to $\omega_{\text{single}} = H_{AB}(z)H_{BA}(z)$ and taking the square root $\omega = \pm\sqrt{\omega_{\text{single}}}$ [106]. For example, as the $|z_{(P)}| = |z_{(P+1)}|$ condition does not explicitly depend on ω , the GBZ of the sublattice-symmetric model is simply two copies of the GBZ for ω_{single} , and the OBC mode frequencies are square roots of the OBC spectra from ω_{single} .

7. CALCULATING THE OPEN-BOUNDARY SPECTRA

To determine the spectral properties of a model with given coupling coefficients, efficient procedures of extracting its PBC, SIBC, and OBC spectra are required. Calculating the PBC spectrum is equivalent to calculating the band structure, which is the characteristic polynomial of $H(z)$ for tight-binding models. The calculation of

SIBC spectrum reduces to finding the winding numbers for different regions divided by the PBC spectrum if we are not concerned with edge modes. On the other hand, it is not immediately clear how the analytical condition for the OBC mode existence $|z_{(P)}| = |z_{(P+1)}|$ can be utilized to calculate OBC spectra from the band structure.

In the following, we list some analytical and numerical approaches for determining the OBC spectra. For each method, we discuss its operating principle and compare its advantages and disadvantages to other methods. In this tutorial, the spectra for various models have been obtained by switching between different approaches. Full analytical results [e.g., Eqs. (57) and (58), Figs. 10(d) and 23] are obtained with the analytical approach (Section 7.1), numerical results for $N \rightarrow \infty$ [e.g., Figures 24 and 34(b)] are obtained with the semi-analytical approach (Section 7.2) and numerical results for finite N [e.g., Figures 10(c) and 28(e)] are obtained with the numerical direct approach (Section 7.3). The code for these figures is provided in Code 1, Ref. [107].

7.1. Analytical Approach

As both the GBZ and the OBC spectrum are based on the algebraic condition $|z_{(P)}| = |z_{(P+1)}|$, they can be determined with algebraic methods for tight-binding models [45]. The idea is to “solve” $|z_{(P)}| = |z_{(P+1)}|$ from the band structure, resulting in polynomial equations of z_r and z_i (the GBZ) or ω_r and ω_i (the OBC spectrum). This is achieved through *resultants* [108], a determinant formed by the coefficients of two polynomials in z , which vanishes if and only if the two polynomials have at least one common root of z . The resultant can be efficiently computed with modern computer algebra systems.

In the following, we outline a procedure of algebraically deriving the GBZ and the OBC spectrum, taking $\omega = z^{-1} + z + 3z^2$ from Section 3.2 as an example.

(1) Eliminate ω from two copies of the band structure, $\omega - \omega(z_{(P)}) = 0$ and $\omega - \omega(z_{(P+1)}) = 0$, obtaining the relation between $z_{(P)}$ and $z_{(P+1)}$ (for single-band models we interpret P as p). For $3z_{(P)}^3 + z_{(P)}^2 - \omega z_{(P)} + 1 = 0$ and $3z_{(P+1)}^3 + z_{(P+1)}^2 - \omega z_{(P+1)} + 1 = 0$, the resultant of them reads

$$(z_{(P+1)} - z_{(P)}) [3z_{(P)}z_{(P+1)}(z_{(P)} + z_{(P+1)}) + z_{(P)}z_{(P+1)} - 1] = 0. \quad (175)$$

For single-band models, it suffices to use $\omega(z_{(P)}) - \omega(z_{(P+1)}) = 0$ directly, but a proper resultant operation is required for multiband models to get the relation. This relation always contain $z_{(P+1)} - z_{(P)}$ as a factor because $z_{(P)} = z_{(P+1)}$ makes it trivial to satisfy both band structures simultaneously. We can factor this out and consider the remaining part symmetric in $z_{(P)}$ and $z_{(P+1)}$, i.e.,

$$3z_{(P)}z_{(P+1)}(z_{(P)} + z_{(P+1)}) + z_{(P)}z_{(P+1)} - 1 = 0. \quad (176)$$

(2) From $z_{(P)}z_{(P)}^* - z_{(P+1)}z_{(P+1)}^* = 0$, eliminate $z_{(P+1)}$ using Eq. (176), then eliminate $z_{(P+1)}^*$ using the conjugate of Eq. (176). This amounts to performing two successive resultant operations while treating $z_{(P+1)}$ and $z_{(P+1)}^*$ as algebraically independent variables. After this step we obtain the GBZ expressed in $z_{(P)}$ and $z_{(P)}^*$. Calculating the resultant of $z_{(P)}z_{(P)}^* - z_{(P+1)}z_{(P+1)}^* = 0$ and $3z_{(P)}z_{(P+1)}(z_{(P)} + z_{(P+1)}) + z_{(P)}z_{(P+1)} - 1 = 0$ [Eq. (176)], viewed as polynomials of $z_{(P+1)}$, gives

$$3z_{(P)}^3(z_{(P)}^*)^2 + 3z_{(P)}^3z_{(P)}^*z_{(P+1)}^* + z_{(P)}^2z_{(P)}^*z_{(P+1)}^* - (z_{(P+1)}^*)^2 = 0. \quad (177)$$

Calculating the resultant of Eq. (177) and $3z_{(P)}^*z_{(P+1)}^*(z_{(P)}^* + z_{(P+1)}^*) + z_{(P)}^*z_{(P+1)}^* - 1 = 0$ [conjugate of Eq. (176)], now viewed as polynomials of $z_{(P+1)}^*$, gives the GBZ:

$$\begin{aligned} & [3zz^*(z + z^*) + zz^* - 1] \\ & [9(zz^*)^4 + 9(zz^*)^2(z^2 - zz^* + z^{*2}) + 3(zz^*)^2(z + z^*) + 3zz^*(z + z^*) + zz^* + 1] \\ & = 0, \end{aligned} \quad (178)$$

where we have dropped the (P) subscript for simplicity. The GBZ can also be expressed using z_r and z_i with the substitution $z = z_r + iz_i$ and $z^* = z_r - iz_i$, which is helpful for generating plots on the z plane. In our case, the GBZ factors into two terms allowing them to be considered separately, but this is not always the case in general models.

(3) Finally, from the GBZ, eliminate z using the band structure, then eliminate z^* using the conjugate of the band structure. This again amounts to performing two successive resultant operations that map the GBZ to the ω plane, which results in the OBC spectrum. The factored form of GBZ allows us to complete this procedure using each factor separately. For the shorter factor of Eq. (178), the corresponding result is

$$(\omega - \omega^*)^6 = 0. \quad (179)$$

This gives the real axis on the ω plane, which contains the horizontal section of the OBC spectrum. For the longer factor of Eq. (178), the resulting expression is given by the square of Eq. (58).

We note that the procedure does not technically constitute a complete algorithm for the GBZ and OBC spectra calculation. As the ordering of z and the conjugation operation cannot be incorporated in a purely algebraic way, the analytical expression for GBZ will also include the auxiliary GBZ (the collection of z values with $|z_{(s)}| = |z_{(s+1)}|$ and $1 \leq s < P + Q$) [45] as well as other spurious segments. To isolate the correct GBZ segments, we can select a z point on the segment, solve the associated ω and numerically verify if the $|z_{(P)}| = |z_{(P+1)}|$ condition holds for at least one ω .

The distinctive advantage of the analytical approach is the ability to produce exact results for any exact input of tight-binding coupling coefficients (including the case where the couplings are unknown variables), which is useful to study model transitions with respect to parameter changes. However, there are also significant drawbacks due to the symbolic nature of this approach, which utilizes polynomial operations and arbitrary-precision arithmetic that are not directly available in many programming languages. In addition, the degrees of polynomials that are used to determine the GBZ and OBC spectra increase rapidly with the band structure degree $P + Q$, and manipulating these polynomials requires a significant amount of computational resources. As such, this approach is more suited to validating the results from faster numerical methods when necessary.

7.2. Semi-Analytical Approach

The $|z_{(P)}| = |z_{(P+1)}|$ condition implies that there is a real number θ with $z_{(P+1)} = e^{2i\theta} z_{(P)}$. Instead of using a single polynomial to cover all the possible values of θ , we can assign numerical values to θ and solve for both $z_{(P)}$ and $z_{(P+1)}$ [109]. The GBZ and the OBC spectra can then be obtained by collecting all the solutions when θ is being varied.

This approach begins by calculating the resultant between $\omega - \omega(z_{(P)}) = 0$ and $\omega - \omega(z_{(P+1)}) = 0$, which is the same as the first step in the analytical method, and leads to a relation between $z_{(P)}$ and $z_{(P+1)}$. Now we define $\zeta = z_{(P)} e^{i\theta} = z_{(P+1)} e^{-i\theta}$, where θ is real if the GBZ condition is satisfied. As $z_{(P)}$ and $z_{(P+1)}$ can be interchanged when their modulus is equal, we only require $0 < \theta \leq \pi/2$ to cover all solutions. If θ is substituted with a numerical value, the relation between $z_{(P)}$ and $z_{(P+1)}$ becomes a polynomial equation in ζ , and all ζ solutions can be obtained with a standard polynomial root finder. These solutions will contain both the GBZ and the auxiliary GBZ similar to the analytical approach (Section 7.1), and should be verified by plugging these back into the band structure and selecting only the solutions that leads to $|z_{(P)}| = |z_{(P+1)}|$. By sampling enough θ values, we obtain a corresponding sampling of the GBZ on the z plane or the OBC spectrum on the ω plane.

This approach is a more efficient substitute to the analytical procedure when the full analytical form of the GBZ is not required. With only one resultant calculation, the symbolic processing overhead is relatively low, but the procedure remains “exact” as it is a direct numerical sampling of the underlying GBZ. The efficiency improvement results from replacing symbolic resultant calculations for the GBZ with numerically solving many algebraic equations. An additional advantage that is physically relevant is that, if θ is uniformly sampled on $0 < \theta \leq \pi/2$ (e.g., by dividing the interval into equal segments), then the density of points in the sampled OBC spectrum represents the actual density of states in the $N \rightarrow \infty$ limit (see Appendix B).

7.3. Numerical Direct Approach

As the system dynamics can be put into a matrix form [Eqs. (3) and (123)], the direct way of calculating the OBC spectrum is to numerically diagonalize the matrix Hamiltonian. The GBZ, if required, can be obtained by solving for z in the band structure for each eigenvalue ω , where $|z_{(P)}| = |z_{(P+1)}|$ should hold approximately. This allows a numerically exact computation of the OBC spectra at any finite N . Since the matrix does not need to be (block) Toeplitz to be numerically diagonalized, the implementation of generalized boundary conditions within this approach becomes straightforward [e.g., Equation (117)]. Edge modes, if present, will also show up in the spectrum, whereas the previous procedures based on $|z_{(P)}| = |z_{(P+1)}|$ do not capture the properties of the edge modes. On the other hand, the matrix Hamiltonian only represents the dynamics for a specific N , and the GBZ or OBC spectra behavior may differ qualitatively from the $N \rightarrow \infty$ limit (e.g., Section 6.5c).

Although this procedure is numerically exact in principle, it is subject to numerical errors introduced in the numerical diagonalization routine. A small change in matrix elements or the numerical eigenvectors may induce a large change in the resulting spectrum due to the extreme sensitivity (Section 5.4), and the calculated spectrum may become distorted compared with the true spectrum of a finite system. This effect becomes more prominent for large N , and it is important to choose a reasonable N when trying to infer the spectral properties in the $N \rightarrow \infty$ limit based on numerical data. To minimize the effects of numerical error, arbitrary-precision arithmetic can be used instead of floating-point arithmetic, and the precision limit can be further increased at the cost of computation time [45]. Another efficient way to reduce numerical error is to precondition the matrix by applying gauge transformations such that the anticipated eigenmodes have $|z|$ values close to 1 (i.e., scale the GBZ and make it closer to the BZ).

7.4. Numerical Approach Based on Gauge Transformations

As discussed in Section 5.2, the $|z_{(P)}| = |z_{(P+1)}|$ condition can be viewed as the self-intersection points of iso- $|z|$ contours, and the collection of such points for all contours leads to the OBC spectra [58]. The GBZ, if required, can be reconstructed by also recording the scaling factor z_0 used for the gauge transformation and the $\text{Arg}(z)$ value along the contour at the intersections.

Different from all previous approaches utilizing various algebraic properties, this approach relies on the geometric properties of the PBC spectrum curve, and its precision depends on the accuracy of the PBC curves of all gauge-transformed models. However, the full analytic form of the band structure is not needed if the PBC spectrum of any gauge-transformed model can be obtained with high accuracy. As such, this approach has the potential to be applied to continuous systems such as photonic crystals, where discretization of the domain allows the system to be approximated by tight-binding models [110] and gauge transformations can be implemented by modified boundary conditions in the unit cell. Although there are preliminary photonic crystal

examples demonstrating that the OBC spectrum passes through self-intersections of the PBC spectrum [105], a set of sufficient conditions for the applicability of this approach has yet to be formulated to the best of the authors' knowledge.

8. EXPERIMENTAL IMPLEMENTATIONS AND POTENTIAL APPLICATIONS

The non-Hermitian skin effect has been theoretically studied in various platforms. These include photonics [110–118], polaritons [119–122], magnetics [123–126], mechanics and elastic systems [127–133], acoustics [134,135], electrical circuits [136,137], atomic physics [138–142], crystal defects [143–147], quadratic-bosonic system with squeezing [148,149], and heat diffusion [150,151]. In many of these platforms, the non-Hermitian skin effect have been experimentally demonstrated.

8.1. Experiments

In Table 3, we list different platforms where either the non-Hermitian skin effect for OBC or eigenvalue winding (nontrivial point-gap topology) for PBC has been demonstrated experimentally. For brevity, we have not included references on experimental demonstrations of eigenvalue braiding [84–91] in the table, where there have also been exciting developments.

The non-Hermitian skin effect was first demonstrated in photonic walks in optical fibre loops [152] and in quantum optics using single-photon quantum walks [183]. Since then, the non-Hermitian skin effect or the effect of nontrivial point-gap topology has been demonstrated in various one-dimensional experimental platforms including electrical circuits [160–163], optical ring resonator systems [157,177], ultracold atoms [186], acoustic systems [178], metamaterials [170,172,173], laser arrays [155], and thermal diffusion lattices [189]. These effects have also been demonstrated in two dimensions using phononic crystals [190], acoustic crystals [181], and active mechanical lattices [191]. Liu *et al.* [154] demonstrated experimentally non-Hermitian skin effects in gyromagnetic photonic crystals, and considered interesting interplay between eigenvalue and eigenvector topology. Another interesting model for experimental demonstration of the non-Hermitian skin effect is the bosonic Kitaev chain [148,192] which has been experimentally realized using optomechanics [174] and superconducting circuits [187].

8.2. Applications

Here we briefly review potential applications for non-Hermitian skin effects and related phenomena. These effects have been extensively considered for enhancing sensing applications. As noted in Section 5.4, with respect to change in boundary conditions, non-Hermitian systems can exhibit sensitivity that scales exponentially as the system size. Thus, non-Hermitian skin effects are of potential interest for sensing applications if one can couple the quantities to be sensed with the change in boundary conditions [193]. For actual sensor applications, on the other hand, it is important to analyze not just sensitivity enhancement, but the change of signal-to-noise ratio. Related analysis has been performed in [194–197].

The non-Hermitian skin effect has also been considered in laser systems. For example, Zhu *et al.* [198] proposed to achieve single-mode lasing at high pump powers using these effects. In a system exhibiting non-Hermitian skin effects, almost all modes are skin modes localized on the edge. At sufficiently high pump power, through nonlinear mode competitions, a single extended mode can then dominate over all these skin modes in the system, resulting in single-mode lasing in an extended laser array. Leefmans *et al.* [156] considered the implications of non-Hermitian skin effects in mode-locked laser systems.

Table 3. Experimental Demonstrations of the Non-Hermitian Skin Effect or Eigenvalue Winding in Various Platforms

| Platform | Experimental Setup | Model |
|--|---|--|
| Photonics and optics | Optical fiber loops and acoustic optic resonators [152,153], two-dimensional gyromagnetic photonic crystal [154], active nonlinear oscillators (laser array) [155], synthetic dimensions in photonic time-multiplexed resonators [156], synthetic frequency dimensions in ring resonators [157], two-dimensional on-chip gauged laser array [158], one- and two-dimensional optical array of lossy helical waveguides [159] | Non-Hermitian SSH model [152,156], skin-edge states in continuous two-dimensional photonic crystal [154], Hatano–Nelson model [155,156], non-Hermitian Floquet Aubry–André–Harper model [153], Hatano–Nelson model with long-range hoppings [157], generalized two-dimensional Hatano–Nelson model [158], Floquet skin-topological effect in 1D and 2D tight-binding lattice [159] |
| Electrical circuits | RLC circuit [160 161 162 163 164 165 166 167–168] | Non-Hermitian SSH model [160,161,167], two-dimensional tight-binding model [162,164], skin-edge and skin-edge-edge states in two-dimensional and three-dimensional tight-binding models [163,166], three-dimensional lattice using N -boson one-dimensional Bose–Hubbard model [165], rank-two skin effect in two-dimensional single band tight-binding lattice [168] |
| Mechanics, active matter | static mechanical metamaterial [169], active mechanical metamaterial [170,171], robotic metamaterial [172], piezoelectric metamaterial [173], squeezing in optomechanical network [174], active particles [175], two-dimensional active mechanical lattice [176] | One-dimensional wave in static Rayleigh model [169], two-dimensional elastic medium with odd mass density tensors [171], non-Hermitian SSH [170], Hatano–Nelson [172], bosonic Kitaev chain [174], second-order skin effect in two-dimensional stochastic tight-binding model [175], one-dimensional micropolar beam theory [173], non-Hermitian Kagome lattice [176] |
| Acoustics | One-dimensional chain of three coupled ring resonators [177], one-dimensional chain of acoustic resonators [178,179], two-dimensional array of whispering-gallery resonators [180], two-dimensional array of sonic resonators [181], two-dimensional phononic crystal [182] | One-dimensional three-band tight-binding model [177], Hatano–Nelson model with on-site loss [178,179], two-dimensional spinful SSH [180], geometry-dependent skin effect in two-dimensional tight-binding model [181,182] |
| Atomic, molecular, and optical (AMO) systems | Polarized single photons [183 184–185], Bose–Einstein condensate of ^{87}Rb atoms [186], squeezing in superconducting circuits [187], multiterminal AlGaAs/GaAs two-dimensional electron gas ring [188] | Quantum walk on one-dimensional lattice (Floquet operator) [183 184–185], dissipative Aharonov–Bohm chain [186], bosonic Kitaev chain [187], Hatano–Nelson model [188] |
| Thermal systems | Thermal diffusion lattice [189] | Non-Hermitian SSH model [189] |

Other applications of non-Hermitian skin effects include potential applications in amplifiers [199,200]. Non-Hermitian dynamics has been considered in a bosonic Kitaev chain [148,174,187], and the non-Hermitian skin effects can manifest in the squeezing properties of the system. A recent paper has also noted the implications of non-Hermitian skin effects for cooling [201].

9. SUMMARY AND OUTLOOK

In this tutorial, we have provided a detailed discussion of the physics and mathematics that underlies the topological band winding and the non-Hermitian skin effect. We have made extensive use of tight-binding models in one-dimensional systems, and focused exclusively on the linear modal properties of non-Hermitian systems. The

mathematics has highlighted the connection between the non-Hermitian skin effects and the topological properties of the bulk band structures.

There are many future directions of interests in the study of non-Hermitian skin effects and related phenomena. A major direction is the non-Hermitian skin effect in higher dimensions [22,202–209]. Skin effects unique to models in two or more dimensions have been discovered, including the geometry-dependent skin effect [210–212] and the higher-order skin effect [213–225]. The geometry-dependent skin effect describes the situation where the presence of the skin effect depends on the spatial orientation of the lattice boundary. For two-dimensional systems, the geometry-dependent skin effect has been explained with the reduced one-dimensional band structure slice of the two-dimensional band structure [210]. When a one-dimensional band structure slice has nontrivial point-gap topology, a lattice with a truncation in the direction perpendicular to the slice would inherit the skin effect from the one-dimensional band structure. The two-dimensional band structure may have one-dimensional band structure slices with different point-gap topology, making these skin effects geometry-dependent. The connection of the geometry-dependent skin effects to exceptional points in the wave vector plane has also been demonstrated [182,210]. On the other hand, higher-order skin effects include skin modes on boundaries, skin modes on corners as well as hybrid skin-edge modes that are a combination of the skin effect and topological boundary modes from eigenvector topology. The total number of each kind of mode is typically proportional to N^s , where N is the lattice size, d is the dimension and $s < d$ [217].

A complete and concise framework to unify these effects for these various higher-dimensional phenomena has not yet been found. The geometry dependence suggests that the one-dimensional GBZ description cannot be generalized in a straightforward manner to higher-dimensional models [226,227]. Some related theoretical analysis includes constructing mappings from higher-dimensional models to lower-dimensional ones [227,228] and using concepts from tropical geometry [229].

Theoretical approaches beyond the usual spectral and topological properties have also been proposed. For example, non-Hermitian topological effects have been related to the nonnormality of Hamiltonians [230,231] or examined from a transfer matrix perspective [104]. A reflection matrix with the non-Hermitian skin effect has been shown to lead to unconventional Goos–Hänchen effects [232]. Given the connections between the non-Hermitian skin effect and scattering properties [63,64,68,69,233], the relation between the topology of scattering matrices [234] and the non-Hermitian topology are worth exploring. Different approaches to non-Hermitian topological invariants have also been proposed in real space [235], for defective edge states [236], and for dynamics [237].

The non-Hermitian skin effect is closely related to gauge transformations that analytically continues the PBC spectrum to the complex wave vector plane and can be utilized to construct the GBZ (Section 5.2). Similar concepts include complex flux threading [57] and interpolating boundary conditions [73,75]. In fact, the early non-Hermitian physics literature using imaginary gauge transformations for the “non-Hermitian delocalization transition” [41] is highly related to the skin effect. As such, localization phenomenon similar to the non-Hermitian skin effects have been discussed in Mott insulators [238], continuum models [239], and disordered systems [240] as early as the 1990s. The technique of applying imaginary gauge transformation to non-Hermitian delocalization transition has also been utilized in other areas, including many-body localization [241] and polymers in periodic potentials [242].

Apart from the intriguing spectral properties, non-Hermitian skin effect also leads to novel dynamical effects in the time domain [243–247] and in Floquet or driven systems [116,159,248,249]. For quantum systems, non-Hermitian skin effects can lead to the

Liouvillian skin effect [205,250–253], point-gap topology in Fock space [254], and entanglement [255,256]. We expect more connections between non-Hermitian topology and quantum effects to be found. An interesting application of the non-Hermitian skin effect is in quadratic bosonic Hamiltonians, where the non-Hermiticity resides in the dynamical matrix while the overall Hamiltonian is Hermitian [148,149,174,187], leading to a quadrature non-Hermitian skin effect or squeezing. We also expect more interplay of non-Hermitian skin effects with external fields, such as with Stark localization and electric fields [257] and magnetic fields [123–126].

Outside the linear regime, extensions of skin effects to nonlinear systems have been proposed [258–260], and there have been discussions of applying the skin effect to solitons [261,262]. The non-Hermitian skin effect and band winding has also been applied to many-body systems [263–277]. An interesting and simple application of the skin effect in a two-body system is that the center-of-mass Hamiltonian may resemble a Hatano–Nelson chain, leading to a correspondence between two-body bound states and the non-Hermitian skin effect [266,278].

Practical implementations of non-Hermitian skin effects would likely require understandings of models beyond tight-binding approximations. From a topological point of view, it can be reasonably expected that the statements not explicitly depending on the coupling ranges, such as the bulk–boundary correspondence and the graphic construction of the OBC spectrum, may be applied beyond tight-binding models. Examples of existing studies include the continuous Schrödinger equation [106,239,279], photonic crystals [105,110,118,154], long-range quantum emitters [124,209,280,281], field-theoretic models [282], and more. Long-range models have different dispersion relations which may be modeled with Toeplitz matrices with a rational symbol [283]. Furthermore, many interesting properties arise when combining non-Hermitian skin effects with interfaces, defects, and heterojunctions [65,284–291]. One example is scale-free localization states [286,291], which is related to critical skin effects [96]. Related directions include non-Hermitian skin effects in systems where perfect periodicity is broken, such as in fractals or quasicrystals [292–307], as well as the interplay of non-Hermitian effects with randomness, disorder, or Anderson localization [233,308–315].

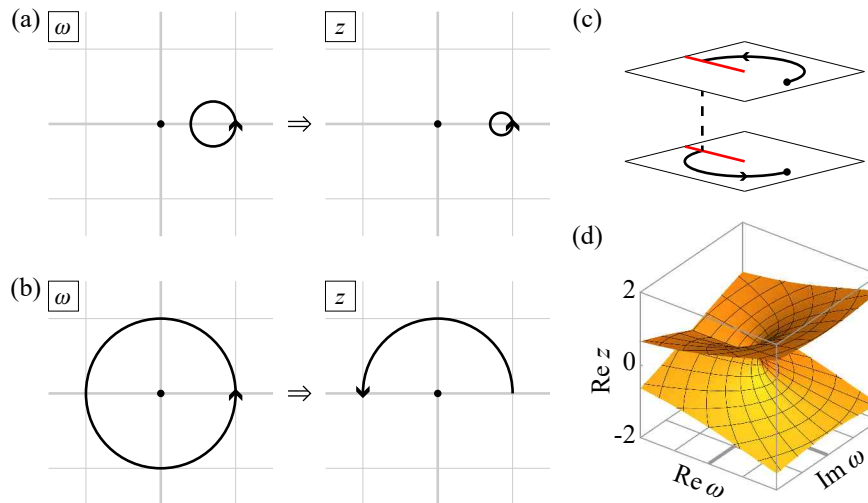
Given that the main ingredients of non-Hermitian skin effects (non-Hermiticity and nonreciprocity) are quite ubiquitous, we expect that new connections of skin effects to other unexpected areas may arise. Existing examples include pay-off matrices of rock–paper–scissors [316], curved spaces [317], biological networks [318], stochastics [308], detailed balance problems [175], directed random graphs (of relevance to applications such as social networks) [319], as well as recurrent neural networks and synaptic connectivity matrices [320,321]. Furthermore, deeper understandings of related mathematical topics, such as Riemann surfaces [45–48], tropical geometry [229,322], and generalized eigenvalue problems [323], may lead to new insights of non-Hermitian physics.

APPENDIX A. RIEMANN SURFACES

Riemann surfaces are useful tools in understanding the global structure of multivalued complex functions. We collect some related concepts here and demonstrate them with examples.

The prototypical multivalued complex function is the square root function $z = \sqrt{\omega}$ (Fig. 35). Although there are, in general, two different values of z satisfying $z^2 = \omega$, only one of them is chosen as the function value of $\sqrt{\omega}$. If ω continuously varies in its neighborhood, the z values also change continuously, defining an analytic function that

Figure 35



Construction of the Riemann surface for $z = \sqrt{\omega}$. (a) If ω continuously varies in its neighborhood, the z values also change continuously. (b) If the path of ω circles around zero, the z value will continuously change to $-z$. (c) We can take two copies of the ω plane and require each ω point to map to a different z , then gluing them together. The path shown in (b) now spans across both copies of ω plane. (d) A three-dimensional rendering of the Riemann surface.

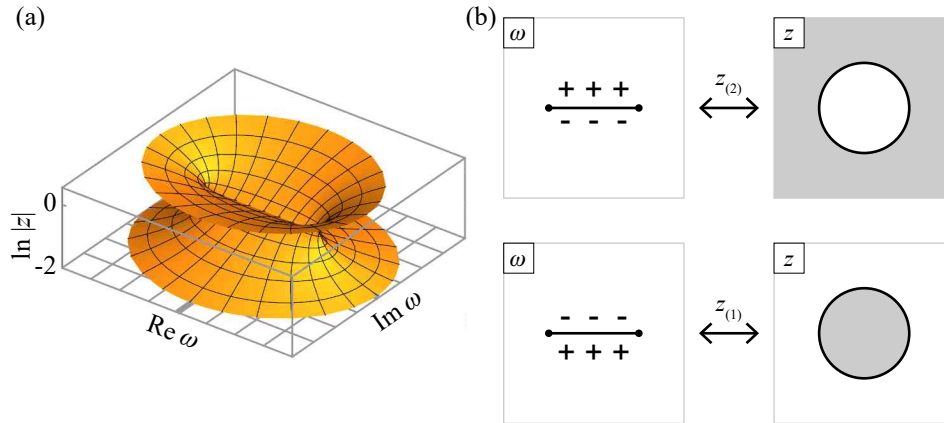
is locally single-valued. However, if ω is varied along a path circling around $\omega = 0$, the z value will continuously change to $-z$ instead of returning to z , indicating the impossibility of extending the analytic function to the entire ω plane. The $\omega = 0$ point is therefore the *branch point* of the function; the $\omega = \infty$ point is another branch point. We can take two copies of the ω plane and require each ω point on each plane to map to a different z , forming a single-valued mapping as a whole. These two planes need to be glued together to ensure that the ω switch planes when continuously circling around a branch point. To do so, we cut the planes along the *branch cut*, a smooth curve connecting the branch points (here $\omega = 0$ and ∞), and glue the two planes together along the cut, with one side of the cut on one plane glued to the other side on the other plane. The resulting structure is a *Riemann surface*, where each point on the surface represents a unique pair of ω and z .

Since the branch points are the points where ω as a function of z fails to be invertible, the locations of the branch points can be determined from $\partial_z \omega = 0$. Together with $\omega = \omega(z)$, z can be eliminated, resulting in an equation of ω . In the case of tight-binding band structures, ω is a Laurent polynomial of z , which can always be factored into linear terms in the complex plane by the fundamental theorem of algebra. As such, $\partial_z \omega = 0$ indicates the locations where $\omega = \omega(z)$ have duplicate roots. In fact, the result of eliminating $\partial_z \omega = 0$ from $\omega = \omega(z)$ is the *discriminant* of the band structure (as a polynomial of z), which equals 0 if there are duplicate roots in $\omega = \omega(z)$. Therefore, the branch point locations are exactly where the degeneracy of z will occur. To determine whether the infinity point is a branch point, we can compute whether ω^{-1} has a branch point at 0. There are many ways to draw the branch cuts on the ω plane, as long as the drawing divides the plane into regions that support single-valued continuous mappings. For example, the branch cut for $z = \sqrt{\omega}$ can be any smooth curve connecting 0 and ∞ . This is because the band structure as a Riemann surface is continuous everywhere, and the multivalued nature of the mapping as well as the branch cuts induced is an artifact of projecting the Riemann surface onto the ω plane. A different projection would lead

to a different division of single-valued sheets. However, a preferred branch cut may be constructed that corresponds to physical quantities, discussed in the following.

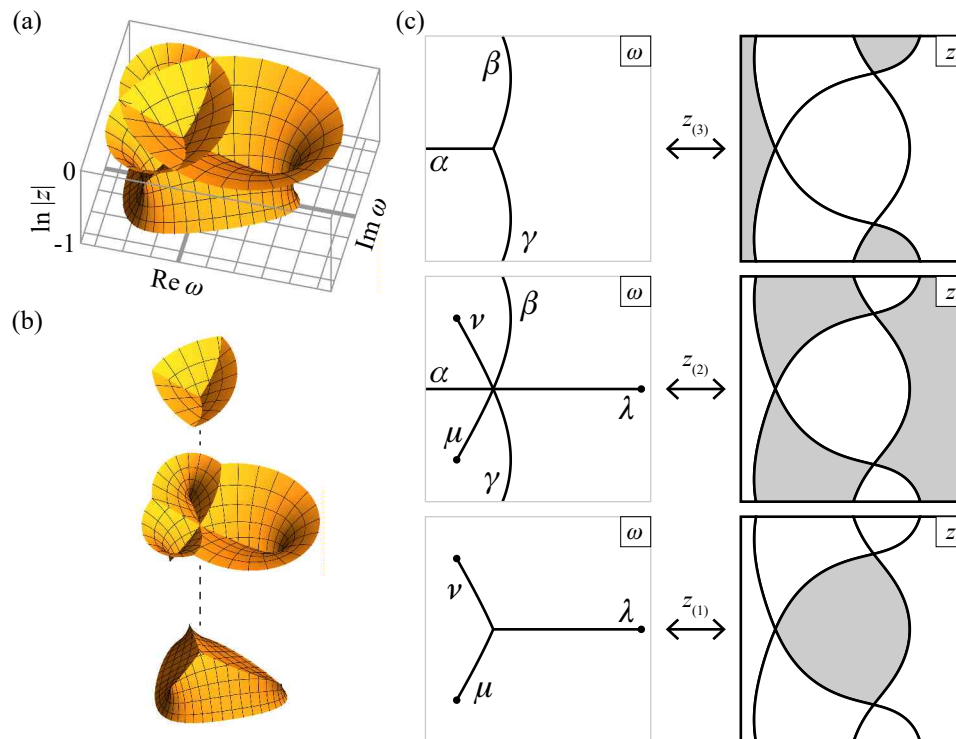
The Riemann surface can naturally be represented in a four-dimensional real space (with z and ω each taking two real coordinates). We can project this representation into

Figure 36



Riemann surface of the Hatano–Nelson model $\omega = z^{-1}/2 + 2z$. (a) A three-dimensional rendering of the Riemann surface. (b) A planar rendering, showing each single-valued sheet and its range on the z plane. The sides of the branch cuts with matching signs should be glued together.

Figure 37



Riemann surface of the model $\omega = z^{-1} + z + 3z^2$. (a) A three-dimensional rendering of the Riemann surface. (b) An exploded view of the three individual sheets. (c) A planar rendering, showing each single-valued sheet and its corresponding z sections. Two branch cuts with matching Greek letters should have opposite sides glued together.

a three-dimensional space by using a real-valued function of z instead of the complex z . Common choices include $\text{Re}(z)$, $\text{Im}(z)$ and $\ln |z|$. This provides a visualization of the Riemann surface structure; two examples using the models from Section 3 are given in Figs. 36 and 37. These two Riemann surfaces can be compared with Figs. 15 and 16, where the iso- $|z|$ contours are horizontal cross sections of the Riemann surface.

Based on the three-dimensional representation, the Riemann surface can be considered as a stack of sheets glued together at the locations of self-intersections. Each sheet naturally corresponds to a single-valued sheet for ω , and the projections of the self-intersection curves on the ω plane are the branch cuts associated with the neighboring sheets. If $\ln |z|$ is used in generating the three-dimensional Riemann surface, then with the ordering $|z_{(1)}| \leq |z_{(2)}| \leq \dots \leq |z_{(p+q)}|$, $z_{(1)}$ will be located on the bottom-most sheet, $z_{(2)}$ on the second-to-bottom sheet, and so on. The OBC spectrum, with $|z_{(p)}| = |z_{(p+1)}|$, would then correspond to the branch cuts between the p th sheet and the $(p + 1)$ th sheet.

APPENDIX B. TOEPLITZ MATRICES

The Hamiltonians of single-band, one-dimensional chains with periodic coupling are characterized by infinite Toeplitz matrices, which have identical elements along the diagonals. The corresponding SIBC and OBC cases are known as Toeplitz matrices and truncated Toeplitz matrices, respectively. Many of the results in the band theory of non-Hermitian systems are known to mathematicians studying Toeplitz matrices under different contexts [43]. We summarize some of the mathematical results here and point out their physical significance.

The *Toeplitz matrix* generated by f , a function defined on the complex unit circle ($|z| = 1$) taking complex values, is the semi-infinite matrix given by

$$T(f) = \begin{bmatrix} t_0 & t_1 & t_2 & \cdots \\ t_{-1} & t_0 & t_1 & \cdots \\ t_{-2} & t_{-1} & t_0 & \cdots \\ \vdots & \vdots & \vdots & \ddots \end{bmatrix}, \quad (\text{B1})$$

where t_m is the Fourier coefficients of f :

$$t_m = \frac{1}{2\pi} \int_0^{2\pi} f(e^{i\theta}) e^{-im\theta} d\theta, \quad \theta \in \mathbb{R}. \quad (\text{B2})$$

The function f is called the *symbol* of the matrix and corresponds to the PBC spectrum. In the following, we only consider the case where f is continuous, as encountered in most physical systems.

The $N \times N$ *truncated Toeplitz matrix* $T_N(f)$ is obtained by taking the first N rows and N columns of $T(f)$. Here $T(f)$ and $T_N(f)$ correspond to the SIBC and OBC Hamiltonian for the system, respectively.

Let X be the space of all physical states defined on the right-extending semi-infinite chain with a converging sum of squared amplitudes. The *kernel* and the *image* of $T(f)$ are defined by

$$\text{Ker } T(f) = \{x \in X : T(f)x = 0\}, \quad \text{Im } T(f) = \{T(f)x : x \in X\}, \quad (\text{B3})$$

Here $T(f)$ is *Fredholm* if $\text{Im } T(f)$ is a closed subspace of X and the two numbers

$$\alpha = \dim \text{Ker } T(f), \quad \beta = \dim \text{Coker } T(f) \quad (\text{B4})$$

are finite, where the *cokernel* of $T(f)$, denoted by $\text{Coker } T(f)$, is the space $X/\text{Im } T(f)$ [i.e., the equivalence classes in X as defined by the relation $x_1 \sim x_2$ if and only if

$x_1 - x_2 \in \text{Im } T(f)$]. In this case, the *index* of $T(f)$ is defined as the integer

$$\text{Ind } T(f) = \dim \text{Ker } T(f) - \dim \text{Coker } T(f). \quad (\text{B5})$$

We are now ready to state the mathematical form of the bulk–boundary correspondence ([43], Theorem 1.17):

We say that $T(f)$ is Fredholm if and only if f has no zeros on $|z| = 1$, in which case

$$\text{Ind } T(f) = w, \quad (\text{B6})$$

where w is the winding number of the curve defined by f with respect to the origin.

The dimension of the kernel corresponds to the number of modes with $\omega = 0$ at the left edge in a semi-infinite chain truncated on the left, since the kernel can be viewed as the collection of modes with zero eigenfrequency. Similarly, by transposing the $T(f)$ matrix, the dimension of the cokernel corresponds to the number of modes at the right edge in a semi-infinite chain truncated on the right. However, by a separate theorem, modes for left-truncated and right-truncated chains cannot exist simultaneously (either $T(f)$ has a trivial kernel or the image of $T(f)$ is dense; see [43]). As such, we were able to show a slightly stronger version of the correspondence in single-band (and possibly non-tight-binding) models where the number of modes on a specific edge is given directly by $|w|$.

The original statement in [43] has $\text{Ind } T(f) = -w$ instead; the sign is different because the Toeplitz matrices there have negative indices on the upper-right diagonals (i.e., transposed compared with our convention). The theorem is itself a special case of the *Atiyah–Singer index theorem* [324], which links the index of certain operators to their topological properties.

For the OBC spectrum, we focus on the *banded Toeplitz matrices*, where $t_m = 0$ for all $|m| \geq p$ for some $p \in \mathbb{N}$. Banded matrices describe tight-binding models, and the corresponding f is a Laurent polynomial in z with a finite number of terms. Let $\text{sp } T_N(f)$ denote the spectrum of $T_N(f)$ (the set of its eigenvalues). The set $\lim_{N \rightarrow \infty} \text{sp } T_N(f)$ consists of the points that are limits of some sequence λ_M where $\lambda_N \in \text{sp } T_N(f)$, and represents the OBC spectrum as $N \rightarrow \infty$.

We have the following theorem regarding the properties of the OBC spectrum [43].

For a Toeplitz banded matrix $T(f)$ and its truncations $T_N(f)$:

- (1) $\lim_{N \rightarrow \infty} \text{sp } T_N(f) = \bigcap_{\lambda > 0} \text{sp } T(f_\lambda)$, where $\text{sp } T(f_\lambda)$, the spectrum of $T(f_\lambda)$, consists of the range of $f_\lambda = f(\lambda e^{i\theta})$ as a function of $\theta \in \mathbb{R}$ as well as regions with a nonzero winding number for the range of f_λ as a curve; the intersection is taken over all positive λ ; this corresponds to the self-intersection construction for the OBC spectrum and explicitly demonstrates its gauge invariance;
- (2) $\lim_{N \rightarrow \infty} \text{sp } T_N(f) = \{\omega \in \mathbb{C} : |z_{(p)}| = |z_{(p+1)}|\}$ where $z_{(m)}$ for each ω is the roots to $z^p f(z) = z^p \omega$ sorted in nondecreasing amplitude; this provides the GBZ construction of the OBC spectrum;
- (3) $\lim_{N \rightarrow \infty} \text{sp } T_N(f)$ is always a finite union of analytic arcs, each pair of which have at most end points in common, and is always connected.

We conclude the discussions of Toeplitz matrices with a theorem characterizing the *density of states* for the OBC spectrum [43].

If there exists a measurable and almost everywhere finite function $\gamma(\omega)$ (from \mathbb{C} to \mathbb{R}) such that, for almost all ω ,

$$\lim_{n \rightarrow \infty} \frac{1}{n} \ln |\det(T_n - \omega \mathbb{I})| = \gamma(\omega), \quad (\text{B7})$$

then $\mu = \Delta\gamma/(2\pi)$ is a measure where Δ is the distributional Laplacian, and

$$\frac{1}{n} \text{tr} \xi(T_n) = \frac{1}{n} \sum_{j=1}^n \xi(\lambda_j) \rightarrow \int_{\mathbb{C}} \xi(\omega) d\mu(\omega) \quad (\text{B8})$$

for every continuous function ξ , where tr is the matrix trace and λ_j is the eigenvalues for T_n . Since the weighted average of any eigenmode properties ξ converges to the average with μ as the weight, μ can be regarded as the limiting density of state of the system when $N \rightarrow \infty$. The density of states as the Laplacian of harmonic functions can be interpreted as a equilibrium problem [59,60] and have lead to electrostatic analogs of the OBC spectra [325]. In particular, for tight-binding models, μ can be formulated as [59,60,326]

$$d\mu = \frac{1}{2\pi i} \sum_{m=1}^p \left(\frac{z'_{(m)+}}{z_{(m)+}} - \frac{z'_{(m)-}}{z_{(m)-}} \right) d\omega, \quad (\text{B9})$$

where $d\omega$ is an oriented line segment on the complex ω plane, $z_{(m)+}$ ($z_{(m)-}$) is the limit of $z_{(m)}$ approaching $d\omega$ from its left (right) side, and a prime indicates derivative with respect to ω . Along a $|z_{(p)}| = |z_{(p+1)}|$ branch cut with $z_{(p+1)} = e^{2i\theta} z_{(p)}$, this simplifies to

$$d\mu = \frac{1}{2\pi i} d\omega \frac{d}{d\omega} \ln \frac{z_{(p+1)}}{z_{(p)}} = \frac{1}{\pi} d\theta. \quad (\text{B10})$$

As such, modes are distributed uniformly in θ , which forms the theoretical basis for Section 7.2.

We note that these discussions are limited to Toeplitz matrices. Many of the results do not carry over to the block Toeplitz matrices representing multiband Hamiltonians. For the bulk–boundary correspondence, the index of $T(f)$ equals w , the winding number of $\det f$ (see [43]). However, it is now possible for both $\dim \text{Ker } T(f)$ and $\dim \text{Coker } T(f)$ to be positive, and we can only conclude that $\dim \text{Ker } T(f) \geq w$. In addition, the second term $\dim \text{Coker } T(f)$ can no longer be interpreted as the number of modes for an left-extending chain, as the transpose of $T(f)$ is generally different from $T[f(z^{-1})]$.

The spectral properties in the single-band case does not generalize directly to the multiband case as there can be exceptions as discussed in Section 6.5c. With some technical restrictions to eliminate such exceptions, the $|z_{(p)}| = |z_{(p+1)}|$ condition can be recovered. Although the OBC spectrum may become disconnected, the total measure of any connected component must be a positive integer. Since the total measure of the spectrum equals to the number of bands r , there can be at most r components. These results have been summarized in [327,328]. As the total measure represents the number of modes for that component averaged over each unit cell, each component contains a integer number of modes per unit cell, and the partition of bands become adequate for the OBC spectrum even for non-Hermitian models.

APPENDIX C. NUMBER OF INDEPENDENT BOUNDARY CONDITIONS FOR MULTIBAND MODELS

During the discussion of SIBC in multiband models (Section 6.4), we need to know the number of independent boundary conditions given a set of coupling coefficients. To this end, we state and prove the following theorem.

Assume that a $r \times r$ matrix $H(z)$ has Laurent polynomials as its entries and can be expressed as

$$H(z) = \sum_{-p \leq m \leq q} T_m z^m, \quad (\text{C1})$$

where p and q are positive integers and T_m are $r \times r$ matrices with complex number entries. Then the rank of the following $rp \times rp$ matrix,

$$T_{\text{left}} = \begin{bmatrix} T_{-p} & T_{-p+1} & \cdots & T_{-2} & T_{-1} \\ 0 & T_{-p} & \cdots & T_{-3} & T_{-2} \\ \vdots & \vdots & \ddots & \vdots & \vdots \\ 0 & 0 & \cdots & T_{-p} & T_{-p+1} \\ 0 & 0 & \cdots & 0 & T_{-p} \end{bmatrix}, \quad (\text{C2})$$

is equal to the negative of the lowest possible degree of z appearing in at least one minor determinant of $H(z)$. In particular, since the characteristic polynomial $\det[H(z) - \omega \mathbb{I}]$ can be expressed using only minor determinants of $H(z)$, it follows that $\text{rank}(T_{\text{left}}) \geq P$, where $-P$ is the lowest degree of z appearing in $\det[H(z) - \omega \mathbb{I}]$.

The proof consists of two parts. We first show that $z^p H(z)$ as a matrix with (ordinary) polynomial entries can be brought to the Smith normal form [329]. This procedure extracts the lowest degree of z in the minors of $H(z)$, and the transformation performed on $H(z)$ can be translated to elementary row and column operations on T_{left} preserving its rank. Then we consider the negative powers of z in the Smith normal form of $H(z)$ and show that they have a one-to-one correspondence to the linear independent rows in T_{left} .

For a matrix $H_{\text{poly}}(z)$ where each entry is an ordinary polynomial of z , there exists square matrices U_L and U_R that has the same size as $H_{\text{poly}}(z)$, has polynomials of z as its entries, and has determinant 1, such that

$$U_L H_{\text{poly}}(z) U_R = \begin{bmatrix} h_1 & 0 & \cdots & 0 & 0 & \cdots & 0 \\ 0 & h_2 & \cdots & 0 & 0 & \cdots & 0 \\ \vdots & \vdots & \ddots & \vdots & \vdots & \vdots & \vdots \\ 0 & 0 & \cdots & h_s & 0 & \cdots & 0 \\ 0 & 0 & \cdots & 0 & 0 & \cdots & 0 \\ \vdots & \vdots & \cdots & \vdots & \vdots & \ddots & \vdots \\ 0 & 0 & \cdots & 0 & 0 & \cdots & 0 \end{bmatrix} \equiv S, \quad (\text{C3})$$

where each entry of S is a polynomial and each h_m divides h_{m+1} (i.e., h_{m+1}/h_m is a polynomial in z) for all $1 \leq m < s$. The diagonal matrix S is termed the Smith normal form of $H_{\text{poly}}(z)$, and is unique up to constant factors for each h_m . The h_m polynomials can be computed as, up to constant factors,

$$h_m = \frac{d_m}{d_{m-1}}, \quad (\text{C4})$$

where $d_0 = 1$ and d_m is the polynomial greatest common divisor of the determinants of all $m \times m$ minors of $H_{\text{poly}}(z)$ with $1 \leq m \leq r$. From the polynomial division properties, the lowest degree of z among all $m \times m$ minor determinants of $H_{\text{poly}}(z)$ equals the lowest degree of z in d_m for each m .

As $z^p H(z)$ cancels the negative powers of z in $H(z)$, we set $H_{\text{poly}}(z) = z^p H(z)$ and arrive at a Smith normal form for $z^p H(z)$ with $U_L z^p H(z) U_R = S$. With the same set of U_L and U_R , we have $U_L H(z) U_R = z^{-p} S$, and with a slight abuse of notation we define $z^{-p} S$ as

the Smith normal form of $H(z)$ with entries $\hat{h}_m \equiv z^{-p} h_m$. We denote the lowest degree of z in \hat{h}_m as $-p_m$. From the properties of the Smith normal form, $p_m \geq p_{m+1}$ for all $1 \leq m < s$, and the lowest degree of z among all $m \times m$ minor determinants of $H(z)$ equals $-\sum_{j=1}^m p_j$.

Since the determinant of U_L does not depend on z , it can be decomposed as the product of finitely many elementary row matrices, each performing an elementary row operation on $H(z)$ (i.e., permuting two rows, multiplying one row by a constant, or adding z^s times one row to another row). The changes to the T_m matrices are equivalent to performing elementary row operations directly on T_{left} . For example, permuting the first two rows is equivalent to swapping the $(rm + 1)$ th row of T_{left} with the $(rm + 2)$ th row of T_{left} for each m from 0 to $p - 1$, and adding z^s times the first row of $H(z)$ to the second row is equivalent to adding the $(rm + 1)$ th row of T_{left} to the $(rm - rs + 2)$ th row for each m from s to $p - 1$. Similarly, U_R performs finitely many elementary column operations on $H(z)$ that can be faithfully translated to T_{left} . As such, the T_{left} corresponding to the Smith normal form of $H(z)$ has the same rank as the original T_{left} .

As the Smith normal form of $H(z)$ is diagonal, it represents a series of decoupled chains, where each chain has a “band structure” given by \hat{h}_m , and we expect that each chain requires p_m boundary conditions if $p_m > 0$ or no boundary conditions if $p_m \leq 0$. To explicitly show this, we consider the collection of $(rm + j)$ th row of T_{left} with j from 1 to s and m from 0 to $p_j - 1$, where the first nonzero element from the left for each row is in the $[rm + r(p - p_j) + j]$ th column and is in a different column for each row. These rows are linearly independent and all other rows are identically zero. As such, the rank can be expressed as

$$\text{rank}(T_{\text{left}}) = \sum_{m=1}^r \max(p_m, 0), \quad (\text{C5})$$

which is exactly the lowest possible value among all $\sum p_m$, and the negative of the minimum degree of z obtainable from $H(z)$ minor determinants of all sizes. As such, the rank of T_{left} equals the lowest possible degree of z in all minor determinants of $H(z)$.

The theorem relating $\text{rank}(T_{\text{left}})$ to the minors of $H(z)$ raises the possibility that $\text{rank}(T_{\text{left}})$ may be larger than P . As an example, consider the following two-band model with next-nearest-neighbor coupling:

$$H(z) = \begin{bmatrix} 0 & z^{-2} \\ z + c & 0 \end{bmatrix}. \quad (\text{C6})$$

The characteristic equation is

$$\omega^2 = cz^{-2} + z^{-1}, \quad (\text{C7})$$

and P may be either 2 ($c \neq 0$) or 1 ($c = 0$). However, the necessary boundary condition remains as 2 due to the z^{-2} element (in this case, $\psi_{B,0} = \psi_{B,-1} = 0$). The discrepancy of P and the number of boundary conditions will lead to problems when counting the available states for superposition and interpreting the winding number as the number of skin modes. To get around this problem, the power of z in the denominator of the characteristic equation should be raised to match the number of boundary conditions before eliminating it, i.e.,

$$z^{-2} (z^2 \omega^2 - z - c) = 0. \quad (\text{C8})$$

This adds a new root $z = 0$ to the polynomial part of the equation when $c = 0$, and we can correctly identify $P = 2$. Although the $z = 0$ solution is spurious for $H(z)$, it is a physically meaningful state in terms of the wave function in the spatial domain when

boundaries are present, corresponding to $\psi_1 \neq 0$ and $\psi_m = 0$ for all $m > 1$ [330]. The state counting can then proceed as normal by including the $z = 0$ state.

FUNDING

Simons Foundation (827065); Air Force Office of Scientific Research (FA9550-22-1-0339).

ACKNOWLEDGMENTS

JZ is grateful to A. Poddubny and Z. Wang for useful discussions.

DISCLOSURES

The authors declare no conflicts of interest.

DATA AVAILABILITY

No data were generated or analyzed in the presented research.

REFERENCES

1. X.-L. Qi and S.-C. Zhang, "Topological insulators and superconductors," *Rev. Mod. Phys.* **83**, 1057–1110 (2011).
2. L. Lu, J. D. Joannopoulos, and M. Soljacic, "Topological photonics," *Nat. Photonics* **8**, 821–829 (2014).
3. T. Ozawa, H. M. Price, A. Amo, *et al.*, "Topological photonics," *Rev. Mod. Phys.* **91**, 015006 (2019).
4. H. Price, Y. Chong, A. Khanikaev, *et al.*, "Roadmap on topological photonics," *J. Phys. Photonics* **4**, 032501 (2022).
5. H. Xue, Y. Yang, and B. Zhang, "Topological acoustics," *Nat. Rev. Mater.* **7**, 974–990 (2022).
6. X. Zhang, F. Zangeneh-Nejad, Z.-G. Chen, *et al.*, "A second wave of topological phenomena in photonics and acoustics," *Nature* **618**, 687–697 (2023).
7. M. S. Rudner and L. S. Levitov, "Topological transition in a non-Hermitian quantum walk," *Phys. Rev. Lett.* **102**, 065703 (2009).
8. Y. C. Hu and T. L. Hughes, "Absence of topological insulator phases in non-Hermitian PT-symmetric Hamiltonians," *Phys. Rev. B* **84**, 153101 (2011).
9. K. Esaki, M. Sato, K. Hasebe, *et al.*, "Edge states and topological phases in non-Hermitian systems," *Phys. Rev. B* **84**, 205128 (2011).
10. S.-D. Liang and G.-Y. Huang, "Topological invariance and global Berry phase in non-Hermitian systems," *Phys. Rev. A* **87**, 012118 (2013).
11. H. Schomerus, "Topologically protected midgap states in complex photonic lattices," *Opt. Lett.* **38**, 1912 (2013).
12. B. Zhu, R. Lü, and S. Chen, "PT symmetry in the non-Hermitian Su-Schrieffer-Heeger model with complex boundary potentials," *Phys. Rev. A* **89**, 062102 (2014).
13. S. Malzard, C. Poli, and H. Schomerus, "Topologically protected defect states in open photonic systems with non-Hermitian charge-conjugation and parity-time symmetry," *Phys. Rev. Lett.* **115**, 200402 (2015).
14. T. E. Lee, "Anomalous edge state in a non-Hermitian lattice," *Phys. Rev. Lett.* **116**, 133903 (2016).
15. D. Leykam, K. Y. Bliokh, C. Huang, *et al.*, "Edge modes, degeneracies, and topological numbers in non-Hermitian systems," *Phys. Rev. Lett.* **118**, 040401 (2017).

16. S. Lieu, “Topological phases in the non-Hermitian Su-Schrieffer-Heeger model,” *Phys. Rev. B* **97**, 045106 (2018).
17. V. M. Martinez Alvarez, J. E. Barrios Vargas, and L. E. F. Foa Torres, “Non-Hermitian robust edge states in one dimension: anomalous localization and eigenspace condensation at exceptional points,” *Phys. Rev. B* **97**, 121401 (2018).
18. Y. Xiong, “Why does bulk boundary correspondence fail in some non-Hermitian topological models,” *J. Phys. Commun.* **2**, 035043 (2018).
19. H. Shen, B. Zhen, and L. Fu, “Topological band theory for non-Hermitian Hamiltonians,” *Phys. Rev. Lett.* **120**, 146402 (2018).
20. C. Yin, H. Jiang, L. Li, *et al.*, “Geometrical meaning of winding number and its characterization of topological phases in one-dimensional chiral non-Hermitian systems,” *Phys. Rev. A* **97**, 052115 (2018).
21. F. K. Kunst, E. Edvardsson, J. C. Budich, *et al.*, “Biorthogonal bulk-boundary correspondence in non-Hermitian systems,” *Phys. Rev. Lett.* **121**, 026808 (2018).
22. S. Yao, F. Song, and Z. Wang, “Non-Hermitian Chern bands,” *Phys. Rev. Lett.* **121**, 136802 (2018).
23. H. Jiang, C. Yang, and S. Chen, “Topological invariants and phase diagrams for one-dimensional two-band non-Hermitian systems without chiral symmetry,” *Phys. Rev. A* **98**, 052116 (2018).
24. V. M. Martinez Alvarez, J. E. Barrios Vargas, M. Berdakin, *et al.*, “Topological states of non-Hermitian systems,” *Eur. Phys. J. Spec. Top.* **227**, 1295–1308 (2018).
25. A. Ghatak and T. Das, “New topological invariants in non-Hermitian systems,” *J. Phys.: Condens. Matter* **31**, 263001 (2019).
26. L. E. F. Foa Torres, “Perspective on topological states of non-Hermitian lattices,” *J. Phys. Mater.* **3**, 014002 (2020).
27. S. Yao and Z. Wang, “Edge states and topological invariants of non-Hermitian systems,” *Phys. Rev. Lett.* **121**, 086803 (2018).
28. X. Zhang, T. Zhang, M.-H. Lu, *et al.*, “A review on non-Hermitian skin effect,” *Adv. Phys.: X* **7**, 2109431 (2022).
29. R. Lin, T. Tai, L. Li, *et al.*, “Topological non-Hermitian skin effect,” *Front. Phys.* **18**, 53605 (2023).
30. Y. Ota, K. Takata, T. Ozawa, *et al.*, “Active topological photonics,” *Nanophotonics* **9**, 547–567 (2020).
31. M. Parto, Y. G. N. Liu, B. Bahari, *et al.*, “Non-Hermitian and topological photonics: optics at an exceptional point,” *Nanophotonics* **10**, 403–423 (2020).
32. H. Wang, X. Zhang, J. Hua, *et al.*, “Topological physics of non-Hermitian optics and photonics: a review,” *J. Opt.* **23**, 123001 (2021).
33. H. Nasari, G. G. Pyrialakos, D. N. Christodoulides, *et al.*, “Non-Hermitian topological photonics,” *Opt. Mater. Express* **13**, 870 (2023).
34. Q. Yan, B. Zhao, R. Zhou, *et al.*, “Advances and applications on non-Hermitian topological photonics,” *Nanophotonics* **12**, 2247–2271 (2023).
35. Q. Wang and Y. D. Chong, “Non-Hermitian photonic lattices: tutorial,” *J. Opt. Soc. Am. B* **40**, 1443 (2023).
36. K. Ding, C. Fang, and G. Ma, “Non-Hermitian topology and exceptional-point geometries,” *Nat. Rev. Phys.* **4**, 745–760 (2022).
37. E. J. Bergholtz, J. C. Budich, and F. K. Kunst, “Exceptional topology of non-Hermitian systems,” *Rev. Mod. Phys.* **93**, 015005 (2021).
38. N. Okuma and M. Sato, “Non-Hermitian topological phenomena: A review,” *Annu. Rev. Condens. Matter Phys.* **14**, 83–107 (2023).
39. A. Banerjee, R. Sarkar, S. Dey, *et al.*, “Non-Hermitian topological phases: principles and prospects,” *J. Phys.: Condens. Matter* **35**, 333001 (2023).

40. Y. Ashida, Z. Gong, and M. Ueda, “Non-Hermitian physics,” *Adv. Phys.* **69**, 249–435 (2020).
41. N. Hatano and D. R. Nelson, “Localization transitions in non-Hermitian quantum mechanics,” *Phys. Rev. Lett.* **77**, 570–573 (1996).
42. W. P. Su, J. R. Schrieffer, and A. J. Heeger, “Solitons in polyacetylene,” *Phys. Rev. Lett.* **42**, 1698–1701 (1979).
43. A. Böttcher and B. Silbermann, *Introduction to Large Truncated Toeplitz Matrices* (Springer, 1999).
44. K. Zhang, Z. Yang, and C. Fang, “Correspondence between winding numbers and skin modes in non-Hermitian systems,” *Phys. Rev. Lett.* **125**, 126402 (2020).
45. Z. Yang, K. Zhang, C. Fang, *et al.*, “Non-Hermitian bulk–boundary correspondence and auxiliary generalized Brillouin zone theory,” *Phys. Rev. Lett.* **125**, 226402 (2020).
46. Y. Fu and Y. Zhang, “Anatomy of open-boundary bulk in multiband non-Hermitian systems,” *Phys. Rev. B* **107**, 115412 (2023).
47. Y.-M. Hu, H.-Y. Wang, Z. Wang, *et al.*, “Geometric origin of non-Bloch PT symmetry breaking,” *Phys. Rev. Lett.* **132**, 050402 (2024).
48. H. Wang, L. Fan, and S. Fan, “One-dimensional non-Hermitian band structures as Riemann surfaces,” *Phys. Rev. A* **110**, 012209 (2024).
49. Z. Gong, Y. Ashida, K. Kawabata, *et al.*, “Topological phases of non-Hermitian systems,” *Phys. Rev. X* **8**, 031079 (2018).
50. K. Kawabata, K. Shiozaki, M. Ueda, *et al.*, “Symmetry and topology in non-Hermitian physics,” *Phys. Rev. X* **9**, 041015 (2019).
51. H. Zhou and J. Y. Lee, “Periodic table for topological bands with non-Hermitian symmetries,” *Phys. Rev. B* **99**, 235112 (2019).
52. N. Okuma, K. Kawabata, K. Shiozaki, *et al.*, “Topological origin of non-Hermitian skin effects,” *Phys. Rev. Lett.* **124**, 086801 (2020).
53. R. A. Horn and C. R. Johnson, *Matrix Analysis* (Cambridge University Press, 1985).
54. D. H. Greene and D. E. Knuth, *Mathematics for the Analysis of Algorithms* (Birkhäuser Boston, 1990).
55. L. Jin and Z. Song, “Bulk-boundary correspondence in a non-Hermitian system in one dimension with chiral inversion symmetry,” *Phys. Rev. B* **99**, 081103 (2019).
56. K. Yokomizo and S. Murakami, “Non-Bloch band theory of non-Hermitian systems,” *Phys. Rev. Lett.* **123**, 066404 (2019).
57. C. H. Lee and R. Thomale, “Anatomy of skin modes and topology in non-Hermitian systems,” *Phys. Rev. B* **99**, 201103 (2019).
58. D. Wu, J. Xie, Y. Zhou, *et al.*, “Connections between the open-boundary spectrum and the generalized Brillouin zone in non-Hermitian systems,” *Phys. Rev. B* **105**, 045422 (2022).
59. M. Duits and A. B. J. Kuijlaars, “An equilibrium problem for the limiting eigenvalue distribution of banded Toeplitz matrices,” *SIAM J. Matrix Anal. Appl.* **30**, 173–196 (2008).
60. S. Delvaux, “Equilibrium problem for the eigenvalues of banded block Toeplitz matrices,” *Mathematische Nachrichten* **285**, 1935–1962 (2012).
61. C. H. Lee, L. Li, R. Thomale, *et al.*, “Unraveling non-Hermitian pumping: emergent spectral singularities and anomalous responses,” *Phys. Rev. B* **102**, 085151 (2020).
62. T. Tai and C. H. Lee, “Zoology of non-Hermitian spectra and their graph topology,” *Phys. Rev. B* **107**, L220301 (2023).

63. H.-G. Zirnstein, G. Refael, and B. Rosenow, “Bulk-boundary correspondence for non-Hermitian Hamiltonians via Green functions,” *Phys. Rev. Lett.* **126**, 216407 (2021).
64. H.-G. Zirnstein and B. Rosenow, “Exponentially growing bulk green functions as signature of nontrivial non-Hermitian winding number in one dimension,” *Phys. Rev. B* **103**, 195157 (2021).
65. F. Roccati, “Non-Hermitian skin effect as an impurity problem,” *Phys. Rev. A* **104**, 022215 (2021).
66. L. Li, S. Mu, C. H. Lee, *et al.*, “Quantized classical response from spectral winding topology,” *Nat. Commun.* **12**, 5294 (2021).
67. L. Mao, T. Deng, and P. Zhang, “Boundary condition independence of non-Hermitian Hamiltonian dynamics,” *Phys. Rev. B* **104**, 125435 (2021).
68. W.-T. Xue, M.-R. Li, Y.-M. Hu, *et al.*, “Simple formulas of directional amplification from non-Bloch band theory,” *Phys. Rev. B* **103**, L241408 (2021).
69. Y.-M. Hu and Z. Wang, “Green’s functions of multiband non-Hermitian systems,” *Phys. Rev. Res.* **5**, 043073 (2023).
70. Q.-B. Zeng, “Non-Hermitian skin effect edge,” *Phys. Rev. B* **106**, 235411 (2022).
71. V. S. Asadchy, M. S. Mirmoosa, A. Díaz-Rubio, *et al.*, “Tutorial on electromagnetic nonreciprocity and its origins,” *Proc. IEEE* **108**, 1684–1727 (2020).
72. R. Koch and J. C. Budich, “Bulk-boundary correspondence in non-Hermitian systems: stability analysis for generalized boundary conditions,” *Eur. Phys. J. D* **74**, 70 (2020).
73. C.-X. Guo, C.-H. Liu, X.-M. Zhao, *et al.*, “Exact solution of non-Hermitian systems with generalized boundary conditions: size-dependent boundary effect and fragility of the skin effect,” *Phys. Rev. Lett.* **127**, 116801 (2021).
74. E. Edvardsson and E. Ardonne, “Sensitivity of non-Hermitian systems,” *Phys. Rev. B* **106**, 115107 (2022).
75. K.-I. Imura and Y. Takane, “Generalized bulk-edge correspondence for non-Hermitian topological systems,” *Phys. Rev. B* **100**, 165430 (2019).
76. C. C. Wojcik, X.-Q. Sun, T. Bzdušek, *et al.*, “Homotopy characterization of non-Hermitian Hamiltonians,” *Phys. Rev. B* **101**, 205417 (2020).
77. H. Hu and E. Zhao, “Knots and non-Hermitian Bloch bands,” *Phys. Rev. Lett.* **126**, 010401 (2021).
78. Z. Li and R. S. K. Mong, “Homotopical characterization of non-Hermitian band structures,” *Phys. Rev. B* **103**, 155129 (2021).
79. C. C. Wojcik, K. Wang, A. Dutt, *et al.*, “Eigenvalue topology of non-Hermitian band structures in two and three dimensions,” *Phys. Rev. B* **106**, L161401 (2022).
80. C.-X. Guo, S. Chen, K. Ding, *et al.*, “Exceptional non-Abelian topology in multiband non-Hermitian systems,” *Phys. Rev. Lett.* **130**, 157201 (2023).
81. L.-J. Lang, Y. Wang, H. Wang, *et al.*, “Effects of non-Hermiticity on Su-Schrieffer-Heeger defect states,” *Phys. Rev. B* **98**, 094307 (2018).
82. R. Chen, C.-Z. Chen, B. Zhou, *et al.*, “Finite-size effects in non-Hermitian topological systems,” *Phys. Rev. B* **99**, 155431 (2019).
83. L. Herviou, J. H. Bardarson, and N. Regnault, “Defining a bulk-edge correspondence for non-Hermitian Hamiltonians via singular-value decomposition,” *Phys. Rev. A* **99**, 052118 (2019).
84. K. Wang, A. Dutt, C. C. Wojcik, *et al.*, “Topological complex-energy braiding of non-Hermitian bands,” *Nature* **598**, 59–64 (2021).
85. Y. S. S. Patil, J. Höller, P. A. Henry, *et al.*, “Measuring the knot of non-Hermitian degeneracies and non-commuting braids,” *Nature* **607**, 271–275 (2022).

86. Y. Yu, L.-W. Yu, W. Zhang, *et al.*, “Experimental unsupervised learning of non-Hermitian knotted phases with solid-state spins,” *npj Quantum Inf* **8**, 116 (2022).
87. W. Tang, K. Ding, and G. Ma, “Experimental realization of non-abelian permutations in a three-state non-Hermitian system,” *Natl. Sci. Rev.* **9**, nwac010 (2022).
88. Q. Zhang, Y. Li, H. Sun, *et al.*, “Observation of acoustic non-Hermitian Bloch braids and associated topological phase transitions,” *Phys. Rev. Lett.* **130**, 017201 (2023).
89. Z. Li, K. Ding, and G. Ma, “Eigenvalue knots and their isotopic equivalence in three-state non-Hermitian systems,” *Phys. Rev. Res.* **5**, 023038 (2023).
90. M.-M. Cao, K. Li, W.-D. Zhao, *et al.*, “Probing complex-energy topology via non-Hermitian absorption spectroscopy in a trapped ion simulator,” *Phys. Rev. Lett.* **130**, 163001 (2023).
91. Q. Zhang, L. Zhao, X. Liu, *et al.*, “Experimental characterization of three-band braid relations in non-Hermitian acoustic lattices,” *Phys. Rev. Res.* **5**, L022050 (2023).
92. K. Kawabata, N. Okuma, and M. Sato, “Non-Bloch band theory of non-Hermitian Hamiltonians in the symplectic class,” *Phys. Rev. B* **101**, 195147 (2020).
93. C. Yuce, “Non-Hermitian anomalous skin effect,” *Phys. Lett. A* **384**, 126094 (2020).
94. W. Zhu, W. X. Teo, L. Li, *et al.*, “Delocalization of topological edge states,” *Phys. Rev. B* **103**, 195414 (2021).
95. J. Cheng, X. Zhang, M.-H. Lu, *et al.*, “Competition between band topology and non-Hermiticity,” *Phys. Rev. B* **105**, 094103 (2022).
96. L. Li, C. H. Lee, S. Mu, *et al.*, “Critical non-Hermitian skin effect,” *Nat. Commun.* **11**, 5491 (2020).
97. S. Mu, L. Zhou, L. Li, *et al.*, “Non-Hermitian pseudo mobility edge in a coupled chain system,” *Phys. Rev. B* **105**, 205402 (2022).
98. L. Li, W. X. Teo, S. Mu, *et al.*, “Direction reversal of non-Hermitian skin effect via coherent coupling,” *Phys. Rev. B* **106**, 085427 (2022).
99. K. Yokomizo and S. Murakami, “Scaling rule for the critical non-Hermitian skin effect,” *Phys. Rev. B* **104**, 165117 (2021).
100. L. Li and C. H. Lee, “Non-Hermitian pseudo-gaps,” *Sci. Bull.* **67**, 685–690 (2022).
101. F. Qin, Y. Ma, R. Shen, *et al.*, “Universal competitive spectral scaling from the critical non-Hermitian skin effect,” *Phys. Rev. B* **107**, 155430 (2023).
102. Y. Yi and Z. Yang, “Non-Hermitian skin modes induced by on-site dissipations and chiral tunneling effect,” *Phys. Rev. Lett.* **125**, 186802 (2020).
103. R. Okugawa, R. Takahashi, and K. Yokomizo, “Non-Hermitian band topology with generalized inversion symmetry,” *Phys. Rev. B* **103**, 205205 (2021).
104. F. K. Kunst and V. Dwivedi, “Non-Hermitian systems and topology: a transfer-matrix perspective,” *Phys. Rev. B* **99**, 245116 (2019).
105. J. Zhong, K. Wang, Y. Park, *et al.*, “Nontrivial point-gap topology and non-Hermitian skin effect in photonic crystals,” *Phys. Rev. B* **104**, 125416 (2021).
106. S. Longhi, “Probing non-Hermitian skin effect and non-Bloch phase transitions,” *Phys. Rev. Res.* **1**, 023013 (2019).
107. H. Wang, “Supplementary code for calculating the open-boundary spectra of non-Hermitian models,” figshare (2024), <https://doi.org/10.6084/m9.figshare.26543518>.
108. I. M. Gelfand, M. M. Kapranov, and A. V. Zelevinsky, *Discriminants, Resultants, and Multidimensional Determinants* (Birkhäuser, 1994).
109. R. M. Beam and R. F. Warming, “The asymptotic spectra of banded Toeplitz and quasi-Toeplitz matrices,” *SIAM J. Sci. Comput.* **14**, 971–1006 (1993).

110. K. Yokomizo, T. Yoda, and S. Murakami, “Non-Hermitian waves in a continuous periodic model and application to photonic crystals,” *Phys. Rev. Res.* **4**, 023089 (2022).
111. M. G. Silveirinha, “Topological theory of non-Hermitian photonic systems,” *Phys. Rev. B* **99**, 125155 (2019).
112. X. Zhu, H. Wang, S. K. Gupta, *et al.*, “Photonic non-Hermitian skin effect and non-Bloch bulk–boundary correspondence,” *Phys. Rev. Res.* **2**, 013280 (2020).
113. Z. Lin, L. Ding, S. Ke, *et al.*, “Steering non-Hermitian skin modes by synthetic gauge fields in optical ring resonators,” *Opt. Lett.* **46**, 3512 (2021).
114. Y. Jin, W. Zhong, R. Cai, *et al.*, “Non-Hermitian skin effect in a phononic beam based on piezoelectric feedback control,” *Appl. Phys. Lett.* **121**, 022202 (2022).
115. H. Xin, W. Song, S. Wu, *et al.*, “Manipulating the non-Hermitian skin effect in optical ring resonators,” *Phys. Rev. B* **107**, 165401 (2023).
116. S. Ke, W. Wen, D. Zhao, *et al.*, “Floquet engineering of the non-Hermitian skin effect in photonic waveguide arrays,” *Phys. Rev. A* **107**, 053508 (2023).
117. H. Liu, P. Lai, H. Wang, *et al.*, “Topological phases and non-Hermitian topology in photonic artificial microstructures,” *Nanophotonics* **12**, 2273–2294 (2023).
118. W. Zhu and J. Gong, “Photonic corner skin modes in non-Hermitian photonic crystals,” *Phys. Rev. B* **108**, 035406 (2023).
119. S. Mandal, R. Banerjee, E. A. Ostrovskaya, *et al.*, “Nonreciprocal transport of exciton polaritons in a non-Hermitian chain,” *Phys. Rev. Lett.* **125**, 123902 (2020).
120. X. Xu, H. Xu, S. Mandal, *et al.*, “Interaction-induced double-sided skin effect in an exciton-polariton system,” *Phys. Rev. B* **103**, 235306 (2021).
121. H. Xu, K. Dini, X. Xu, *et al.*, “Nonreciprocal exciton-polariton ring lattices,” *Phys. Rev. B* **104**, 195301 (2021).
122. S. Mandal, R. Banerjee, and T. C. H. Liew, “From the topological spin-Hall effect to the non-Hermitian skin effect in an elliptical micropillar chain,” *ACS Photonics* **9**, 527–539 (2022).
123. B. Flebus, R. A. Duine, and H. M. Hurst, “Non-Hermitian topology of one-dimensional spin-torque oscillator arrays,” *Phys. Rev. B* **102**, 180408 (2020).
124. T. Yu and B. Zeng, “Giant microwave sensitivity of a magnetic array by long-range chiral interaction driven skin effect,” *Phys. Rev. B* **105**, L180401 (2022).
125. K. Deng and B. Flebus, “Non-Hermitian skin effect in magnetic systems,” *Phys. Rev. B* **105**, L180406 (2022).
126. H. M. Hurst and B. Flebus, “Non-Hermitian physics in magnetic systems,” *J. Appl. Phys.* **132**, 220902 (2022).
127. H. Schomerus, “Nonreciprocal response theory of non-Hermitian mechanical metamaterials: response phase transition from the skin effect of zero modes,” *Phys. Rev. Res.* **2**, 013058 (2020).
128. M. I. N. Rosa and M. Ruzzene, “Dynamics and topology of non-Hermitian elastic lattices with non-local feedback control interactions,” *New J. Phys.* **22**, 053004 (2020).
129. D. Zhou and J. Zhang, “Non-Hermitian topological metamaterials with odd elasticity,” *Phys. Rev. Res.* **2**, 023173 (2020).
130. C. Scheibner, W. T. Irvine, and V. Vitelli, “Non-Hermitian band topology and skin modes in active elastic media,” *Phys. Rev. Lett.* **125**, 118001 (2020).
131. P. Gao, M. Willatzen, and J. Christensen, “Anomalous topological edge states in non-Hermitian piezophononic media,” *Phys. Rev. Lett.* **125**, 206402 (2020).
132. D. Braghini, L. G. G. Villani, M. I. N. Rosa, *et al.*, “Non-Hermitian elastic waveguides with piezoelectric feedback actuation: non-reciprocal bands and skin modes,” *J. Phys. D: Appl. Phys.* **54**, 285302 (2021).

133. S. Shankar, A. Souslov, M. J. Bowick, *et al.*, “Topological active matter,” *Nat. Rev. Phys.* **4**, 380–398 (2022).
134. Z. Gu, H. Gao, P.-C. Cao, *et al.*, “Controlling sound in non-Hermitian acoustic systems,” *Phys. Rev. Appl.* **16**, 057001 (2021).
135. X. Wang, R. Dong, Y. Li, *et al.*, “Non-local and non-Hermitian acoustic metasurfaces,” *Rep. Prog. Phys.* **86**, 116501 (2023).
136. K. Xu, X. Zhang, K. Luo, *et al.*, “Coexistence of topological edge states and skin effects in the non-Hermitian Su-Schrieffer-Heeger model with long-range nonreciprocal hopping in topoelectric realizations,” *Phys. Rev. B* **103**, 125411 (2021).
137. S. M. Rafi-Ul-Islam, Z. B. Siu, H. Sahin, *et al.*, “Unconventional skin modes in generalized topoelectrical circuits with multiple asymmetric couplings,” *Phys. Rev. Res.* **4**, 043108 (2022).
138. L. Li, C. H. Lee, and J. Gong, “Topological switch for non-Hermitian skin effect in cold-atom systems with loss,” *Phys. Rev. Lett.* **124**, 250402 (2020).
139. L. Zhou, H. Li, W. Yi, *et al.*, “Engineering non-Hermitian skin effect with band topology in ultracold gases,” *Commun. Phys.* **5**, 252 (2022).
140. S. Guo, C. Dong, F. Zhang, *et al.*, “Theoretical prediction of a non-Hermitian skin effect in ultracold-atom systems,” *Phys. Rev. A* **106**, L061302 (2022).
141. L. Mao, Y. Hao, and L. Pan, “Non-Hermitian skin effect in a one-dimensional interacting Bose gas,” *Phys. Rev. A* **107**, 043315 (2023).
142. P. Kokhanchik, D. Solnyshkov, and G. Malpuech, “Non-Hermitian skin effect induced by Rashba-Dresselhaus spin-orbit coupling,” *Phys. Rev. B* **108**, L041403 (2023).
143. X.-Q. Sun, P. Zhu, and T. L. Hughes, “Geometric response and disclination-induced skin effects in non-Hermitian systems,” *Phys. Rev. Lett.* **127**, 066401 (2021).
144. F. Schindler and A. Prem, “Dislocation non-Hermitian skin effect,” *Phys. Rev. B* **104**, L161106 (2021).
145. B. A. Bhargava, I. C. Fulga, J. Van Den Brink, *et al.*, “Non-Hermitian skin effect of dislocations and its topological origin,” *Phys. Rev. B* **104**, L241402 (2021).
146. A. Panigrahi, R. Moessner, and B. Roy, “Non-Hermitian dislocation modes: stability and melting across exceptional points,” *Phys. Rev. B* **106**, L041302 (2022).
147. Z.-K. Lin, Q. Wang, Y. Liu, *et al.*, “Topological phenomena at defects in acoustic, photonic and solid-state lattices,” *Nat. Rev. Phys.* **5**, 483–495 (2023).
148. A. McDonald, T. Pereg-Barnea, and A. A. Clerk, “Phase-dependent chiral transport and effective non-Hermitian dynamics in a bosonic Kitaev-Majorana chain,” *Phys. Rev. X* **8**, 041031 (2018).
149. L.-L. Wan and X.-Y. Lü, “Quantum-squeezing-induced point-gap topology and skin effect,” *Phys. Rev. Lett.* **130**, 203605 (2023).
150. P.-C. Cao, Y. Li, Y.-G. Peng, *et al.*, “Diffusive skin effect and topological heat funneling,” *Commun. Phys.* **4**, 230 (2021).
151. P.-C. Cao, Y.-G. Peng, Y. Li, *et al.*, “Phase-locking diffusive skin effect,” *Chin. Phys. Lett.* **39**, 057801 (2022).
152. S. Weidemann, M. Kremer, T. Helbig, *et al.*, “Topological funneling of light,” *Science* **368**, 311–314 (2020).
153. S. Weidemann, M. Kremer, S. Longhi, *et al.*, “Topological triple phase transition in non-Hermitian Floquet quasicrystals,” *Nature* **601**, 354–359 (2022).
154. G.-G. Liu, S. Mandal, P. Zhou, *et al.*, “Localization of chiral edge states by the non-Hermitian skin effect,” *Phys. Rev. Lett.* **132**, 113802 (2024).
155. Y. G. N. Liu, Y. Wei, O. Hemmatyar, *et al.*, “Complex skin modes in non-Hermitian coupled laser arrays,” *Light: Sci. Appl.* **11**, 336 (2022).

156. C. R. Leefmans, M. Parto, J. Williams, *et al.*, “Topological temporally mode-locked laser,” *Nat. Phys.* **20**, 852–858 (2024).
157. K. Wang, A. Dutt, K. Y. Yang, *et al.*, “Generating arbitrary topological windings of a non-Hermitian band,” *Science* **371**, 1240–1245 (2021).
158. Z. Gao, X. Qiao, M. Pan, *et al.*, “Two-dimensional reconfigurable non-Hermitian gauged laser array,” *Phys. Rev. Lett.* **130**, 263801 (2023).
159. Y. Sun, X. Hou, T. Wan, *et al.*, “Photonic Floquet skin-topological effect,” *Phys. Rev. Lett.* **132**, 063804 (2024).
160. T. Helbig, T. Hofmann, S. Imhof, *et al.*, “Generalized bulk–boundary correspondence in non-Hermitian topoelectrical circuits,” *Nat. Phys.* **16**, 747–750 (2020).
161. S. Liu, R. Shao, S. Ma, *et al.*, “Non-Hermitian skin effect in a non-Hermitian electrical circuit,” *Research (Washington, DC)* **2021**, 5608038 (2021).
162. T. Hofmann, T. Helbig, F. Schindler, *et al.*, “Reciprocal skin effect and its realization in a topoelectrical circuit,” *Phys. Rev. Res.* **2**, 023265 (2020).
163. D. Zou, T. Chen, W. He, *et al.*, “Observation of hybrid higher-order skin-topological effect in non-Hermitian topoelectrical circuits,” *Nat. Commun.* **12**, 7201 (2021).
164. C. Shang, S. Liu, R. Shao, *et al.*, “Experimental identification of the second-order non-Hermitian skin effect with physics-graph-informed machine learning,” *Adv. Sci.* **9**, 2202922 (2022).
165. W. Zhang, F. Di, H. Yuan, *et al.*, “Observation of non-Hermitian aggregation effects induced by strong interactions,” *Phys. Rev. B* **105**, 195131 (2022).
166. H. Zhang, T. Chen, L. Li, *et al.*, “Electrical circuit realization of topological switching for the non-Hermitian skin effect,” *Phys. Rev. B* **107**, 085426 (2023).
167. H. Yuan, W. Zhang, Z. Zhou, *et al.*, “Non-Hermitian topoelectrical circuit sensor with high sensitivity,” *Adv. Sci.* **10**, 2301128 (2023).
168. P. Zhu, X.-Q. Sun, T. L. Hughes, *et al.*, “Higher rank chirality and non-Hermitian skin effect in a topoelectrical circuit,” *Nat. Commun.* **14**, 720 (2023).
169. A. Wang, Z. Meng, and C. Q. Chen, “Non-Hermitian topology in static mechanical metamaterials,” *Sci. Adv.* **9**, eadf7299 (2023).
170. A. Ghatak, M. Brandenbourger, J. Van Wezel, *et al.*, “Observation of non-Hermitian topology and its bulk-edge correspondence in an active mechanical metamaterial,” *Proc. Natl. Acad. Sci.* **117**, 29561–29568 (2020).
171. Q. Wu, X. Xu, H. Qian, *et al.*, “Active metamaterials for realizing odd mass density,” *Proc. Natl. Acad. Sci.* **120**, e2209829120 (2023).
172. M. Brandenbourger, X. Locsin, E. Lerner, *et al.*, “Non-reciprocal robotic metamaterials,” *Nat. Commun.* **10**, 4608 (2019).
173. Y. Chen, X. Li, C. Scheibner, *et al.*, “Realization of active metamaterials with odd micropolar elasticity,” *Nat. Commun.* **12**, 5935 (2021).
174. J. J. Slim, C. C. Wanjura, M. Brunelli, *et al.*, “Optomechanical realization of the bosonic Kitaev chain,” *Nature* **627**, 767–771 (2024).
175. L. S. Palacios, S. Tchoumakov, M. Guix, *et al.*, “Guided accumulation of active particles by topological design of a second-order skin effect,” *Nat. Commun.* **12**, 4691 (2021).
176. W. Wang, X. Wang, and G. Ma, “Extended state in a localized continuum,” *Phys. Rev. Lett.* **129**, 264301 (2022).
177. H. Gao, H. Xue, Z. Gu, *et al.*, “Anomalous Floquet non-Hermitian skin effect in a ring resonator lattice,” *Phys. Rev. B* **106**, 134112 (2022).
178. L. Zhang, Y. Yang, Y. Ge, *et al.*, “Acoustic non-Hermitian skin effect from twisted winding topology,” *Nat. Commun.* **12**, 6297 (2021).
179. Z. Gu, H. Gao, H. Xue, *et al.*, “Transient non-Hermitian skin effect,” *Nat. Commun.* **13**, 7668 (2022).

180. X. Zhang, Y. Tian, J.-H. Jiang, *et al.*, “Observation of higher-order non-Hermitian skin effect,” *Nat. Commun.* **12**, 5377 (2021).
181. T. Wan, K. Zhang, J. Li, *et al.*, “Observation of the geometry-dependent skin effect and dynamical degeneracy splitting,” *Sci. Bull.* **68**, 2330–2335 (2023).
182. Q. Zhou, J. Wu, Z. Pu, *et al.*, “Observation of geometry-dependent skin effect in non-Hermitian phononic crystals with exceptional points,” *Nat. Commun.* **14**, 4569 (2023).
183. L. Xiao, T. Deng, K. Wang, *et al.*, “Non-Hermitian bulk–boundary correspondence in quantum dynamics,” *Nat. Phys.* **16**, 761–766 (2020).
184. L. Xiao, T. Deng, K. Wang, *et al.*, “Observation of non-Bloch parity-time symmetry and exceptional points,” *Phys. Rev. Lett.* **126**, 230402 (2021).
185. K. Wang, T. Li, L. Xiao, *et al.*, “Detecting non-Bloch topological invariants in quantum dynamics,” *Phys. Rev. Lett.* **127**, 270602 (2021).
186. Q. Liang, D. Xie, Z. Dong, *et al.*, “Dynamic signatures of non-Hermitian skin effect and topology in ultracold atoms,” *Phys. Rev. Lett.* **129**, 070401 (2022).
187. J. H. Busnaina, Z. Shi, A. McDonald, *et al.*, “Quantum simulation of the bosonic Kitaev chain,” *Nat. Commun.* **15**, 3065 (2024).
188. K. Ochkan, R. Chaturvedi, V. Könye, *et al.*, “Non-Hermitian topology in a multi-terminal quantum Hall device,” *Nat. Phys.* **20**, 395–401 (2024).
189. Y.-K. Liu, P.-C. Cao, M. Qi, *et al.*, “Observation of non-Hermitian skin effect in thermal diffusion,” *Sci. Bull.* **69**, 1228–1236 (2024).
190. W. Wang, M. Hu, X. Wang, *et al.*, “Experimental realization of geometry-dependent skin effect in a reciprocal two-dimensional lattice,” *Phys. Rev. Lett.* **131**, 207201 (2023).
191. W. Wang, X. Wang, and G. Ma, “Non-Hermitian morphing of topological modes,” *Nature* **608**, 50–55 (2022).
192. K. Yokomizo and S. Murakami, “Non-Bloch band theory in bosonic Bogoliubov-De Gennes systems,” *Phys. Rev. B* **103**, 165123 (2021).
193. J. C. Budich and E. J. Bergholtz, “Non-Hermitian topological sensors,” *Phys. Rev. Lett.* **125**, 180403 (2020).
194. A. McDonald and A. A. Clerk, “Exponentially-enhanced quantum sensing with non-Hermitian lattice dynamics,” *Nat. Commun.* **11**, 5382 (2020).
195. L. Bao, B. Qi, and D. Dong, “Exponentially enhanced quantum non-Hermitian sensing via optimized coherent drive,” *Phys. Rev. Appl.* **17**, 014034 (2022).
196. W. Ding, X. Wang, and S. Chen, “Fundamental sensitivity limits for non-Hermitian quantum sensors,” *Phys. Rev. Lett.* **131**, 160801 (2023).
197. C. Ehrhardt and J. Larson, “Exploring the impact of fluctuation-induced criticality on non-Hermitian skin effect and quantum sensors,” *Phys. Rev. Res.* **6**, 023135 (2024).
198. B. Zhu, Q. Wang, D. Leykam, *et al.*, “Anomalous single-mode lasing induced by nonlinearity and the non-Hermitian skin effect,” *Phys. Rev. Lett.* **129**, 013903 (2022).
199. T. Ramos, J. J. García-Ripoll, and D. Porras, “Topological input-output theory for directional amplification,” *Phys. Rev. A* **103**, 033513 (2021).
200. Q. Wang, C. Zhu, Y. Wang, *et al.*, “Amplification of quantum signals by the non-Hermitian skin effect,” *Phys. Rev. B* **106**, 024301 (2022).
201. H. Xu, U. Delic, G. Wang, *et al.*, “Exponentially enhanced non-Hermitian cooling,” *Phys. Rev. Lett.* **132**, 110402 (2024).
202. E. Edvardsson, F. K. Kunst, and E. J. Bergholtz, “Non-Hermitian extensions of higher-order topological phases and their biorthogonal bulk–boundary correspondence,” *Phys. Rev. B* **99**, 081302 (2019).
203. D. S. Borgnia, A. J. Kruchkov, and R.-J. Slager, “Non-Hermitian boundary modes and topology,” *Phys. Rev. Lett.* **124**, 056802 (2020).

204. T. Yoshida, T. Mizoguchi, and Y. Hatsugai, “Mirror skin effect and its electric circuit simulation,” *Phys. Rev. Res.* **2**, 022062 (2020).
205. N. Okuma and M. Sato, “Quantum anomaly, non-Hermitian skin effects, and entanglement entropy in open systems,” *Phys. Rev. B* **103**, 085428 (2021).
206. T. Li, Y.-S. Zhang, and W. Yi, “Two-dimensional quantum walk with non-Hermitian skin effects,” *Chin. Phys. Lett.* **38**, 030301 (2021).
207. M. Lu, X.-X. Zhang, and M. Franz, “Magnetic suppression of non-Hermitian skin effects,” *Phys. Rev. Lett.* **127**, 256402 (2021).
208. Y.-X. Xiao and C. T. Chan, “Topology in non-Hermitian Chern insulators with skin effect,” *Phys. Rev. B* **105**, 075128 (2022).
209. Y.-C. Wang, J.-S. You, and H. H. Jen, “A non-Hermitian optical atomic mirror,” *Nat. Commun.* **13**, 4598 (2022).
210. K. Zhang, Z. Yang, and C. Fang, “Universal non-Hermitian skin effect in two and higher dimensions,” *Nat. Commun.* **13**, 2496 (2022).
211. Z. Fang, M. Hu, L. Zhou, *et al.*, “Geometry-dependent skin effects in reciprocal photonic crystals,” *Nanophotonics* **11**, 3447–3456 (2022).
212. Y. Qin, K. Zhang, and L. Li, “Geometry-dependent skin effect and anisotropic Bloch oscillations in a non-Hermitian optical lattice,” *Phys. Rev. A* **109**, 023317 (2024).
213. T. Liu, Y.-R. Zhang, Q. Ai, *et al.*, “Second-order topological phases in non-Hermitian systems,” *Phys. Rev. Lett.* **122**, 076801 (2019).
214. M. Ezawa, “Non-Hermitian higher-order topological states in nonreciprocal and reciprocal systems with their electric-circuit realization,” *Phys. Rev. B* **99**, 201411 (2019).
215. C. H. Lee, L. Li, and J. Gong, “Hybrid higher-order skin-topological modes in nonreciprocal systems,” *Phys. Rev. Lett.* **123**, 016805 (2019).
216. X.-W. Luo and C. Zhang, “Higher-order topological corner states induced by gain and loss,” *Phys. Rev. Lett.* **123**, 073601 (2019).
217. K. Kawabata, M. Sato, and K. Shiozaki, “Higher-order non-Hermitian skin effect,” *Phys. Rev. B* **102**, 205118 (2020).
218. R. Okugawa, R. Takahashi, and K. Yokomizo, “Second-order topological non-Hermitian skin effects,” *Phys. Rev. B* **102**, 241202 (2020).
219. Y. Fu, J. Hu, and S. Wan, “Non-Hermitian second-order skin and topological modes,” *Phys. Rev. B* **103**, 045420 (2021).
220. Y. Li, C. Liang, C. Wang, *et al.*, “Gain-loss-induced hybrid skin-topological effect,” *Phys. Rev. Lett.* **128**, 223903 (2022).
221. W. Zhu and J. Gong, “Hybrid skin-topological modes without asymmetric couplings,” *Phys. Rev. B* **106**, 035425 (2022).
222. A. K. Ghosh and T. Nag, “Non-Hermitian higher-order topological superconductors in two dimensions: statics and dynamics,” *Phys. Rev. B* **106**, L140303 (2022).
223. Z. Ou, Y. Wang, and L. Li, “Non-Hermitian boundary spectral winding,” *Phys. Rev. B* **107**, L161404 (2023).
224. J. Sun, C.-A. Li, S. Feng, *et al.*, “Hybrid higher-order skin-topological effect in hyperbolic lattices,” *Phys. Rev. B* **108**, 075122 (2023).
225. C.-A. Li, B. Trauzettel, T. Neupert, *et al.*, “Enhancement of second-order non-Hermitian skin effect by magnetic fields,” *Phys. Rev. Lett.* **131**, 116601 (2023).
226. K. Yokomizo and S. Murakami, “Non-Bloch bands in two-dimensional non-Hermitian systems,” *Phys. Rev. B* **107**, 195112 (2023).
227. H. Jiang and C. H. Lee, “Dimensional transmutation from non-Hermiticity,” *Phys. Rev. Lett.* **131**, 076401 (2023).
228. F. Schindler, K. Gu, B. Lian, *et al.*, “Hermitian bulk-non-Hermitian boundary correspondence,” *PRX Quantum* **4**, 030315 (2023).

229. H.-Y. Wang, F. Song, and Z. Wang, “Amoeba formulation of non-Bloch band theory in arbitrary dimensions,” *Phys. Rev. X* **14**, 021011 (2024).
230. N. Okuma and M. Sato, “Hermitian zero modes protected by nonnormality: application of pseudospectra,” *Phys. Rev. B* **102**, 014203 (2020).
231. Y. O. Nakai, N. Okuma, D. Nakamura, *et al.*, “Topological enhancement of nonnormality in non-Hermitian skin effects,” *Phys. Rev. B* **109**, 144203 (2024).
232. S. Franca, V. Könye, F. Hassler, *et al.*, “Non-Hermitian physics without gain or loss: the skin effect of reflected waves,” *Phys. Rev. Lett.* **129**, 086601 (2022).
233. C. C. Wanjura, M. Brunelli, and A. Nunnenkamp, “Correspondence between non-Hermitian topology and directional amplification in the presence of disorder,” *Phys. Rev. Lett.* **127**, 213601 (2021).
234. C. Guo, J. Li, M. Xiao, *et al.*, “Singular topology of scattering matrices,” *Phys. Rev. B* **108**, 155418 (2023).
235. F. Song, S. Yao, and Z. Wang, “Non-Hermitian topological invariants in real space,” *Phys. Rev. Lett.* **123**, 246801 (2019).
236. X.-R. Wang, C.-X. Guo, and S.-P. Kou, “Defective edge states and number-anomalous bulk-boundary correspondence in non-Hermitian topological systems,” *Phys. Rev. B* **101**, 121116 (2020).
237. B. Zhu, Y. Ke, H. Zhong, *et al.*, “Dynamic winding number for exploring band topology,” *Phys. Rev. Res.* **2**, 023043 (2020).
238. T. Fukui and N. Kawakami, “Breakdown of the Mott insulator: exact solution of an asymmetric Hubbard model,” *Phys. Rev. B* **58**, 16051–16056 (1998).
239. J. Feinberg and A. Zee, “Non-Hermitian localization and delocalization,” *Phys. Rev. E* **59**, 6433–6443 (1999).
240. A. V. Kolesnikov and K. B. Efetov, “Localization-delocalization transition in non-Hermitian disordered systems,” *Phys. Rev. Lett.* **84**, 5600–5603 (2000).
241. S. Heußen, C. D. White, and G. Refael, “Extracting many-body localization lengths with an imaginary vector potential,” *Phys. Rev. B* **103**, 064201 (2021).
242. A. Melkani, A. Patapoff, and J. Paulose, “Delocalization of interacting directed polymers on a periodic substrate: localization length and critical exponents from non-Hermitian spectra,” *Phys. Rev. E* **107**, 014501 (2023).
243. S. Longhi, “Non-Bloch-band collapse and chiral Zener tunneling,” *Phys. Rev. Lett.* **124**, 066602 (2020).
244. T. Li, J.-Z. Sun, Y.-S. Zhang, *et al.*, “Non-Bloch quench dynamics,” *Phys. Rev. Res.* **3**, 023022 (2021).
245. W.-T. Xue, Y.-M. Hu, F. Song, *et al.*, “Non-Hermitian edge burst,” *Phys. Rev. Lett.* **128**, 120401 (2022).
246. S. Longhi, “Non-Hermitian skin effect and self-acceleration,” *Phys. Rev. B* **105**, 245143 (2022).
247. H. Li and S. Wan, “Dynamic skin effects in non-Hermitian systems,” *Phys. Rev. B* **106**, L241112 (2022).
248. H. Liu and I. C. Fulga, “Mixed higher-order topology: boundary non-Hermitian skin effect induced by a Floquet bulk,” *Phys. Rev. B* **108**, 035107 (2023).
249. X. Ji and X. Yang, “Generalized bulk–boundary correspondence in periodically driven non-Hermitian systems,” *J. Phys.: Condens. Matter* **36**, 243001 (2024).
250. F. Song, S. Yao, and Z. Wang, “Non-Hermitian skin effect and chiral damping in open quantum systems,” *Phys. Rev. Lett.* **123**, 170401 (2019).
251. S. Longhi, “Unraveling the non-Hermitian skin effect in dissipative systems,” *Phys. Rev. B* **102**, 201103 (2020).
252. T. Haga, M. Nakagawa, R. Hamazaki, *et al.*, “Liouvillian skin effect: slowing down of relaxation processes without gap closing,” *Phys. Rev. Lett.* **127**, 070402 (2021).

253. F. Yang, Q.-D. Jiang, and E. J. Bergholtz, “Liouvillian skin effect in an exactly solvable model,” *Phys. Rev. Res.* **4**, 023160 (2022).
254. J.-S. Pan, L. Li, and J. Gong, “Point-gap topology with complete bulk-boundary correspondence and anomalous amplification in the Fock space of dissipative quantum systems,” *Phys. Rev. B* **103**, 205425 (2021).
255. K. Kawabata, T. Numasawa, and S. Ryu, “Entanglement phase transition induced by the non-Hermitian skin effect,” *Phys. Rev. X* **13**, 021007 (2023).
256. L. Zhou, “Entanglement phase transitions in non-Hermitian Floquet systems,” *Phys. Rev. Res.* **6**, 023081 (2024).
257. Y. Peng, J. Jie, D. Yu, *et al.*, “Manipulating the non-Hermitian skin effect via electric fields,” *Phys. Rev. B* **106**, L161402 (2022).
258. C. Yuce, “Nonlinear non-Hermitian skin effect,” *Phys. Lett. A* **408**, 127484 (2021).
259. M. Ezawa, “Dynamical nonlinear higher-order non-Hermitian skin effects and topological trap-skin phase,” *Phys. Rev. B* **105**, 125421 (2022).
260. Z.-X. Zhang, J. Cao, J.-Q. Li, *et al.*, “Topological skin modes and intensity amplification in a nonlinear non-Hermitian lattice,” *Phys. Rev. B* **108**, 125402 (2023).
261. L.-J. Lang, S.-L. Zhu, and Y. D. Chong, “Non-Hermitian topological end breathers,” *Phys. Rev. B* **104**, L020303 (2021).
262. I. Komis, Z. H. Musslimani, and K. G. Makris, “Skin solitons,” *Opt. Lett.* **48**, 6525–6528 (2023).
263. E. Lee, H. Lee, and B.-J. Yang, “Many-body approach to non-Hermitian physics in fermionic systems,” *Phys. Rev. B* **101**, 121109 (2020).
264. D.-W. Zhang, Y.-L. Chen, G.-Q. Zhang, *et al.*, “Skin superfluid, topological Mott insulators, and asymmetric dynamics in an interacting non-Hermitian Aubry-André-Harper model,” *Phys. Rev. B* **101**, 235150 (2020).
265. T. Liu, J. J. He, T. Yoshida, *et al.*, “Non-Hermitian topological Mott insulators in one-dimensional Fermionic superlattices,” *Phys. Rev. B* **102**, 235151 (2020).
266. C. H. Lee, “Many-body topological and skin states without open boundaries,” *Phys. Rev. B* **104**, 195102 (2021).
267. K. Kawabata, K. Shiozaki, and S. Ryu, “Many-body topology of non-Hermitian systems,” *Phys. Rev. B* **105**, 165137 (2022).
268. M. Žnidarič, “Solvable non-Hermitian skin effect in many-body unitary dynamics,” *Phys. Rev. Res.* **4**, 033041 (2022).
269. F. Alsallom, L. Herviou, O. V. Yazyev, *et al.*, “Fate of the non-Hermitian skin effect in many-body Fermionic systems,” *Phys. Rev. Res.* **4**, 033122 (2022).
270. K. Suthar, Y.-C. Wang, Y.-P. Huang, *et al.*, “Non-Hermitian many-body localization with open boundaries,” *Phys. Rev. B* **106**, 064208 (2022).
271. S.-B. Zhang, M. M. Denner, T. Bzdušek, *et al.*, “Symmetry breaking and spectral structure of the interacting Hatano–Nelson model,” *Phys. Rev. B* **106**, L121102 (2022).
272. R. Shen and C. H. Lee, “Non-Hermitian skin clusters from strong interactions,” *Commun. Phys.* **5**, 238 (2022).
273. T. Yoshida and Y. Hatsugai, “Reduction of one-dimensional non-Hermitian point-gap topology by interactions,” *Phys. Rev. B* **106**, 205147 (2022).
274. Y.-C. Wang, K. Suthar, H. H. Jen, *et al.*, “Non-Hermitian skin effects on thermal and many-body localized phases,” *Phys. Rev. B* **107**, L220205 (2023).
275. H. Li, H. Wu, W. Zheng, *et al.*, “Many-body non-Hermitian skin effect under dynamic gauge coupling,” *Phys. Rev. Res.* **5**, 033173 (2023).
276. S. Hamanaka, K. Yamamoto, and T. Yoshida, “Interaction-induced Liouvillian skin effect in a Fermionic chain with a two-body loss,” *Phys. Rev. B* **108**, 155114 (2023).

277. K. Cao, Q. Du, and S.-P. Kou, "Many-body non-Hermitian skin effect at finite temperatures," *Phys. Rev. B* **108**, 165420 (2023).
278. A. N. Poddubny, "Interaction-induced analog of a non-Hermitian skin effect in a lattice two-body problem," *Phys. Rev. B* **107**, 045131 (2023).
279. S. Longhi, "Non-Hermitian skin effect beyond the tight-binding models," *Phys. Rev. B* **104**, 125109 (2021).
280. B. Zeng and T. Yu, "Radiation-free and non-Hermitian topology inertial defect states of on-chip magnons," *Phys. Rev. Res.* **5**, 013003 (2023).
281. A. Poddubny, J. Zhong, and S. Fan, "Mesoscopic non-Hermitian skin effect," *Phys. Rev. A* **109**, L061501 (2024).
282. K. Kawabata, K. Shiozaki, and S. Ryu, "Topological field theory of non-Hermitian systems," *Phys. Rev. Lett.* **126**, 216405 (2021).
283. K. M. Day, "Toeplitz matrices generated by the Laurent series expansion of an arbitrary rational function," *Trans. Amer. Math. Soc.* **206**, 224 (1975).
284. M. Ezawa, "Non-Hermitian boundary and interface states in nonreciprocal higher-order topological metals and electrical circuits," *Phys. Rev. B* **99**, 121411 (2019).
285. T.-S. Deng and W. Yi, "Non-Bloch topological invariants in a non-Hermitian domain wall system," *Phys. Rev. B* **100**, 035102 (2019).
286. L. Li, C. H. Lee, and J. Gong, "Impurity induced scale-free localization," *Commun. Phys.* **4**, 42 (2021).
287. Y. Liu, Y. Zeng, L. Li, *et al.*, "Exact solution of the single impurity problem in nonreciprocal lattices: impurity-induced size-dependent non-Hermitian skin effect," *Phys. Rev. B* **104**, 085401 (2021).
288. S. Longhi, "Self-healing of non-Hermitian topological skin modes," *Phys. Rev. Lett.* **128**, 157601 (2022).
289. H. Geng, J. Y. Wei, M. H. Zou, *et al.*, "Nonreciprocal charge and spin transport induced by non-Hermitian skin effect in mesoscopic heterojunctions," *Phys. Rev. B* **107**, 035306 (2023).
290. C.-X. Guo, X. Wang, H. Hu, *et al.*, "Accumulation of scale-free localized states induced by local non-Hermiticity," *Phys. Rev. B* **107**, 134121 (2023).
291. B. Li, H.-R. Wang, F. Song, *et al.*, "Scale-free localization and PT symmetry breaking from local non-Hermiticity," *Phys. Rev. B* **108**, L161409 (2023).
292. S. Longhi, "Topological phase transition in non-Hermitian quasicrystals," *Phys. Rev. Lett.* **122**, 237601 (2019).
293. H. Jiang, L.-J. Lang, C. Yang, *et al.*, "Interplay of non-Hermitian skin effects and Anderson localization in nonreciprocal quasiperiodic lattices," *Phys. Rev. B* **100**, 054301 (2019).
294. Q.-B. Zeng, Y.-B. Yang, and Y. Xu, "Topological phases in non-Hermitian Aubry-André-Harper models," *Phys. Rev. B* **101**, 020201 (2020).
295. Q.-B. Zeng, Y.-B. Yang, and R. Lü, "Topological phases in one-dimensional nonreciprocal superlattices," *Phys. Rev. B* **101**, 125418 (2020).
296. Y. Liu, X.-P. Jiang, J. Cao, *et al.*, "Non-Hermitian mobility edges in one-dimensional quasicrystals with parity-time symmetry," *Phys. Rev. B* **101**, 174205 (2020).
297. Q.-B. Zeng and Y. Xu, "Winding numbers and generalized mobility edges in non-Hermitian systems," *Phys. Rev. Res.* **2**, 033052 (2020).
298. T. Liu, H. Guo, Y. Pu, *et al.*, "Generalized Aubry-André self-duality and mobility edges in non-Hermitian quasiperiodic lattices," *Phys. Rev. B* **102**, 024205 (2020).
299. X. Cai, "Boundary-dependent self-dualities, winding numbers, and asymmetrical localization in non-Hermitian aperiodic one-dimensional models," *Phys. Rev. B* **103**, 014201 (2021).

300. Y. Liu, Y. Wang, X.-J. Liu, *et al.*, “Exact mobility edges, PT-symmetry breaking, and skin effect in one-dimensional non-Hermitian quasicrystals,” *Phys. Rev. B* **103**, 014203 (2021).
301. Y. Liu, Y. Wang, Z. Zheng, *et al.*, “Exact non-Hermitian mobility edges in one-dimensional quasicrystal lattice with exponentially decaying hopping and its dual lattice,” *Phys. Rev. B* **103**, 134208 (2021).
302. Y. Liu, Q. Zhou, and S. Chen, “Localization transition, spectrum structure, and winding numbers for one-dimensional non-Hermitian quasicrystals,” *Phys. Rev. B* **104**, 024201 (2021).
303. L.-J. Zhai, G.-Y. Huang, and S. Yin, “Cascade of the delocalization transition in a non-Hermitian interpolating Aubry-André-Fibonacci chain,” *Phys. Rev. B* **104**, 014202 (2021).
304. Q.-B. Zeng and R. Lü, “Real spectra and phase transition of skin effect in nonreciprocal systems,” *Phys. Rev. B* **105**, 245407 (2022).
305. Q. Lin, T. Li, L. Xiao, *et al.*, “Topological phase transitions and mobility edges in non-Hermitian quasicrystals,” *Phys. Rev. Lett.* **129**, 113601 (2022).
306. X. Cai, “Localization transitions and winding numbers for non-Hermitian Aubry-André-Harper models with off-diagonal modulations,” *Phys. Rev. B* **106**, 214207 (2022).
307. S. Manna and B. Roy, “Inner skin effects on non-Hermitian topological fractals,” *Commun. Phys.* **6**, 10 (2023).
308. S. Longhi, “Stochastic non-Hermitian skin effect,” *Opt. Lett.* **45**, 5250 (2020).
309. J. Claes and T. L. Hughes, “Skin effect and winding number in disordered non-Hermitian systems,” *Phys. Rev. B* **103**, L140201 (2021).
310. S. Longhi, “Spectral deformations in non-Hermitian lattices with disorder and skin effect: a solvable model,” *Phys. Rev. B* **103**, 144202 (2021).
311. N. Okuma and M. Sato, “Non-Hermitian skin effects in Hermitian correlated or disordered systems: quantities sensitive or insensitive to boundary effects and pseudo-quantum-number,” *Phys. Rev. Lett.* **126**, 176601 (2021).
312. K.-M. Kim and M. J. Park, “Disorder-driven phase transition in the second-order non-Hermitian skin effect,” *Phys. Rev. B* **104**, L121101 (2021).
313. R. Sarkar, S. S. Hegde, and A. Narayan, “Interplay of disorder and point-gap topology: chiral modes, localization, and non-Hermitian Anderson skin effect in one dimension,” *Phys. Rev. B* **106**, 014207 (2022).
314. Z.-Q. Zhang, H. Liu, H. Liu, *et al.*, “Bulk-boundary correspondence in disordered non-Hermitian systems,” *Sci. Bull.* **68**, 157–164 (2023).
315. P. Mognini, O. Arandes, and E. J. Bergholtz, “Anomalous skin effects in disordered systems with a single non-Hermitian impurity,” *Phys. Rev. Res.* **5**, 033058 (2023).
316. T. Yoshida, T. Mizoguchi, and Y. Hatsugai, “Non-Hermitian topology in rock–paper–scissors games,” *Sci. Rep.* **12**, 560 (2022).
317. C. Lv, R. Zhang, Z. Zhai, *et al.*, “Curving the space by non-Hermiticity,” *Nat. Commun.* **13**, 2184 (2022).
318. A. Amir, N. Hatano, and D. R. Nelson, “Non-Hermitian localization in biological networks,” *Phys. Rev. E* **93**, 042310 (2016).
319. F. L. Metz and I. Neri, “Localization and universality of eigenvectors in directed random graphs,” *Phys. Rev. Lett.* **126**, 040604 (2021).
320. H. Tanaka and D. R. Nelson, “Non-Hermitian quasilocalization and ring attractor neural networks,” *Phys. Rev. E* **99**, 062406 (2019).
321. Z. Jiang, Z. Chen, T. Hou, *et al.*, “Spectrum of non-Hermitian deep-Hebbian neural networks,” *Phys. Rev. Res.* **5**, 013090 (2023).
322. A. Banerjee, R. Jaiswal, M. Manjunath, *et al.*, “A tropical geometric approach to exceptional points,” *Proc. Natl. Acad. Sci.* **120**, e2302572120 (2023).

323. K. Yokomizo, T. Yoda, and Y. Ashida, “Non-Bloch band theory of generalized eigenvalue problems,” *Phys. Rev. B* **109**, 115115 (2024).
324. M. Nakahara, *Geometry, Topology and Physics* (Taylor & Francis, 2003).
325. R. Yang, J. W. Tan, T. Tai, *et al.*, “Designing non-Hermitian real spectra through electrostatics,” *Sci. Bull.* **67**, 1865–1873 (2022).
326. I. I. Hirschman, “The spectra of certain Toeplitz matrices,” *Illinois J. Math.* **11**, 145 (1967).
327. H. Widom, “Asymptotic behavior of block Toeplitz matrices and determinants,” *Adv. Math.* **13**, 284–322 (1974).
328. H. Widom, “Asymptotic behavior of block Toeplitz matrices and determinants. II,” *Adv. Math.* **21**, 1–29 (1976).
329. M. Newman, *Integral Matrices* (Academic Press, 1972).
330. Y. Fu and S. Wan, “Degeneracy and defectiveness in non-Hermitian systems with open boundary,” *Phys. Rev. B* **105**, 075420 (2022).



Heming Wang is a post-doctoral researcher in the Department of Electrical Engineering and Edward L. Ginzton Laboratory at Stanford University. He received his BS in Physics from Peking University, China, in 2016 and PhD in Applied Physics from California Institute of Technology (Caltech) in 2021. He is a gold medalist at the 13th Asian Physics Olympiad (2012). He has co-authored over 40 journal articles in optics and photonics. His current research is focused on non-Hermitian physics, including spectral and topological properties of non-Hermitian systems.



Janet Zhong is a PhD student in Applied Physics at Stanford University. She received her Bachelor and Master’s in Philosophy in Physics from the Australian National University in 2019 and 2021 and also interned at Nanyang Technological University in 2018. She is a recipient of the Fulbright Future Fellowship, the Quad Fellowship, and is an Emerson Consequential Scholar. Her current research interests involve topological physics and quantum optics.



Shanhui Fan is the Joseph and Hon Mai Goodman Professor in the School of Engineering, a Professor of Electrical Engineering, a Professor of Applied Physics (by courtesy), and a Senior Fellow of the Precourt Institute for Energy, at the Stanford University. He received his PhD in 1997 in Theoretical Condensed Matter Physics from the Massachusetts Institute of Technology (MIT). His research interests are in fundamental studies of nanophotonic structures, especially photonic crystals, plasmonic structures, and meta-materials, and applications of these structures in energy and information technology applications. He has published approximately 700 refereed journal articles, has given over 400 plenary/keynote/invited talks, and holds over 70 US patents. He is a co-founder of two companies aiming to commercialize high-speed engineering computations and radiative cooling technology respectively. He received a National Science Foundation Career Award (2002), a David and Lucile Packard Fellowship in Science and Engineering (2003), the US National Academy of Sciences W.O. Baker Award for Initiatives in Research (2007), the Adolph Lomb Medal from the Optical Society of America (2007), a Vannevar Bush Faculty Fellowship from the US Department of Defense (2017), a Simons Investigator in Physics (2021), and the R.W. Wood Prize from Optica (2022). He is a member of the National Academy of Engineering, and a Fellow of the IEEE, the American Physical Society, Optica, and SPIE.